

**Study of field-limiting defects in
superconducting RF cavities for
electron-accelerators**

Dissertation

zur Erlangung des Doktorgrades
des Fachbereichs Physik
der Universität Hamburg

vorgelegt von

SEBASTIAN ADERHOLD

aus Köln

Hamburg
2015

Gutachter der Dissertation:	Prof. Dr. Eckhard Elsen Prof. Dr. Erika Garutti
Gutachter der Disputation:	Prof. Dr. Eckhard Elsen Dr. Bernhard Schmidt
Datum der Disputation:	16.12.2014
Vorsitzender des Prüfungsausschusses:	Dr. Georg Steinbrück
Vorsitzende des Promotionsausschusses:	Prof. Dr. Daniela Pfannkuche
Leiter des Fachbereichs Physik:	Prof. Dr. Peter Hauschildt
Dekan der MIN Fakultät:	Prof. Dr. Heinrich Graener

Abstract

Superconducting radio-frequency resonators made from niobium are an integral part of many accelerator projects. Their main advantage are the low ohmic losses resulting in the possibility for a long pulse structure and high duty cycles up to continuous wave (cw) operation. The European X-Ray Free-Electron Laser (XFEL) and the International Linear Collider (ILC) are based on this technology. In some cases the resonators reach accelerating electric fields close to the theoretical limit of bulk niobium. Yet most resonators are limited at lower fields and mass production for large scale accelerator projects suffers from the spread in the achievable gradient per resonator. The main limitations are field emission and the breakdown of superconductivity (quench). While field emission is mostly attributed to the overall surface cleanliness of the resonator, quench is usually associated with local defects.

Optical inspection of the inner surface of the resonators with unprecedented resolution, accuracy and a special illumination has been established at DESY and used to study such local surface defects. More than 30 resonators have been inspected. Distinctive features from these inspections have been catalogued and assessed for their potential risk for the performance of the resonator. Several confirmed quenching defects could be extracted for further analysis and could be traced back to likely origins in the production process.

A new, automated set-up for optical inspection of large series of resonators, named OBACHT, has been developed and successfully commissioned. Its design includes the minimal need for operator interference, reproducibility, robustness and versatility, in order to fit the requirements for application both in a laboratory and in a production environment.

To facilitate the comparison of the results obtained during the global R&D effort on resonators for the ILC, the ILC global yield database has been established. The yield and selection rules for the resonators have been defined and the ILC yield database has served as a tool to monitor the progress of the ILC R&D program.

Kurzfassung

Supraleitende Hochfrequenz-Resonatoren aus Niob sind Bestandteil vieler Teilchenbeschleuniger. Ihr größter Vorteil ist die geringe Verlustleistung und die daraus resultierende Möglichkeit von langen Pulsen und einer hohen relativen Einschaltdauer (duty cycle) bis hin zu kontinuierlichem Betrieb. Der European X-Ray Free-Electron Laser (XFEL) und der International Linear Collider (ILC) basieren auf dieser Technologie. In manchen Fällen erreichen die Resonatoren elektrische Beschleunigungsspannungen nahe dem theoretischen Wert für Niob. Trotzdem sind die meisten Resonatoren bei niedrigeren Feldern limitiert und eine Massenproduktion für große Beschleunigerprojekte leidet unter der starken Streuung des erreichbaren Gradienten je Resonator. Die wichtigsten Begrenzungen sind Feldemission und der Zusammenbruch der Supraleitung (Quench). Während Feldemission üblicherweise von der allgemeinen Sauberkeit des Resonators abhängt, wird der Quench eher mit lokalen Defekten in Verbindung gebracht. Zur Untersuchung von solchen lokalen Defekten wurde die optische Inspektion der inneren Oberfläche der Resonatoren mit sehr hoher Auflösung, Genauigkeit und spezieller Beleuchtung bei DESY eingeführt und auf mehr als 30 Resonatoren angewendet. Auffallende Objekte und Eigenschaften der Oberfläche aus diesen Inspektionen wurden katalogisiert und hinsichtlich ihres möglichen Einflusses auf die supraleitenden Hochfrequenzeigenschaften des Resonators bewertet. Mehrere Defekte, die als Quench-Ort bestätigt waren, wurden aus den Resonatoren herausgeschnitten und analysiert. Sie konnten wahrscheinlichen Ursachen im Produktionsprozess zugeordnet werden.

Zur optischen Inspektion einer größeren Anzahl von Resonatoren wurde das neue, automatisierte Instrument OBACHT entwickelt. OBACHT zeichnet sich aus durch den minimalen erforderlichen Eingriff eines Operators, Wiederholgenauigkeit, Robustheit und Flexibilität. Dadurch kann es sowohl im Labor als auch in einer Produktionsumgebung eingesetzt werden.

Zur Vereinfachung des Vergleiches der Ergebnisse aus der weltweiten Forschung an Resonatoren für den ILC wurde die *ILC global yield database* etabliert. Die einheitliche Definition der Produktionsausbeute und der Auswahlkriterien für die Resonatoren haben die Datenbank zu einem nützlichen Werkzeug zur Verfolgung der Fortschritte des ILC R&D Programms gemacht.

Contents

1	Introduction	1
2	Towards the International Linear Collider ILC	5
2.1	The need for a linear lepton collider	5
2.2	TESLA	8
2.2.1	Tesla Test Facility TTF and FLASH	8
2.3	The European XFEL	9
2.4	The International Linear Collider ILC	10
2.4.1	Decision for superconducting acceleration techniques	10
2.4.2	Layout and components	10
3	Fundamentals of RF acceleration and superconductivity	13
3.1	RF acceleration	13
3.2	Superconductivity	17
3.2.1	Meissner-Ochsenfeld effect	17
3.2.2	London equations and London penetration depth	19
3.3	Limitations for superconducting cavities	19
3.3.1	Field emission	19
3.3.2	Thermal breakdown	23
3.3.3	Multipacting	25
3.3.4	Q-switch	25
3.3.5	Q-disease	26
4	Fabrication and Preparation of SRF cavities	29
4.1	Fabrication	29
4.2	Surface Preparation	31
4.2.1	Buffered chemical polishing	31
4.2.2	Electropolishing	33
4.2.3	High pressure rinsing	34
4.2.4	Heat treatment	35
5	Cavity performance test at DESY	37
5.1	Test in vertical cryostat	37

5.2	Mode measurement	39
5.3	Temperature mapping	40
5.4	Second sound	42
6	The optical inspection system	45
6.1	Motivation for an optical inspection system	45
6.2	Optical inspection tool	48
6.2.1	Camera properties and image size	50
6.2.2	Depth of field	51
6.2.3	Illumination system	52
6.3	Coordinate system	54
6.4	OBACHT	54
7	Results of cavity inspections	59
7.1	Examples of inspected surfaces	59
7.1.1	Standard welds	59
7.1.2	Non-straight welding	62
7.1.3	Weld-overlap	62
7.1.4	Welds in LG material	64
7.1.5	Grinding of welding seams	66
7.1.6	Spots and stains on the surface	67
7.1.7	"Dirty" cavity surface	69
7.1.8	Scratches	70
7.1.9	Pits and "Cat-Eyes"	71
7.1.10	Pronounced grain-boundaries in fine grain cavities	73
7.1.11	Risk assessment for optical features	74
7.2	Linking images and cavity performance	75
7.3	Analysis of individual cavities	75
7.3.1	AC126	75
7.3.2	Z161	79
7.3.3	Z130	84
7.3.4	AC151	84
7.3.5	Z142	90
7.3.6	AC71	90
7.4	Defect size and quench field	93
7.5	Large Grain Cavities	95
8	The ILC yield database	99
8.1	Selection criteria	99
8.1.1	First pass	100
8.1.2	Second pass	100
8.1.3	Time evolution of the yield	101
9	Summary	105

A Data for yield plots	109
B Spots in Z161	111
List of Figures	I
List of Tables	V
References	XIV
Acknowledgement	XVI

CHAPTER 1

Introduction

The discovery of a Higgs-boson at the Large Hadron Collider (LHC) at CERN confirmed the last predicted but missing particle of the standard model of particle physics. As a part of the Higgs mechanism it is responsible for the explanation why elementary particles have mass. Its mass is near 125 GeV and its properties are so far found to be compatible with the expectations for the standard model. Still, it is possible that the found Higgs particle is only one of several scalar bosons with the others to be discovered.

Hadron machines reach the highest collision energies, which is why the LHC is sometimes called a "discovery" machine. It will have to be followed by a high precision machine to measure the properties of the Higgs-boson and possible future discoveries in detail. Lepton colliders are best suited as such high precision machines.

Two different layouts are possible for such a collider: circular or linear. In principle, less installed accelerating voltage is needed to reach a certain center of mass energy for the collision in a circular collider than in a linear one. The particles pass the accelerating structures on each turn and gain more energy, while in the linear case each point of the accelerator is only passed once. But with increasing particle energy E the energy loss due to synchrotron radiation increases dramatically ($\sim E^4/R$) and can only be partially counteracted by increasing the radius of the accelerator R .

The concept of a circular lepton collider to follow the LHC at CERN, Future Circular Collider-ee (FCC-ee), explores the possibility of a rather big circumference of 80 km to 100 km [1]. The circumference is motivated by the aim of a hadron collider (FCC-hh) with a center of mass energy of 100 TeV. With the parameters chosen for the desired luminosity of FCC-ee, it still would have to deal with a synchrotron radiation load of 50 MW per beam. The energy loss by synchrotron radiation introduces different problems. The particle energy needs to be restored continuously by re-acceleration and the beam pipe needs to be constructed in such a way, that it is able to withstand such high loads of power, which also has to be transported away by the cooling-system. The problem of synchrotron radiation can be mitigated completely by choosing the accelerator to be linear.

The most mature proposal for a linear collider at present is the International Linear Collider ILC [2], consisting of two 11 km long linacs for electrons and positrons. Its center of

mass energy is designed to cover the range of 200 GeV to 500 GeV, with the possibility for an upgrade to 1 TeV.

Based on the choice of material for the accelerating resonators, accelerators can be grouped in two categories. The resonators are either made from normalconducting material (mostly copper) and operated at room-temperature or superconducting material (e.g. niobium) that demands operation at cryogenic temperatures. In general normalconducting resonators allow higher accelerating gradients than the superconducting ones. But due to the ohmic losses in the resonator walls, the dissipated power in the normalconducting resonators is larger by orders of magnitude. This makes normalconducting resonators prohibitive for long pulses or even cw-operation. The low losses at cryogenic temperatures for superconducting resonators are corresponding to larger losses at room temperature due to the efficiency of the cryo plant. Still the overall power consumption is lower than for normalconducting structures. The lower power consumption and thereby operating cost together with other advantages like a longer pulse structure or even cw-operation, as described in Section 2.4.1, makes the superconducting technology highly attractive for a future linear lepton collider and has thus been chosen for the International Linear Collider ILC.

The accelerating resonators, or *cavities*, for the ILC are based on the 1.3 GHz nine-cell TESLA-type superconducting cavities [3]. For a linear collider the length is inversely proportional to the accelerating gradient for a given desired particle energy. Hence the accelerating gradient has to be as high as possible in order to contain the overall length. Individual 9-cell cavities have demonstrated excellent performance up to about 45 MV/m [4], and thereby close to the fundamental limit that is set by the current choice of material and geometry. However, mass production for large-scale accelerator projects with hundreds or thousands of resonators would suffer from the large spread in achievable maximum gradient per cavity. A more conservative choice for the ILC was therefore a design average accelerating gradient of 35 MV/m with a planned average operational gradient of 31.5 MV/m.

This work introduces optical inspection of the inner surface of the cavities as diagnostic method to investigate objects (defects) on the surface that affect the performance of the cavity. The cavities that have been inspected in the scope of this thesis are from the R&D effort at the Free Electron Laser Hamburg FLASH, that is successfully operated since many years at DESY, and the preparatory phase of the European X-Ray Free-Electron Laser XFEL, that is currently under construction at DESY. The type of cavities is the same for both accelerators and will also be the same for ILC. FLASH, the European XFEL and the ILC are introduced in more detail in Chapter 2.

Usually the limiting spot of a cavity is determined during the RF-test of the reachable gradient in a vertical cryostat by methods of thermal mapping of the outer cavity surface (Tmap) or second sound. Both methods detect the location of the breakdown of superconductivity by the large amount of thermal energy that is deposited locally. The so called vertical test and the associated diagnostic methods are described in detail in Chapter 5. Optical inspection tends to result in not only one distinct spot but a number of eye-catching features, as listed in the beginning of Chapter 7. By comparison with

the results of Tmap and second sound it was possible to determine which objects found in optical inspection limit the cavity performance and which do not. Several of such limiting defects that have been found in optical inspection and were confirmed as limiting location have been extracted from the cavity and analysed in detail to understand their origin and the limiting mechanism.

In contrast to the vertical performance test of the cavity that can only be done at the very end of the fabrication and surface preparation process, optical inspection is possible at all stages of the preparation process. It was thereby possible to trace defects to their origins and also track their evolution during further surface treatment steps. This allows to implement optical inspection as a tool for quality control during cavity fabrication and surface processing. A new optical inspection set-up named OBACHT (Chapter 6.4) has been developed and is in regular operation at DESY now.

CHAPTER 2

Towards the International Linear Collider ILC

2.1 The need for a linear lepton collider

The standard model of particle physics comprises the elementary particles that form the building blocks in the construction kit of nature and three fundamental forces that describe their interaction. The particles in the standard model are depicted in Fig. 2.1. They are divided into fermions with spin $s = \frac{1}{2}$ and bosons with integer spin, as well as their respective antiparticles. Within the fermions there are six different leptons and six types of quarks. The bosons can be identified with the exchange particles of the three fundamental forces in the standard model, namely the photon for the electric force, the gluon for the strong force and the W- and Z-bosons for the weak force.

Since its development in the second half of the 20th century the standard model of particle physics has been very successful in explaining the observations and making predictions of particle discoveries, for example with the confirmation of one of its elements, the top quark, at the Tevatron in 1995 [6, 7]. The last remaining particle predicted in the standard model but not confirmed was the Higgs boson. It is part of the Higgs mechanism that has been introduced to explain how the elementary particles, as the W- and Z-bosons, gain their mass [8, 9]. The latest effort in searching for the Higgs boson and physics beyond the standard model has been carried out at the Large Hadron Collider LHC [10] at CERN. The Higgs-searches at the two large multi-purpose experiments at LHC, ATLAS [11] and CMS [12], have resulted in the observation of a new boson with a mass near 125 GeV [13, 14]. The characteristics of the observed particle are so far compatible with the expectations for the standard model Higgs boson.

In addition to the Higgs boson, there are other aspects that give rise to the need for an extension of the standard model. For example only three out of the four fundamental forces, namely electro-magnetic, weak and strong force are included in the standard model, while gravitation can not be treated. Also a unification of the coupling of the three forces within the standard model is not possible. While the unification of electro-magnetic and weak

2 Towards the International Linear Collider ILC

	1. Generation	2. Generation	3. Generation	Gauge Bosons
Quarks	u up $s = 1/2$ $Q = +2/3e$ $m = 1.7-3.1 \text{ MeV}$	c charm $s = 1/2$ $Q = +2/3e$ $m = 1.29^{+0.05}_{-0.11} \text{ GeV}$	t top $s = 1/2$ $Q = +2/3e$ $m = 172.9 \pm 1.5 \text{ GeV}$	γ photon $s = 1$ $Q = 0$ $m < 10^{-18} \text{ eV}$
	d down $s = 1/2$ $Q = -1/3e$ $m = 4.1-5.7 \text{ MeV}$	s strange $s = 1/2$ $Q = -1/3e$ $m = 100^{+30}_{-20} \text{ MeV}$	b bottom $s = 1/2$ $Q = -1/3e$ $m = 4.19^{+0.18}_{-0.06} \text{ GeV}$	Z^0 $s = 1$ $Q = 0$ $m = 91.2 \text{ GeV}$
Leptons	e^- electron $s = 1/2$ $Q = -1e$ $m = 0.51 \text{ MeV}$	μ^- muon $s = 1/2$ $Q = -1e$ $m = 105.6 \text{ MeV}$	τ^- tau $s = 1/2$ $Q = -1e$ $m = 1777 \text{ MeV}$	W^\pm $s = 1$ $Q = \pm 1e$ $m = 80.4 \text{ GeV}$
	ν_e electron neutrino $s = 1/2$ $Q = 0$ $m < 2 \text{ eV}$	ν_μ muon neutrino $s = 1/2$ $Q = 0$ $m < 2 \text{ eV}$	ν_τ tau neutrino $s = 1/2$ $Q = 0$ $m < 2 \text{ eV}$	g gluon $s = 1$ $Q = 0$ $m = 0$

Figure 2.1: Elementary particles in the standard model of particle physics along with their spin, electric charge and mass. The Higgs boson is not shown. Based on data from [5]

force to an electroweak force is possible, an expansion onto the strong force at high energies needs concepts that are beyond the extent of the current standard model.

From astronomical and cosmological observations like gravitational lensing and the mismatch in the mass of rotating galaxies when comparing the visible matter and mass derived from the analysis of their rotation curves, it is clear that our universe consists of more than just the "visible matter" included in the standard model. Observations of the cosmic microwave background [15] show the fraction of atoms in the universe's mass-energy budget to be less than 5%. The rest is so-called dark matter (about 24%) and dark energy. While there is no evidence for what the dark matter consists of, there are several possible solutions. One could be part of so-called supersymmetry [16, 17], a concept that is discussed as a possible cure for the above-mentioned weaknesses of the standard model. In supersymmetry each particle of the standard model is given a "superpartner". The lightest of those supersymmetric particles (LSP) would be a candidate for the dark matter.

The limits of high energy physics have been pushed jointly by hadron and lepton colliders in the past. Originating in the nature of the accelerated particles, hadron colliders (accelerating protons and anti-protons) are more suited as "discovery machines" while lepton colliders (accelerating electrons and positrons) offer the more precise measurements.

Protons (and anti-protons) are not elementary particles but carry a substructure of quarks and gluons. In a proton-proton collision one can not pre-define which part of one proton (parton) will collide with which part of the other proton. Also the fraction of the momentum that takes part in the collision can not be chosen. Also the strong interaction of the partons leads to a high background of QCD reactions with complex events in the detector to analyse. As electrons and positrons are elementary particles without substructure the initial state for the collision can be chosen much better. The momentum of both particles is fixed by the beam energy and can be adjusted as well as their polarisation. Since no strong but electroweak interactions are happening, the background in the detectors is lower than in the proton-proton case. That makes a lepton collider the best choice for precision measurements.

The maximum achievable collision energy in a circular collider is limited by the maximum force of the dipole magnets that bend the particles trajectory to keep them on the circular path and by synchrotron radiation. The energy ΔE lost per revolution via synchrotron radiation by a particle with energy E and mass m is described by

$$\Delta E \sim \frac{E^4}{m^4 R} \quad (2.1)$$

where R is the radius of the accelerator. Due to the m^4 -term in the denominator and the mass ratio of $\frac{m_p}{m_e} \approx 1800$ synchrotron radiation is highly suppressed for protons compared to electrons, permitting much higher energies for protons at a given accelerator radius. Since the energy loss by synchrotron radiation increases with the fourth power of the particles energy E the amount of energy that has to be replaced by the accelerating structures reaches impractical values quickly. As the radius of the accelerator enters only linearly

the dimensions of a ring would reach gigantic scales when trying to compensate the higher energies with bigger radii. That is why the next lepton collider has to be built in a linear shape.

In 2003 several concepts for a linear lepton collider with similar physics goals but different accelerating techniques were existing [18]. The Japan Linear Collider JLC [19] proposed by KEK in Japan included two different versions: JLC-C, with normalconducting linacs operating in the C-band at 5.4 GHz and JLC-X, operating in the X-band at 11.4 GHz. Very similar to JLC-X is the Next Linear Collider NLC [20] also operating at 11.4 GHz. In fact JLC-X and NLC were unified into one design. The most important design (with respect to this work) on the path towards the ILC, the TeV-Energy Superconducting Linear Accelerator TESLA is presented with a little more detail in the following section.

2.2 TESLA

The TeV-Energy Superconducting Linear Accelerator (TESLA) was designed as a linear collider of electrons and positrons at a center of mass energy of 500 GeV with the option for an extension to 800 GeV [21]. With a total site length of 33 km the two linacs facing each other were to collide the particles in a detector at the central interaction point.

It was intended to include a X-ray free-electron laser into TESLA. Electrons could be extracted at intermediate points of the electron linac and guided to undulator magnets for the creation of coherent X-ray pulses down to a wavelength of 0.85 Å with a pulse length on the order of ~ 100 fs.

Acceleration of the electrons and positrons is achieved by the use of superconducting nine-cell cavities operating at a frequency of 1.3 GHz. The frequency choice is a trade-off between several parameters. Making the frequency too low results in larger cavity dimensions. That is unfavourable because of the high number of cavities needed in a linear collider. Setting the frequency too high yields higher losses in the cavity walls and more problems with wake-fields. The optimum would be around 1.5 GHz, the actual value of 1.3 GHz has been chosen because of the good availability of high-power klystrons.

The design operating accelerating gradient for TESLA is set to 23.4 MV/m. In the beginning of the TESLA effort such accelerating gradients were not regularly achieved in superconducting cavities. Therefore the Tesla Test Facility TTF was implemented at DESY.

2.2.1 Tesla Test Facility TTF and FLASH

The Tesla Test Facility TTF was established at DESY in order to demonstrate that the TESLA technology is able to provide cavities of the desired accelerating gradients and to operate them in an actual linac to accelerate electrons [22]. The initial design included four cryo-modules of eight cavities each. Depending on the achieved accelerating gradient the expected final energy of the electrons was 300 MeV to 500 MeV. After the first very successful steps of cavity preparation and operation in the linac [23] additional



Figure 2.2: Birds-eye view of the future European XFEL, electrons will be accelerated from DESY-Bahrenfeld (right) in the direction of Osdorfer Born (middle) where undulators create the X-ray pulses that are then guided to the experiments in Schenefeld (left) (© European XFEL)

components for a free-electron laser were included at the end of the accelerator [24]. At this free-electron laser the first Self-Amplified Spontaneous Emission (SASE) emission at 109 nm was observed [25]. Stepwise the linac and the FEL components were expanded to provide electron energies up to 1.25 GeV and FEL wavelength in the water-window at 4.1 nm [26]. In the mean-time the accelerator that started as a test facility was turned into a FEL user facility and named Free-Electron Laser Hamburg (FLASH).

The operation of TTF and FLASH as a user facility has given invaluable experience for the conceptual design of the European XFEL. In addition it has been an unrivalled possibility for the test of fabrication, preparation and operation under true accelerator conditions of TESLA-type cavities. All cavities that have been studied within the scope of this work are part of this prototype programme of the European XFEL and FLASH.

2.3 The European XFEL

The European X-ray Free-Electron Laser (XFEL) [27] is currently under construction at DESY. The XFEL was initially included as a part in the proposal for TESLA. As TESLA was not approved, the European XFEL was proposed and approved as a stand-alone facility. The objective is to provide coherent X-ray pulses of high intensity and short duration of wavelength down to 0.1 nm for structural experiments. The short wavelength in the order of atomic scales allows the exploration of molecules and materials in very high detail. The short pulse length of ~ 100 fs gives access to the temporal structure of biological and chemical processes, such as the formation of molecules.

The X-ray pulses are created by guiding a bunched electron beam through undulator magnets, where they are stimulated to emit in the SASE-process by the alternating magnetic field.

For the wavelength of 0.1 nm the electrons have to be accelerated to an energy of

17.5 GeV. The injector complex for the accelerator is situated on the DESY site and the tunnel then continues in the direction of Schenefeld with a total length of 3.4 km (see Fig. 2.2). The 1.7 km long linear accelerator consists of 100 modules containing 8 superconducting cavities of the TESLA-type [3] each, running at an operating gradient of 23.6 MV/m. The cavity technology is the same as is foreseen for the ILC. Since 800 is the largest number of TESLA-type cavities being built up to now, the fabrication for the European XFEL will be a very valuable experience with regard to the ILC.

2.4 The International Linear Collider ILC

2.4.1 Decision for superconducting acceleration techniques

As recommended by the International Technology Recommendation Panel (ITRP) [28] the ILC would be built based on "cold" superconducting acceleration technique. A superconducting accelerator holds several advantages over a normal conducting one. The advantage mainly originates from the fact that the losses caused by the RF current in the cavity walls are smaller by orders of magnitude (for more details see Section 3). The lower losses result in the need for less RF power what on the one hand side brings lower investment costs for e.g. klystrons and even more important much lower operational cost for power consumption. While at high gradients normal conducting cavities can only be operated with short pulses superconducting cavities allow longer pulses¹ or even CW operation. SCRF cavities can be built with a significantly larger aperture for the beam because of typically lower operating frequencies compared to normalconducting equivalents. This is due to the effect that the BCS-component of the surface resistance and thereby the losses in a superconducting cavity decrease with lower frequencies, in contrast to a normalconducting one. The larger aperture of the cavity results in a lower impedance. Thereby higher beam currents are possible with lower detrimental effects for the beam quality.

2.4.2 Layout and components

The proposed design of the ILC consists of two linear accelerators, one for electrons and one for positrons, facing each other [29]. The overall layout is shown in Fig. 2.3. Both linacs have a length of about 11 km. The length is determined by the desired center of mass energy of 500 GeV and the chosen accelerating gradient of 31.5 MV/m. The electrons are produced by illuminating a photocathode with a laser, followed by a section for bunching and pre-acceleration. By using a polarised laser, a polarisation of the electron beam of at least 80 % is achieved. In the baseline design the particles are accelerated in so-called bunch trains at a repetition rate of 5 Hz. i.e. the bunch trains of about 1 ms

¹The pulse structure of the ILC is discussed in Section 2.4.2

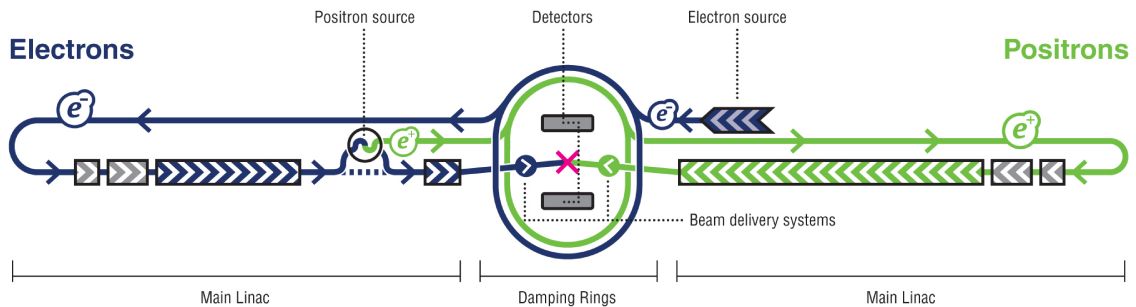


Figure 2.3: Schematic drawing of the ILC design layout [30]

length have a gap of 199 ns in-between. Each bunch train consists of 1312 bunches. The bunch spacing is 554 ns and bunch length 300 μm . The production of the positron bunches is a bit more complicated than the electron bunches. The electron beam from the main linac passes a helical undulator after having reached an energy of 150 GeV and emits photons of several MeV. Those photons are directed on a metal target in order to produce electron-positron pairs in electro-magnetic showers. The positrons are separated from the shower, pre-accelerated to 5 GeV and transported to the damping ring. Damping rings are needed both for the positron as well as for the electron beam. Here the emittance of both beams is reduced to the design values in order to achieve the desired luminosity. Damping is achieved by the emission of synchrotron radiation in the bending magnets and dedicated damping wigglers. The emission reduces the transverse momentum as well while only the longitudinal component is restored via accelerating cavities, resulting in an emittance reduction. The damping rings have a circumference of 3.2 km and are located in the center of the facility surrounding the interaction region. After sufficient damping the beams are transferred to their respective ends of the main linacs. Each linac consists of about 8000 superconducting 1.3 GHz cavities. More details about the cavities can be found in Section 3.1. After acceleration to the final energy the beams are guided to the interaction region by the beam delivery system (BDS). The BDS focusses the beams to the final collision conditions and is well instrumented in order to monitor beam parameters like polarisation and beam energy before and after the collision. In contrast to a circular collider where multiple interaction points can be maintained around the circumference, only one interaction region is present in the layout of the ILC, sitting in the middle of the damping rings. Two detectors are going to be operated there, the Silicon Detector (SiD) [31] and the International Large Detector (ILD) [32]. The detectors will be operated in a so-called "push-pull" mode. Only one detector is at the interaction point taking data at a time. The other detector is resting beside. After a period of data taking the first detector is "pulled" out of the interaction point and the other is "pushed" into it. This procedure is then repeated after the next data taking period.

The SRF cavities and the associated subsystems, together with the costs for buildings and the tunnel, are by far the biggest cost driver in the ILC estimated building budget,

Table 2.1: Selected nominal parameters for the ILC [2].

Parameter	Nominal value	Unit
Center-of-mass energy	500	GeV
Peak luminosity	1.8×10^{34}	$\text{cm}^{-2}\text{s}^{-1}$
Particles per bunch	2×10^{10}	
Bunch separation	554	ns
RMS bunch length	300	μm

together with the civil engineering part, that is mainly dominated by the cost for building the underground tunnel structure. That motivated the aim in R&D to not only push the individual cavities for maximum performance but also consider how to establish a cavity production that is able to yield the large number of cavities in a cost effective way. The standard recipe for cavity production and treatment has proven to create cavities with accelerating gradients that satisfy the desired values for ILC operation. Nevertheless there are individual, localized defects that hinder cavities from reaching these values. The R&D effort to find, investigate and finally eliminate those flaws has been carried out globally with all major laboratories active in the field of SRF cavities.

CHAPTER 3

Fundamentals of RF acceleration and superconductivity

3.1 RF acceleration

Acceleration of charged particles can be achieved by exposing them to the fields inside radio-frequency (RF) resonators or *cavities*.

The two most important figures of merit of a superconducting RF cavity are the gradient of the accelerating field E_{acc} and its unloaded quality factor Q_0 . E_{acc} determines how much energy a particle can gain per given length. Q_0 describes, simply speaking, how efficient the acceleration can happen and is related to the power dissipation in the cavity.

The distribution of electro-magnetic field-lines for the TM_{010} -mode inside a 9-cell cavity is shown in Fig. 3.1. This mode is most suited for particle acceleration, as the electric field is aligned to the beam-axis of the cavity. The magnetic field lines surround the electric ones in perpendicular circles. This results in the magnetic field to be maximal at the equator regions. This will become important in later considerations.

As a 9-cell cavity consists of nine coupled oscillators, the fundamental mode splits up

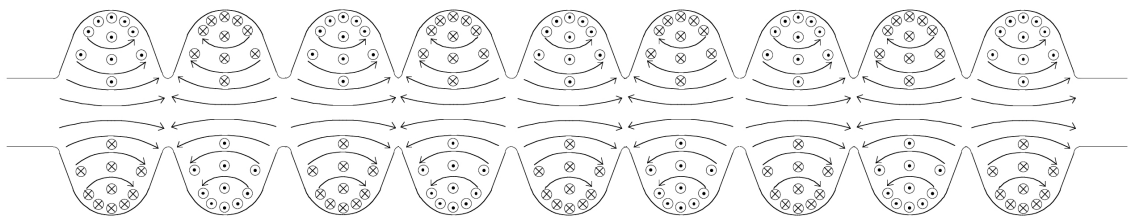


Figure 3.1: Distribution of electro-magnetic field lines inside a 9-cell cavity. The electric field is aligned to the beam axis, the magnetic field surrounds it perpendicular. In the π -mode shown here, electric field in neighbouring cells is of opposite direction. [33]

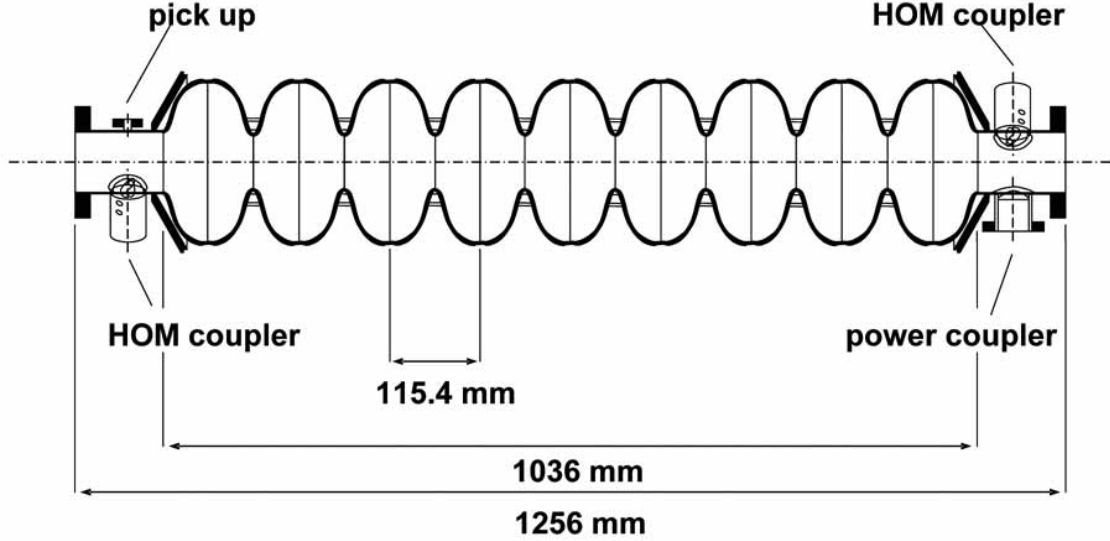


Figure 3.2: Schematic cross-section view of a TESLA-shape 9-cell cavity. The main power coupler is on the right side. In addition the higher order mode (HOM) couplers on each side and the pickup coupler are marked. [27]

into a spectrum of nine modes. According to the phase advance from cell to cell they are named $\frac{\pi}{9}$ -mode, $\frac{2\pi}{9}$ -mode, ..., π -mode. The amplitude of the electric field for each of this modes is shown in Fig. 3.3. The most suitable mode for particle acceleration is the π -mode, where the electric field is of opposite direction in neighbouring cells. When arriving in phase, a particle experiences an accelerating field in the first cell. During the time the particle travels to the next cell, the field has changed its direction and the particle is accelerated again. This continues from cell to cell. For a particle to gain the maximum possible energy, the time it travels through one cell needs to be matched to one-half of the rf-period.

For a particle close to the speed of light c , as it can be safely assumed when dealing with electrons, the accelerating voltage V_{acc} is obtained by integrating along the path d through the cavity:

$$V_{acc} = \left| \int_0^d E_z(z) e^{i\omega z/c} dz \right| \quad (3.1)$$

where ω is the eigenfrequency of the accelerating mode.

To obtain the average accelerating electric field E_{acc} , also often called *accelerating gradient*, of the cavity, the accelerating voltage V_{acc} is simply divided by the active accelerating length of the cavity d :

$$E_{acc} = \frac{V_{acc}}{d} \quad (3.2)$$

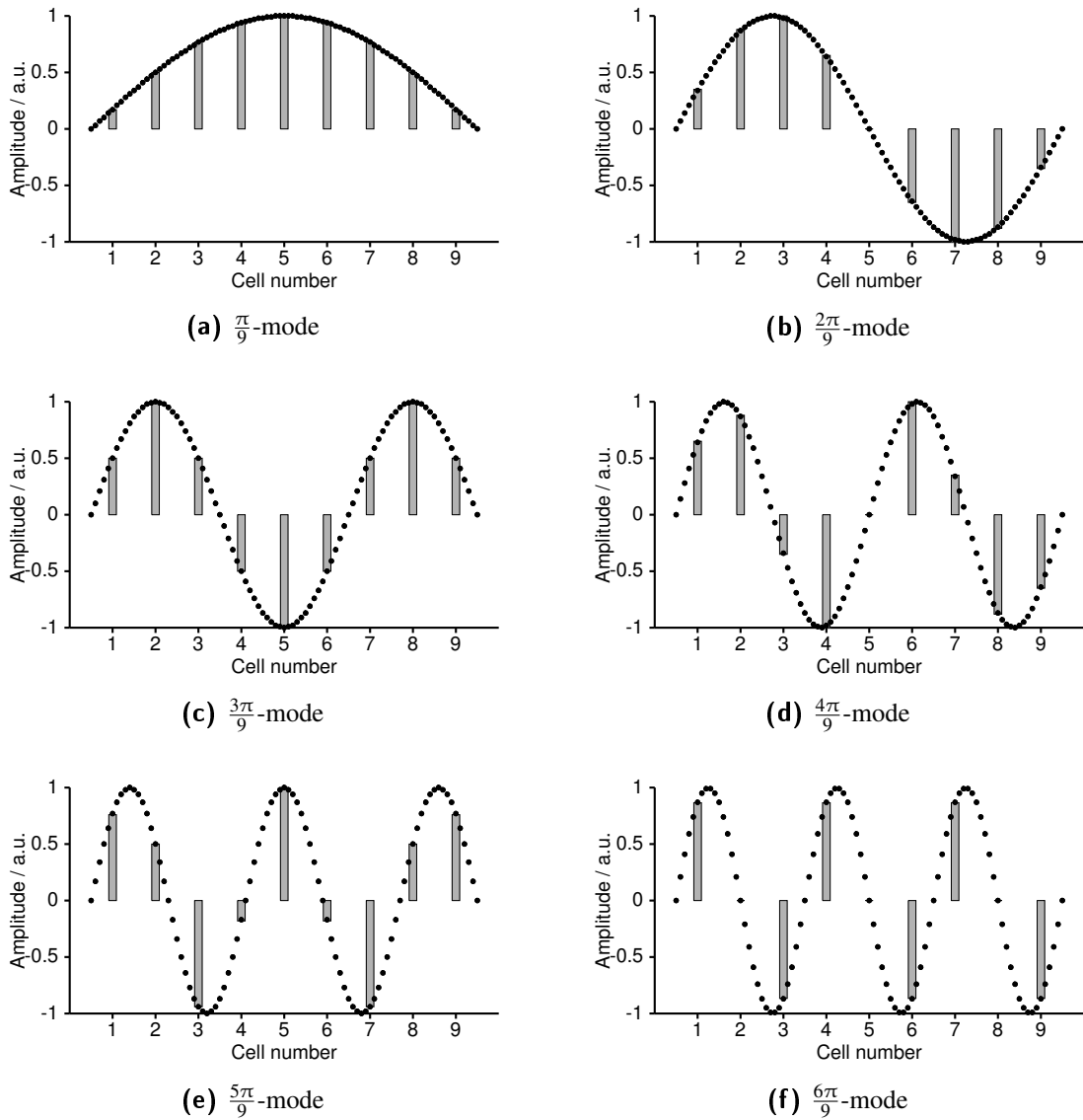


Figure 3.3: Relative distribution of the electric field in the nine cells for all nine modes, normalised to highest occurring amplitude. The bars show the field in the center of the cells, the dotted line is the continuous field distribution. Note the symmetry with respect to the center cell.

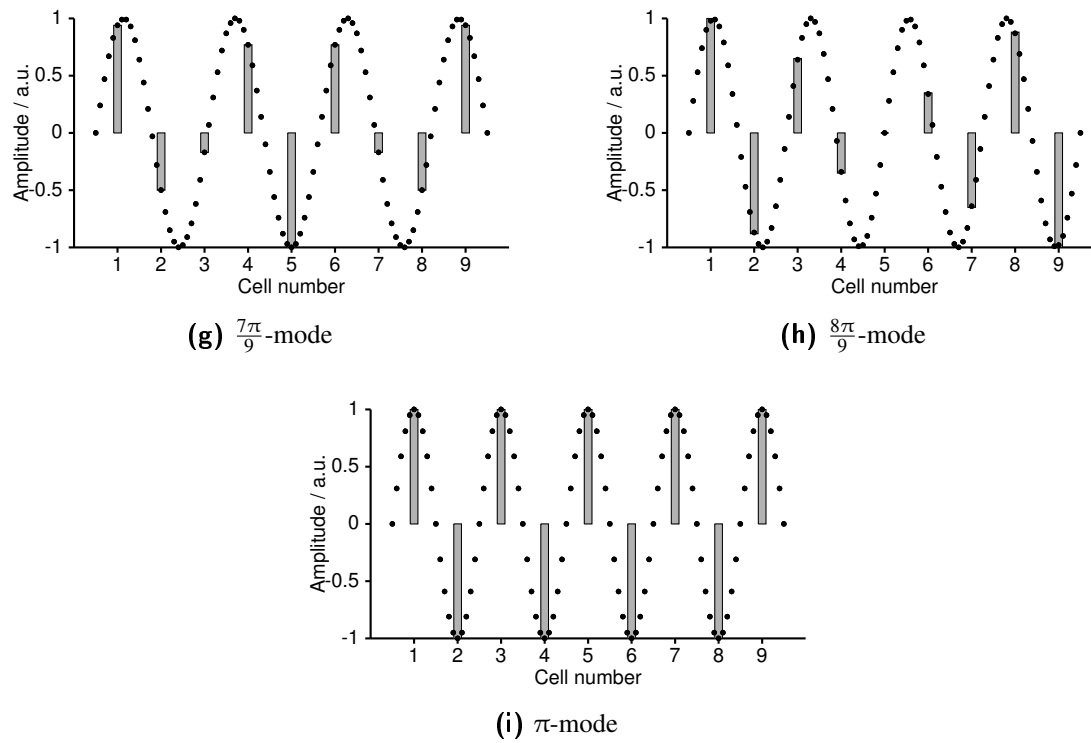


Figure 3.3: Relative distribution of the electric field in the nine cells for all nine modes, normalised to highest occurring amplitude. The bars show the field in the center of the cells, the dotted line is the continuous field distribution. Note the symmetry with respect to the center cell.

The unloaded quality factor Q_0 is closely related to the dissipated power P_{diss} generated by the currents flowing in the upper layers of the inner cavity surface:

$$Q_0 = \frac{\omega_0 U}{P_{diss}} \quad (3.3)$$

where ω_0 is the resonant frequency of the cavity and U is the energy stored in the cavity. The dissipated power P_{diss} is depending on the magnetic field H and the surface resistance R_S :

$$P_{diss} = \frac{1}{2} R_S \int_A H^2 dA \quad (3.4)$$

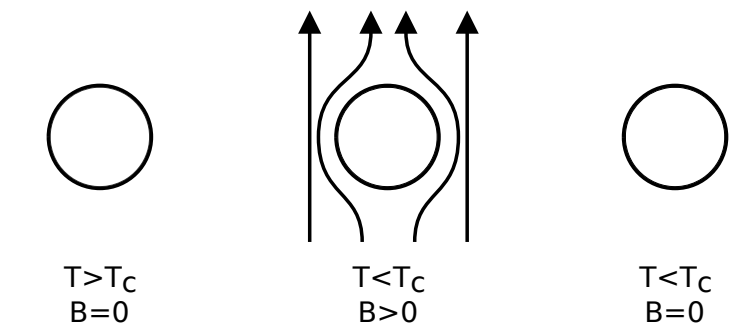
For superconducting cavities the ohmic losses in the cavity walls are very small compared to normal conducting cavities. This results in very high quality factors. In the case of 1.3 GHz TESLA-shape 9-cell cavities typical quality factors lie in the range of $Q_0 = 1 \times 10^{10}$ to few 10^{10} .

3.2 Superconductivity

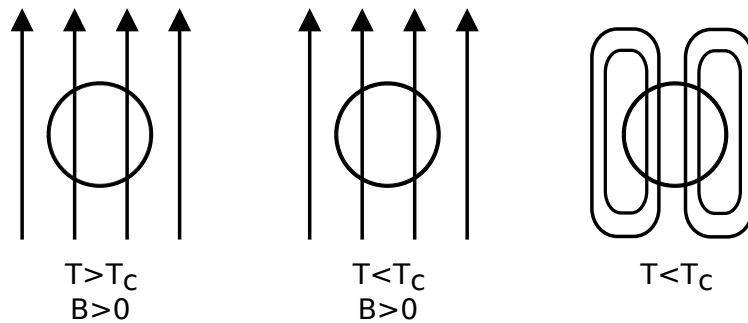
By finding a way to liquefy helium in 1908, Heike Kamerlingh Onnes opened the door to experiments at the temperature of a few Kelvin. Thus, when analysing the properties of mercury at the temperature of liquid helium three years later, he noticed that no ohmic resistance was measurable below a temperature of 4.15 K, a characteristic that is known as superconductivity.

3.2.1 Meissner-Ochsenfeld effect

Besides the complete loss of direct current resistivity below the critical temperature the expulsion of magnetic flux from the inner part of a superconductor is the most impressive property of superconducting materials. The effect was discovered by Walther Meissner and Robert Ochsenfeld in 1933 [34] and is named after them. The Meissner-Ochsenfeld effect is also what distinguishes a superconductor from a theoretical perfect conductor. As illustrated in Fig. 3.4 and Fig. 3.5 the perfect conductor as well as the superconductor shield their inner part from a magnetic field, that is applied after cooling the conductor below its critical temperature T_c . But if the magnetic field is present before cooling below T_c perfect conductor and superconductor behave differently. In the perfect conductor the magnetic field is still able to penetrate and when lowering the external field to zero, the flux is trapped in the perfect conductor and maintains the magnetic field (Fig. 3.4b). The superconductor however expels the magnetic field from its inner part when transitioning from normal to superconducting state (Fig. 3.5b). Only if the magnetic field reaches the critical magnetic field B_c , the superconductive state breaks down and the magnetic flux can enter. For type II superconductors there exists an intermediate state of $B_{c1} < B < B_{c2}$,



(a) Perfect conductor with magnetic field applied after cooling below T_c



(b) Perfect conductor with magnetic field present before cooling below T_c

Figure 3.4: (a) A perfect conductor shields its inner part from external magnetic field, if applied after cooling below T_c (b) Magnetic flux present before cooling below T_c is trapped in a perfect conductor after cooling below T_c

where flux can enter the inner part but the superconducting state is maintained. After crossing B_{c_2} superconductivity breaks down as well.

3.2.2 London equations and London penetration depth

In 1935 Fritz and Heinz London made a phenomenological approach to explain superconductivity [36], including a quantitative description of the Meissner-Ochsenfeld effect, leading to the two following equations:

$$\frac{\partial \mathbf{j}_s}{\partial t} = \frac{n_s e^2}{m} \mathbf{E} \quad (3.5)$$

$$\nabla \times \mathbf{j}_s = -\frac{n_s e^2}{m} \mathbf{B} \quad (3.6)$$

where j_s is the superconducting current, e and m are the charge and mass of the electron and n_s is the number-density of superconducting charge carriers. By applying Ampere's law ($\nabla \times \mathbf{B} = \mu_0 \mathbf{j}$) to London's second equation Eqn. (3.6) one yields the differential equation

$$\nabla^2 \mathbf{B} = \frac{1}{\lambda_L^2} \mathbf{B} \quad (3.7)$$

with the London penetration depth

$$\lambda_L = \sqrt{\frac{m}{\mu_0 n_s e^2}} \quad (3.8)$$

For the case of a magnetic field outside the superconductor, parallel to its boundary, and x perpendicular to that boundary, the solution to the differential equation reads

$$B(x) = B_0 e^{-\frac{x}{\lambda_L}} \quad (3.9)$$

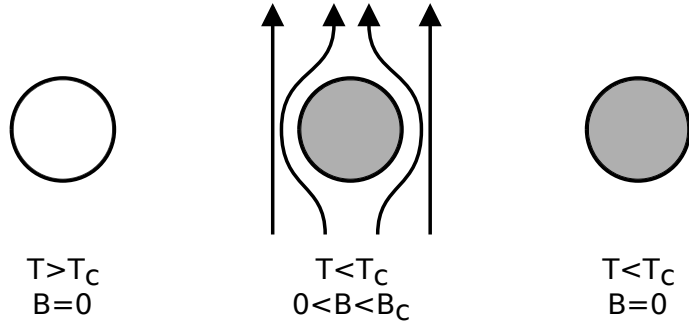
showing, that magnetic field is penetrating into the surface of a superconductor, but decaying exponentially over a short length. Typical values for λ_L in niobium are on the order of some 10 nm.

3.3 Limitations for superconducting cavities

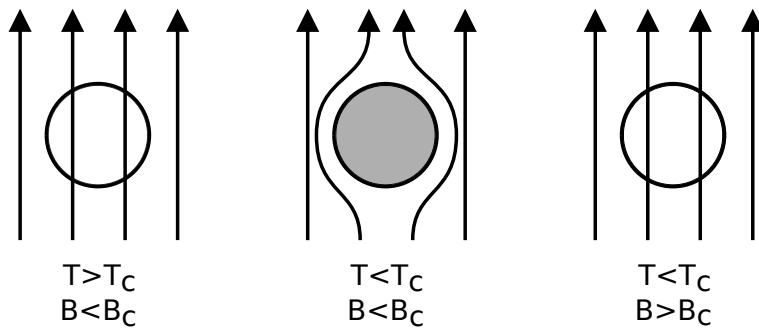
3.3.1 Field emission

Field emission of electrons has been and still is a serious limitation for SRF cavities. Starting from a certain field-strength on electrons free electrons are emitted in the cavity and accelerated by the electric field. The acceleration lowers the stored energy in the cavity

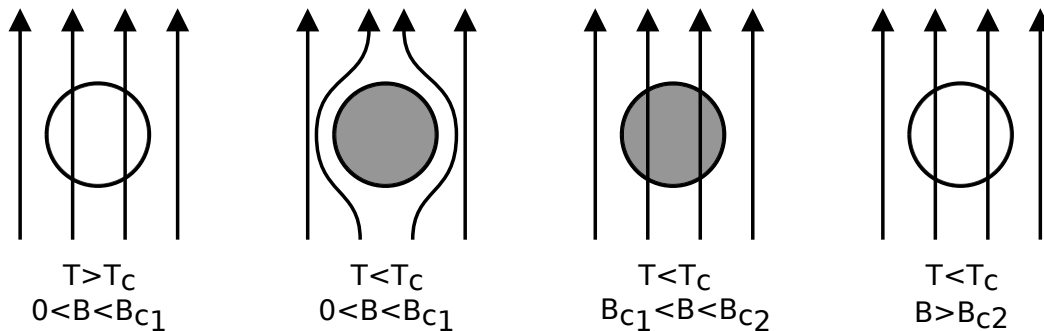
3 Fundamentals of RF acceleration and superconductivity



(a) Type I superconductor with magnetic field applied after cooling below T_c



(b) Type I superconductor with magnetic field present before cooling below T_c . Magnetic flux is expelled below T_c until B reaches B_c



(c) Type II superconductor with magnetic field present before cooling below T_c . Magnetic flux is expelled below T_c until B reaches B_{c1} . For $B_{c1} < B < B_{c2}$ flux enters the superconductor but it remains in superconducting state. Above B_{c2} superconductivity breaks down.

Figure 3.5: A superconductor shields its inner part from external magnetic field as a perfect conductor (a). Expulsion of magnetic flux (Meissner-Ochsenfeld effect) that was present before cooling below T_c in a type I superconductor until breakdown of superconductivity at $B > B_c$ (b). A type II superconductor allows flux penetration for $B_{c1} < B < B_{c2}$ before breaking down (c). Superconducting state is indicated by filled grey circles, normal conducting state by open white circles.

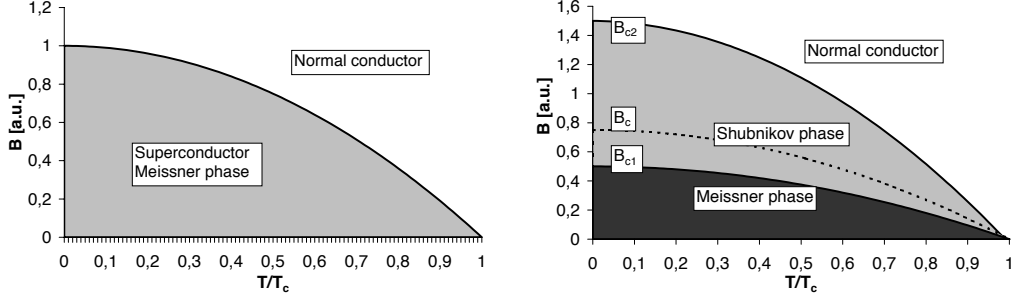


Figure 3.6: B-T-phase-diagrams for type I- (left) and type II- (right) superconductors [35]

and deteriorates the Q . The electrons can hit the surface of the cavity and cause heating. If the heat created by these electrons is too high, a field emission induced quench may occur. In addition for cavities that are operational in an accelerator, the electrons created by field emission create an unwanted dark current that may pose problems at other places in the accelerator.

Electrons in the cavity walls are confined to the metal since their energy is usually lower than the work function ϕ for escaping. In the presence of an electric field on the surface electrons are able to tunnel out of the surface, because the otherwise infinite potential barrier is deformed to a finite triangular shape. Fowler and Nordheim [37] found an expression for the current of electrons tunnelling from an emitter of size A_{emit} . in dependence of the electric field E :

$$I(E) = \frac{A_{emit} \cdot B E^2}{\phi} \exp\left(-\frac{C \phi^{3/2}}{E}\right), \quad (3.10)$$

where $B = e^2/8\pi h$ and $C = 8\pi\sqrt{2m_e}/3he$ are constants, with e the electron charge, h the Planck constant, m_e the electron mass and ϕ the work function of the metal in eV. $v(y)$ and $t(y)$ are functions of the variable $y = \sqrt{\frac{eE}{4\pi\epsilon_0\phi^2}}$, but can be approximated as equal to 1 for a triangular potential barrier.

In experiments with superconducting cavities, where the electrons created by field emission were measured by pick-up probes and the x-ray radiation was analysed, it was found that an additional empirical factor is needed in the equations. With the field-enhancement factor β_{FN} multiplied to the electric field E in the equations the electron current and x-ray radiation predicted by theory match the observation in experiments. The modified FN-equation reads then:

$$I(E) = \frac{A_{emit} \cdot B (\beta_{FN} E)^2}{\phi} \exp\left(-\frac{C \phi^{3/2}}{\beta_{FN} E}\right). \quad (3.11)$$

Explanations for the field enhancement factor β_{FN} can be of different nature. One is of pure geometrical type. Sharp and jagged features on the surface can be present at scratches

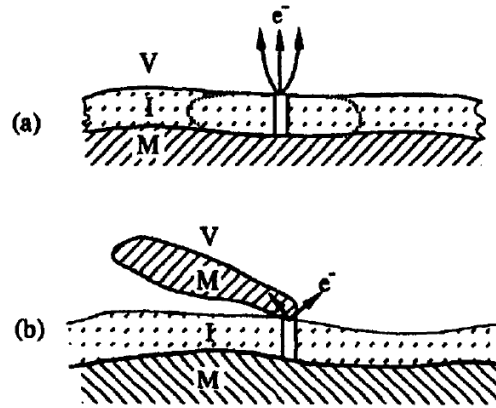


Figure 3.7: Illustration of the metal-insulator-vacuum (MIV) (a) and metal-insulator-metal (MIM) model (b) [40]

or metal particles. The "macroscopic" geometry of particles that have been found at field emitter sites is not able to explain the full enhancement factors of β_{FN} up to several 100 that are observed [38]. The so-called "tip-on-tip-model" gives some improvement over the basic approach [39]. When considering the microstructure of particles, a small tip that is sitting on top of a protrusion can explain higher values for β_{FN} when multiplying the field enhancement factors of both, the protrusion and the tip on top of it, e.g. $\beta_1 = 10$ and $\beta_2 = 10$ resulting in $\beta_{FN} = \beta_1 \beta_2 = 100$.

Another model is the metal-insulator-vacuum (MIV) model [40]. As illustrated in Fig. 3.7 an insulating particle is assumed to be sitting on top of the metal surface. The bulk metal material, the insulating particle as well as the two interfaces, metal-insulator and insulator-vacuum, are described in an electron energy band diagram and form a "pin-hole" that allows the electrons to be emitted into the cavity. In contrast the metal-insulator-metal (MIM) model assumes a metallic, i.e. conducting, particle sitting on top of a thin insulating layer formed by the oxide layer of the bulk metal or an adsorption layer on the metallic particle (Fig. 3.7).

Both of the latter models have in common that the emission site needs to be "switched on" at a certain electric fields. That is in accordance with observations often made during the test of a cavity. A cavity may be field-emission free up to a certain accelerating gradient at which suddenly radiation is measured. In subsequent power-rises the field-emission on-set is at significantly lower accelerating gradients, the field emitter has been "switched on" or "activated", resulting in a lower threshold for emitting.

In the vertical test of a cavity that suffers from field emission two effects can be observed. One is a drop of the quality factor Q , as can be seen in Fig. 3.8. This drop is caused by the additional losses that arise due to the acceleration of the electrons in the accelerating field of the cavity. Simultaneously a rise in radiation can be observed. This radiation is mainly Bremsstrahlung-photons generated by the electrons that hit either the inner cavity wall or the flanges. The radiation sensors are typically placed on top of the cryostat. At

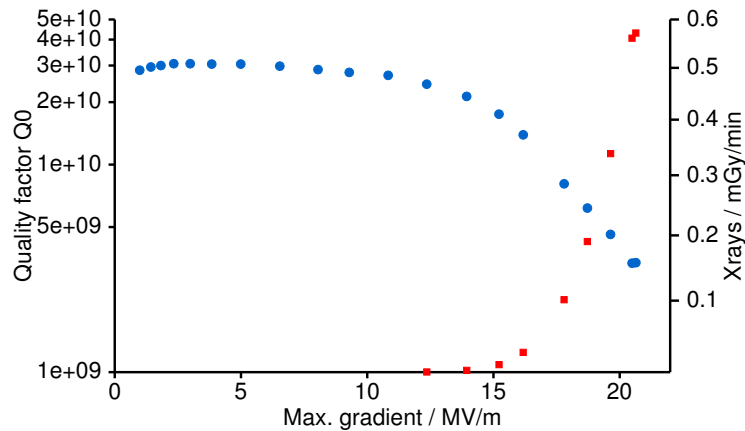


Figure 3.8: Typical $Q(E)$ -curve for a cavity limited by FE. Note the steep decrease of Q (blue circles) once the field emission sets in (red squares)

KEK arrays of PIN-diodes are placed around the irises of the cavity, so that the point of impact of the electrons can be located [41]. It was possible to correlate heating in cells with enhanced radiation at the corresponding PIN-diodes.

Field emission can limit the maximum accelerating gradient of a cavity in two ways. One is that the loss in Q is so high that the power from the amplifier is not sufficient to drive the cavity into a quench. The other happens, when the field emitted electrons hit the inner cavity wall. By impinging on the niobium they heat the spot and if the heating exceeds the cooling capability of the surrounding material, the cavity quenches.

For cavities that are in use in an accelerator there is a third limit to the maximum *usable* gradient. The electrons produced by field emission create a dark current and this dark current must not be arbitrarily high. So an operational limit may have to be set for specific field emission loaded cavities in order to not cross a certain radiation value.

By improving the overall cleanliness of the cavity preparation process and introducing additional special cleaning steps (see Section 4.2) the onset of field emission has been shifted to higher gradients or can be avoided completely in most cavities nowadays.

3.3.2 Thermal breakdown

The phenomenon called thermal breakdown or *quench* describes the breakdown of the superconducting state of a cavity. As shown in Figure 3.6 the superconducting phase is limited by either crossing the critical magnetic field at a given temperature or the critical temperature at a given magnetic field. A simple model for the thermal breakdown is the existence of a small (sub-millimeter) ‘defect’ with a higher surface resistance R_s than the surrounding material. If the surrounding material is not able to transport the excess heat to the liquid Helium bath and the temperature exceeds the critical value T_c the supercon-

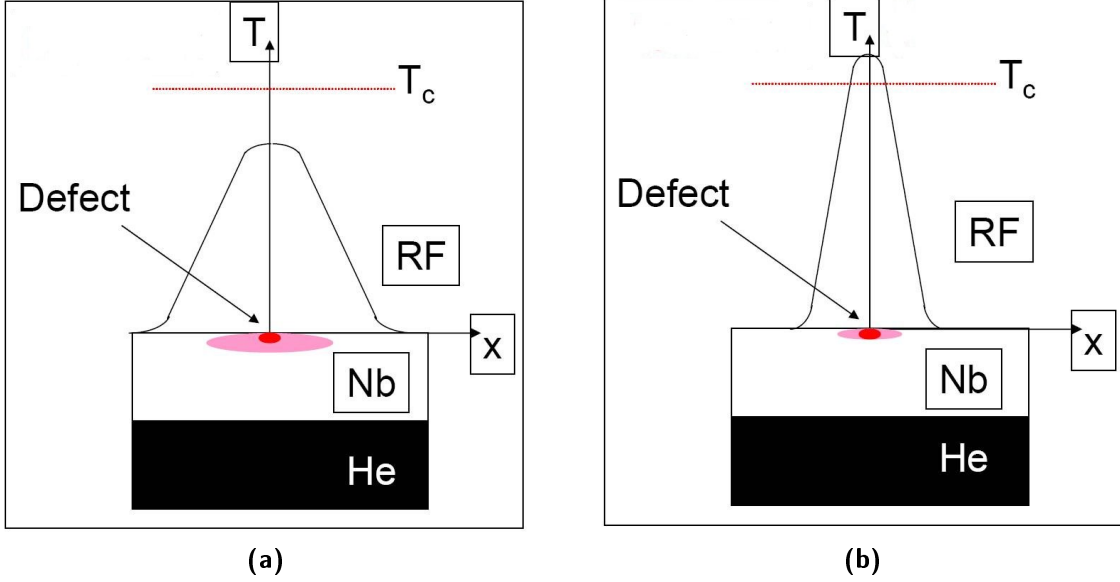


Figure 3.9: Schematic view of the thermal breakdown of superconductivity. Figure 3.9a: For lower fields the cooling of the defect by the surrounding material is sufficient to stay below the critical temperature. Figure 3.9b: For higher fields the excess heat from the defect is high enough to cross the critical temperature [38]

ducting state breaks down locally, producing even more heat and driving a large fraction of the cavity into the normal conducting state.

Initial experiments whether the instability is of thermal or magnetic nature were carried out by exciting both modes (the π - and the $\frac{\pi}{2}$ -mode) of a 2-cell cavity simultaneously [42]. By letting the cavity quench with different fractions of the two modes, the relation $H_\pi^2 + H_{\pi/2}^2 = \text{constant}$ was proven to be correct, corresponding to a thermal instability. In the case of a magnetic instability $H_\pi + H_{\pi/2} = \text{constant}$ would be expected. More recent experiments on three more cavities have given a more diverse picture [43]. With a more general approach of $H_1^\alpha + H_2^\alpha = \text{constant}$ values in the range of 1.35 to 1.9 for α were obtained.

Using the model of a local small defect with higher surface resistance, as mentioned earlier, one derives a maximum value for the magnetic field of a defect [38]. It assumes a hemispherical, normal conducting defect of radius a with surface resistance R_s embedded in the niobium surface. Considering the power dissipation in the defect and the heat flow from the defect to the surrounding niobium, the maximum value for the magnetic field, where the defect drives the surrounding niobium into thermal breakdown is given by:

$$H_{max} = \sqrt{\frac{4\kappa(T_c - T_b)}{aR_s}} \quad (3.12)$$

with the critical temperature of niobium $T_c=9.2$ K, the typical bath temperature $T_b=2$ K

and the average thermal conductivity for niobium of $RRR=300$ $\kappa=75$ W/(m K).

This very simple model only considers the static case, leaving out details like for example the temperature dependences of the BCS surface resistance of the surrounding material and the thermal conductivity. For a more elaborate consideration numerical simulations with an iterative solution to the heat flow equations can be used [44].

3.3.3 Multipacting

Multipacting ¹ describes a phenomenon where an avalanche of electrons builds up resonantly in the cavity. Depending on the secondary electron emission coefficient (SEEC) an electron impacting on the cavity surface will create additional electrons. The initial electron may be produced e.g. by cosmic rays or field-emission. The emitted electrons are accelerated by the component of the electric field perpendicular to the surface while the magnetic field bends the electron trajectories. If the electron trajectory and the RF frequency of the cavity meet a resonant condition, the electrons return and hit the surface at the same (or close to the) spot where they started and the number of electrons increases exponentially for an SEEC greater than unity. Electrons hitting the same spot form so-called "one-point multipacting". For "two-point multipacting" the electrons travel between two different points with a distance of the order of some mm to cm, e.g. two points left and right of the equator. The acceleration of the electrons consumes a significant amount of energy that can be noticed in a steep drop in Q , a so-called multipacting barrier. Even when feeding more energy to the cavity the accelerating gradient does not increase.

Most multipacting barriers can be processed by letting the cavity multipact for a couple of minutes. The electrons clean adsorbed gases from the cavity surface and the SEEC drops below unity. The location of the multipacting may move along the cavity surface during that process. Processed multipacting barriers remain "switched-off" as long as the cavity is kept under vacuum, after venting and contact with air the multipacting may return. One-point multipacting is a serious limitation for cavities of cylindrical shape. The spherical or elliptical shape that is now in use has been introduced to overcome this limit [45]. Since the magnetic field varies along the wall, electrons drift to the equator where no perpendicular electric field is present without forming stable resonant paths before. However some two-point multipacting sometimes is possible in the region of 17 MV/m to 22 MV/m [46].

3.3.4 Q-switch

The phenomenon known as Q-switch is visible in the $Q(E)$ -curve as a sudden drop of the quality factor when raising the rf power above a certain level, as illustrated in Fig. 3.11. The curve looks normal up to a field of 16 MV/m and then suddenly starts to drop to lower Q -values and respectively lower accelerating fields for rising power input. The origin usually is a part of material with "bad" thermal contact to the rest of the surface. The isolated part heats up and at a certain level becomes normal conducting causing excessive

¹The word Multipacting is a contraction of Multi Impacting

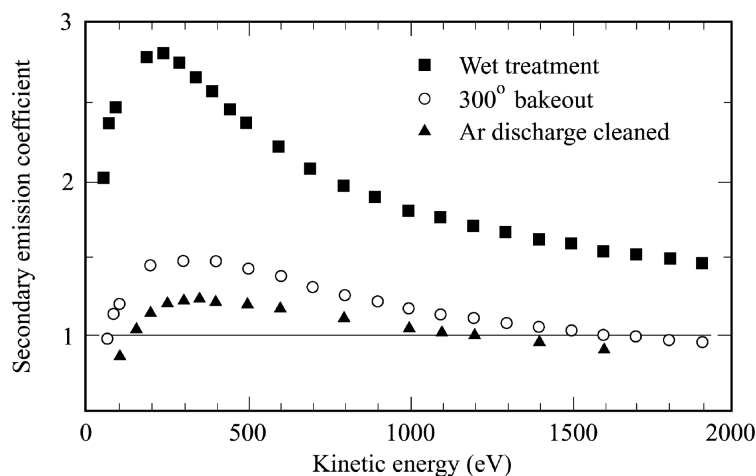


Figure 3.10: Secondary electron emission coefficient for niobium after different surface preparations [47]

losses. Due to the thermal isolation the heating stays localised and only lowers Q_0 due to the dissipated energy. The heat does not spread out and induces a thermal instability causing the whole cavity to quench.

In several cases Q-switches have been traced back to the region of the HOM-couplers via thermometry measurements. In this particular cases most likely parts of the HOM-coupler feedthroughs were heating.

3.3.5 Q-disease

Q-disease or hydrogen-disease is a phenomenon where the quality factor Q_0 of the cavity is low (10^8 to 10^9) at low accelerating fields in the absence of other Q_0 -limiting effects like field emission or multipacting. It occurs if hydrogen is present in the bulk niobium and forms niobium hydrides during cooldown [48]. Hydrogen can be introduced into the niobium during etching if the acid becomes too hot or if the hydrogen gas that is formed during electropolishing is not taken care of. The hydride formation is happening in the temperature window of 100 K to 150 K. The temperature dependence is determined by the solubility of hydrogen in niobium at different temperatures and the temperature dependence of the mobility of hydrogen in the material. One possibility to avoid the symptoms of Q-disease is cooling the cavity quickly through this dangerous temperature range. The shorter the time at that temperature, the fewer hydride can be built.

The other possibility is to cure the origin by removing possible hydrogen contamination from the niobium after chemical treatments by a heat treatment in vacuum, e.g. the 800 °C firing for 2 hours (see Section 4.2.4).

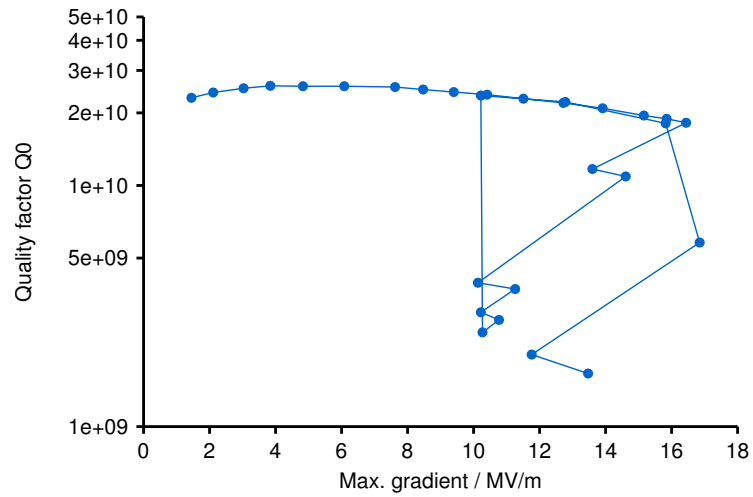


Figure 3.11: Example for Q-switches in a Q(E)-curve: The gradient increases smoothly up to 16 MV/m. From there it jumps back to lower gradients at lower Q_0 -values.

CHAPTER 4

Fabrication and Preparation of SRF cavities

4.1 Fabrication

The fabrication of TESLA-style nine-cell superconducting cavities starts with an ingot of niobium. For good superconducting properties the material has to be very pure in terms of foreign metals and elements that form interstitial impurities. On the metallic side tantalum is the main contaminant since the chemical properties of tantalum and niobium are very similar and both elements are always found together in the ore. A content of up to 500-1000 ppm (wt) distributed in the bulk as substitutional impurities is not considered to be harmful for the electrical performance [38], while localised inclusions of tantalum are problematic [49]. The interstitials are hydrogen, nitrogen, oxygen and carbon, with oxygen being the most important. Interstitials reduce the residual resistivity ratio (RRR) by acting as scattering centres for the electrons. The niobium ingot is purified by electron-beam re-melting in an ultra high vacuum (UHV) furnace, where the impurities "boil" out of the molten niobium. Several re-melting cycles are needed to reach the wanted low values for impurities. An overview of the desired values for impurity concentration and mechanical properties is given in Table 4.1.

Once the raw material reaches the desired purity, the sheet production from the ingot is started. For the standard material, the so-called fine-grain (FG) material with individual grain sizes on the order of few 10 μm , several steps of forging and rolling combined with grinding and polishing result in sheets of 2.8 mm thickness. In a newer approach, discs in the desired thickness are immediately cut from the ingot [50, 51]. Omitting the several steps of forging and rolling leads to a speed-up with possible cost-benefits of the material production process. In addition it results in grain sizes of up to several centimeters, therefore the name large grain (LG) material. A detailed description of the development of large grain cavities at DESY can be found in [52].

Each step of mechanically forming the FG material increases the possibility of introduc-

4 Fabrication and Preparation of SRF cavities

Table 4.1: Specification for the niobium used for the fabrication of the European XFEL cavities [27].

Electrical and mechanical properties		Main impurity content ($\mu\text{g/g}$)		
Property	Value			
Residual Resistivity Ratio	> 300	Ta	≤ 500	H ≤ 2
Grain size	$\approx 50 \mu\text{m}$	W	≤ 50	O ≤ 10
Yield strength	$> 50 \text{ N/mm}^2$	Mo	≤ 50	N ≤ 10
Tensile strength	$> 140 \text{ N/mm}^2$	Ti	≤ 50	C ≤ 10
Elongation at fracture	$> 30 \%$	Fe	≤ 50	
Vickers hardness	≤ 60	Ni	≤ 50	

ing particles of foreign material in the surface of the sheets. Therefore the sheets are checked for such inclusions with an eddy-current measurement, for highest sensitivities with SQUID-based measurement set-ups [53, 54]. From the sheets half-cells are created via deep-drawing. Using a die of the desired half-cell shape, the sheet is formed using a high-power press.

After the deep-drawing the equator and the iris side are trimmed. At the equator some additional length is kept to have a margin for length-adjustment after the next step. Since the resonance frequency of a cavity cell is highly dependant on the shape, the most sensitive way to determine the correct size of the half-cells is by a RF-measurement. Therefore a device for semi-automated half-cell measurement called HAZEMEMA as abbreviation for 'Halbzellenmessmaschine' (*english*: half cell measurement machine) was designed and built at DESY [55]. The machine can measure the resonant frequency of half-cells, dumb-bells and end-groups.

From the half-cells so called dumb-bells are welded by joining two half-cells at the iris. The used method for all welds on the cavity is electron beam welding (EBW). The two parts are pressed together and an electron beam is used to melt the contact area. For a smooth welding seam the beam is slightly defocussed and moved in a rhombic or elliptical raster pattern [56]. After re-solidification the two parts are joined. That way no foreign material is introduced into the welding seam. During the EBW the parts are inside a chamber with good vacuum conditions since the molten niobium would getter residual gas from the surrounding and RRR would degrade [35]. The dumb-bells are checked with the HAZEMEMA again and the final amount of trimming of the equators is calculated. The contour of the two pieces for the equator welding seam can either be formed as a butt weld or a lap weld (see Fig. 4.1. For the final step of the welding of the cavity the dumb-bells are joined with two end-groups, consisting of half-cells with beam-pipes, HOM couplers and flanges. Then all equatorial welds are done.

After fabrication the cavity has to be tuned in a way such that the electric field is the same in all nine cells in the π -mode. The ratio between the cell with the highest and lowest field is called field flatness. In addition, the cavity has to be adjusted to the correct frequency

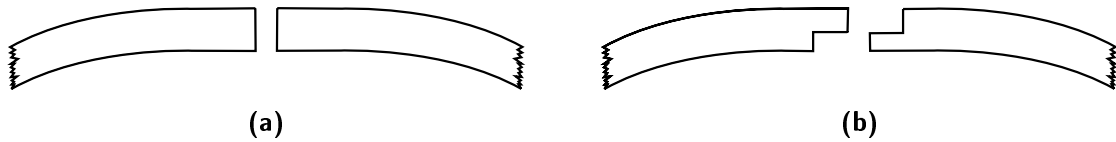


Figure 4.1: Two possible contours of the two half-cells before welding of the equator seam 4.1a: butt weld, 4.1b: lap weld

for later operation. Both goals are achieved by measuring the field profile and resonant frequency of the cavity and mechanically deforming the individual cells iteratively until both quantities reach the desired value of better than 98 % field flatness and 1.3 GHz. For the reliable, fast and easy tuning of the cavities during fabrication, an automated tuning-machine has been developed at DESY [57, 58].

The last production step, the welding of the cavity into the Helium vessel, is located at variable points in the production cycle, depending on the chosen surface preparation scheme (see Fig. 4.2)

A cavity fabrication method alternative to the above described is hydroforming [59, 60]. Instead of welding the cavity from preformed half-cells, it is formed from seamless niobium tubes by means of high water pressure. Thereby the welding seams in the region of high magnetic field at the equators can be eliminated.

4.2 Surface Preparation

In order to reach high accelerating gradients in superconducting cavities, the demands with respect to smoothness and cleanliness of the surface are very high. Therefore a lot of effort is put into the preparation of the cavity's inner surface. An overview of the main steps after welding of the equator seams is given in Fig. 4.2. After completion of the cavity-fabrication about 100 μm of the surface have to be removed. That eliminates the layer with mechanical damage and possible contaminations that have been introduced during the mechanical production process. This surface-removal is done by (electro-)chemical means. The chemical processes involve strong acids such as hydrofluoric acid. Thereby very high security standards for the protection of personnel and environment are mandatory. All final handling steps of the cavities where the inner part of the cavity is exposed to air are performed in the extremely dust-free environment of a clean room. The DESY clean room facilities include areas of clean room class ISO6 to ISO4 [61].

4.2.1 Buffered chemical polishing

One way for the uniform removal of material from the inner cavity surface is the so called buffered chemical polishing (BCP). An acid mixture is pumped through the cavity in a

4 Fabrication and Preparation of SRF cavities

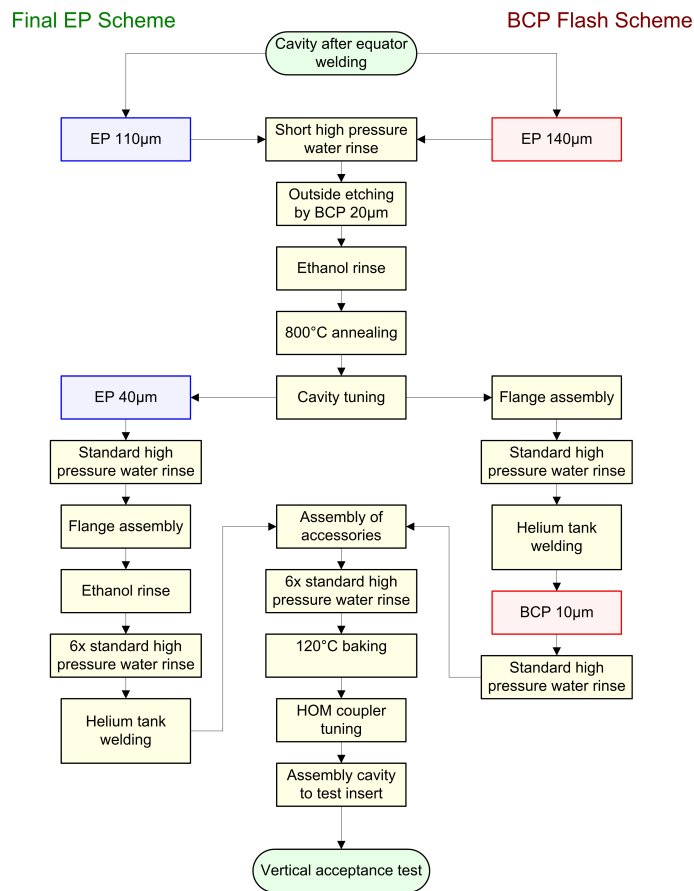
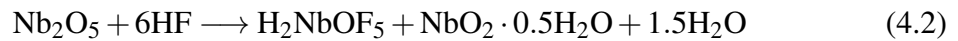


Figure 4.2: Preparation scheme for the preparation of cavities for the European XFEL with the two possible schemes "Final EP" and "Flash BCP" [62]

closed circuit and etches away the topmost layer of the surface. The acid in use for BCP at DESY is a 1:1:2 mixture of HF (48 %), HNO₃ (65 %) and H₃PO₄ (85 %) [35]. HNO₃ oxidises the Nb on the surface (Eqn. (4.1)), and the Nb₂O₅ is then dissolved by the HF, forming H₂NbOF₅ (Eqn. (4.2) and Eqn. (4.3)). The H₃PO₄ is acting as a buffer, slowing down the chemical reaction. Otherwise the reaction would be strongly exothermic and with a lot of released gases (H, HF, nitrous gases) due to the comparatively large inner surface of a nine-cell cavity. In addition the acid is cooled during the polishing process.



The highest gradients reached in cavities treated by pure BCP are in the order of 25 MV/m to 30 MV/m [35] [4]) consistently. In very few cases etched cavities have significantly exceeded gradients of 30 MV/m [63].

4.2.2 Electropolishing

A second possible method to remove material from the inner cavity surface is electropolishing (EP). As the name suggests, in addition to the pure etching as in the BCP an electric current is involved. The acid mixture for EP at DESY is a 1:9 combination of HF (45 %) and H₂SO₄ (96 %); the so-called "Siemens-recipe" [64]. One advantage of electropolishing over BCP is that the introduction of a voltage in the surface-removal process gives improved control of the process stability. The niobium wall of the cavity acts as the positive electrode (anode) and a hollow electrode made from pure aluminium is inserted along the centre axis of the cavity as cathode. The acid acts as electrolyte and is pumped from a reservoir through small holes in the cathode into the cavity and back into the reservoir with a flow rate around 10 l min⁻¹. When a voltage is applied a current starts to flow and by absorbing oxygen and electrons the niobium is oxidised to Nb₂O₅ (Eqn. (4.4)). In addition hydrogen forms at the cathode. The Nb₂O₅ is then dissolved by the HF as in the BCP process (Eqn. (4.2) and Eqn. (4.3)). There are several models about the exact mechanism of polishing during EP. Some [65] contain a viscous layer forming in the acid close to the cavity surface. Due to the surface roughness the layer is of different thickness at different locations (see Fig. 4.3). The higher viscosity is equivalent to a higher resistivity for the electrolytic current, so that at the protruding features with a lower thickness of the layer the current is higher. As a result protrusions are removed faster and the EP yields a smoother surface in general. The hydrogen gas forming at the cathode is problematic. Gas bubbles on the niobium surface could disturb the polishing process and hydrogen enters the bulk niobium. The cathode is wrapped in a Teflon cloth that breaks up the bubbles. The cavity is electropolished in horizontal position and the acid level is adjusted at about half the height of the cavity with the cathode completely covered. Hydrogen that leaves

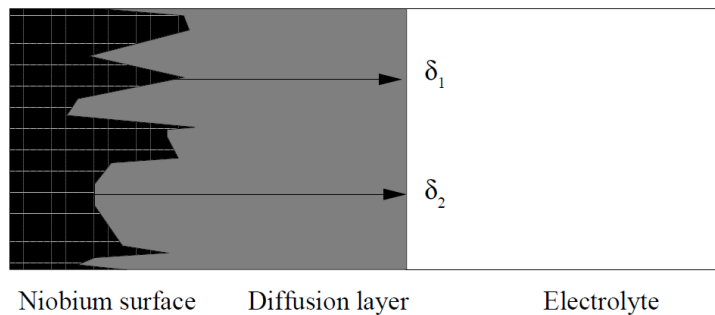
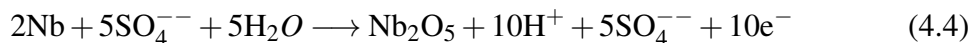


Figure 4.3: Viscous layer forming during EP and its different thickness due to protruding features and pits [35]

the acid at the surface is swept away by a steady flow of nitrogen. Since only half of the cavity surface is covered by electrolyte in this set-up the cavity has to be rotated. The rotation speed is about 1 rpm. Typical removal rates are in the order of $0.3 \mu\text{m min}^{-1}$ to $0.4 \mu\text{m min}^{-1}$ [66]. After the desired amount has been removed, the cavity is brought to vertical position to drain the acid from the cavity as quickly as possible and rinse with water several times until no acid is remaining.



One of the drawbacks of EP is the formation of sulphur in a reaction of the aluminium cathode and the acid [67, 68]. The sulphur segregates on the surface of the cavity and is a known source for field-emission [69]. Removal of the sulphur by high pressure water rinsing or ultra-sonic cleaning is not very effective. Therefore the cavity is rinsed with pure ethanol in a closed circuit system inside the clean room [70, 71]. The ethanol rinse of cavities as part of the standard treatment after the EP at DESY has shown to yield cavities with significantly less field emission [72]. The insertion of the cathode into the cavity bears the potential risk of touching parts of the inner wall, e.g. the protruding antennas of the HOM couplers or the irides. Contact between the electrode and the cavity could result in scratches or material transfer of Teflon from the cathode-wrapping or aluminium from the cathode itself onto the cavity. Therefore the tool for inserting the cathode has to be designed with great care to avoid any damage.

4.2.3 High pressure rinsing

To clean the inner cavity surface from particles and contaminations it is rinsed with high pressure jets of ultra pure water (UPW). During high pressure rinsing (HPR) water jets with high pressure (typically ~ 100 bar) from a spray-head with several nozzles are directed all over the inner surface of the cavity. The HPR set-up is situated inside the clean room. Drying of the cavity after the rinsing also happens inside the clean room.

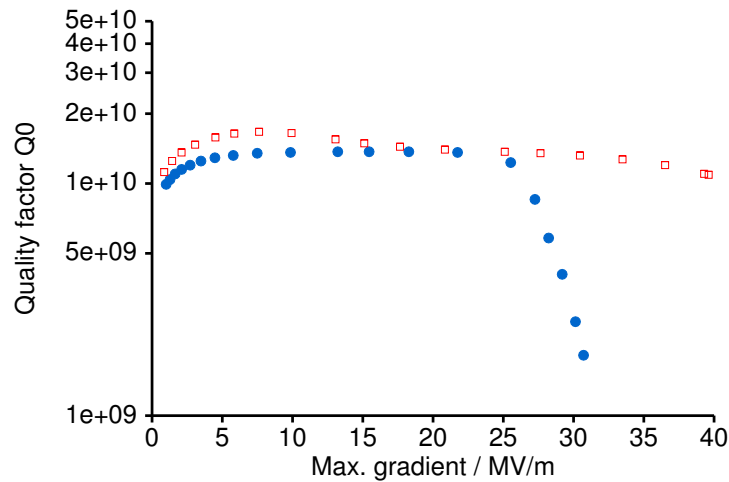


Figure 4.4: Impact of 120 °C bake on the Q(E)-curve of cavity 1AC8, before baking (blue circles) and after baking (red squares)

4.2.4 Heat treatment

800 °C heating

During the chemical treatment hydrogen is introduced into the Nb-surface. The cavity is heated in an Ultra High Vacuum (UHV) furnace for 2 hours at 800 °C in order to degas the hydrogen from the material. Otherwise Q-disease (see Section 3.3.5) may occur. In addition the high temperature treatment relieves mechanical stress that is present in the cavity after the deformation during the production process.

120 °C bake

Heat treatment of cavities at temperatures significantly lower than the 800 °C heating is also included in the treatment. Searching for a means to circumvent Q-slope a baking of the cavity at 120 °C for 48 h has proven to be effective. Figure 4.4 shows an example for the effectiveness. The first test was performed without baking and the quality factor Q_0 of the cavity drops steeply beginning at an accelerating voltage of 25 MV/m, limiting the performance to a maximum of slightly more than 30 MV/m. After the test the cavity was baked at 120 °C for 48 h, without any other modification of the cavity surface. In the second test the quality factor drops not as steeply and the cavity reaches up to 40 MV/m. The 120 °C bake is usually the last step before the vertical test with the cavity completely equipped and under vacuum.

CHAPTER 5

Cavity performance test at DESY

5.1 Test in vertical cryostat

In order to check if the manufacturing and treatment of the cavity succeeded and if it performs well, a RF-test under operating conditions, usually at 2 K, has to be done. Instead of the main-coupler that is later used for operation in the linac the cavity is equipped with an antenna for lower input power. There are two alternatives, either a fixed antenna or a variable antenna where a movement of the antenna and the cavity relative to each other is possible in order to adjust the coupling during the test. Feedthroughs for the HOM couplers can either be mounted or not. If HOM coupler feedthroughs are mounted, the RF power that is coupled out by them as well as their temperature are closely watched in order to prevent damage by overheating. Since the amount of power coupled out is too high for modes other than the π -mode, full mode measurements as described in Section 5.2 are not possible.

The cavity is lowered into a vertical cryostat in vertical position and connected to the vacuum system as depicted in Figure 5.1. The cryostat is then filled with liquid Helium, cooling the cavity to 4.2 K. From there on lower temperatures (down to 1.6 K if needed for special measurements) are achieved by lowering the pressure in the cryostat. Once the cavity is cooled down, the RF test can start.

In addition to the vertical test it is beneficial to be able to test the cavity in the exact configuration as it is operated in the linac afterwards. For this purpose the so called Chechia test-stand [73] is in operation at DESY. Here the cavity is tested in horizontal position and after welding to its He-vessel. RF-power can be fed via the main-coupler by a klystron with the same amplitude and time-structure of the RF-pulses as in the linac.

5 Cavity performance test at DESY

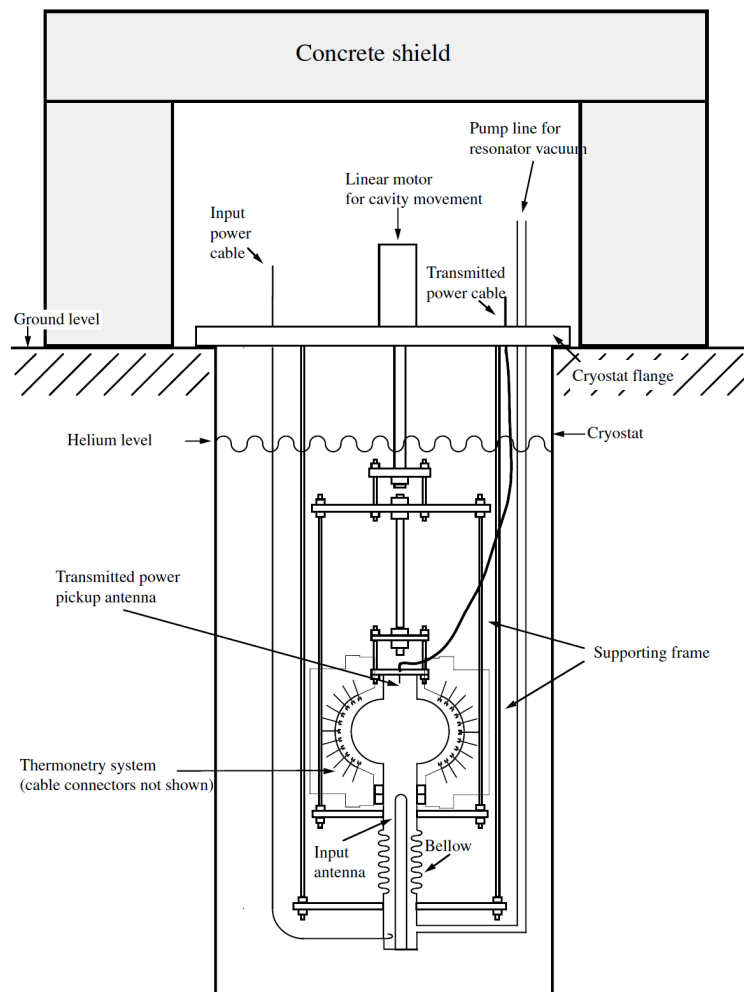


Figure 5.1: Schematic drawing of the vertical test cryostat, shown is a single cell cavity with attached fixed temperature mapping system and variable coupling [33]

mode cell	π	$8/9\pi$	$7/9\pi$	$6/9\pi$	$5/9\pi$	$4/9\pi$	$3/9\pi$	$2/9\pi$	$1/9\pi$
1	14	14	18	21	17	10	7	4	3
2	14	12	10	0	11	13	13	11	9
3	14	9	3	21	20	5	7	13	13
4	14	5	15	21	4	15	7	8	16
5	14	0	19	0	22	0	13	0	17
6	14	5	15	21	4	15	7	8	16
7	14	9	3	21	20	5	7	13	13
8	14	12	10	0	11	13	13	11	9
9	14	14	18	21	17	10	7	4	3
Limit:	BD	BD	BD	BD	BD	BD	BD	BD	BD
rf mode:	TM010	TM010	TM010	TM010	TM010	TM010	TM010	TM010	TM010

Figure 5.2: Accelerating gradient in MV/m for all cells measured in all nine modes. The white entries show the highest possible field for each cell.

5.2 Mode measurement

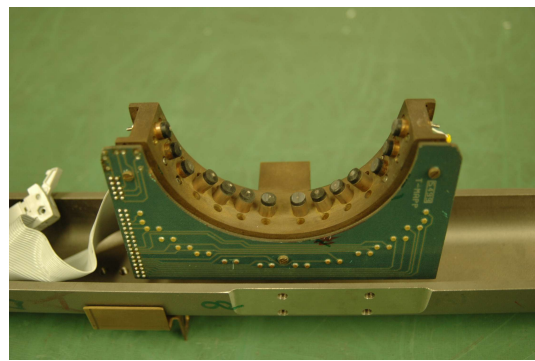
As described in Section 3.1 a nine-cell cavity has a fundamental spectrum of nine different resonant modes. In the π -mode the electric field has (ideally) the same strength in all nine cells. The quench of the weakest cell determines the maximum reachable electric field for the whole cavity. Other cells that possibly would reach higher values are not able to go up to their individual limits. By exciting the cavity in all nine modes one after the other it is possible to probe the individual limit of the different cells. An exemplary result of such a mode measurement is shown in Fig. 5.2. The table lists the breakdown field of all cells for the nine different resonant modes. Due to the fact that the field distribution is symmetric to the center cell, cell pairs 1 & 9, 2 & 8, 3 & 7 and 4 & 6 have the same field (see Fig. 3.3). In this case cells 2 & 8 reach with 14 MV/m the lowest gradient. All other cells are limited at 21 MV/m to 22 MV/m.

Mode measurement has two main benefits: With a rather quick measurement the candidates for the limiting cell can be narrowed down to two (or one, if it happens to be the center cell). In an additional vertical test this cells can then be further investigated in more detail. As second important output of the mode measurement more quench sites can be found and investigated. While the test of a cavity in the π -mode will only yield one quench site, the cavity will usually quench in more than one cell when excited in all different nine modes due to the different field distribution. This multiplies the number of possible defects that can be identified for further investigation.

A drawback of the method is that by the symmetry of fields there is the ambiguity between two cells as the limiting one. Also only the cell can be identified, not the exact position of the quench. Therefore mode measurement is usually combined with temperature mapping or second sound measurement, as described in the next sections, for a more precise result. In addition one has to be careful with the absolute values for the maximum gradient in some cases. The field strength for the individual cells is calculated according to the theoretical (ideal) field distribution based on the measurement at one point in the



(a)



(b)

Figure 5.3: Rotating temperature mapping system at DESY, 5.3a: Cavity in vertical insert with assembled temperature mapping system, 5.3b: Card with 14 sensors for one cell

cavity. The pick-up probe for the measurement of the transmitted signal is located at the beam-tube close to the end-cell. Especially in the lower modes ($2\pi/9$ and $\pi/9$), where the field in the end-cells is comparably low to the inner cells the computed values can be less precise. Also the field flatness has to be very good, else the calculated values have an additional uncertainty.

5.3 Temperature mapping

For a more detailed localisation of the quench position temperature mapping is applied. Thermo-sensors are placed on the outer surface of the cavity during the vertical test. They monitor the change in temperature that is created by defects or field emission on the inner surface. Covering the whole surface of a nine-cell cavity with good spatial resolution by fixed sensors would need a very high number of sensors. Therefore a rotating system is in use at DESY [74]. A cavity with assembled temperature mapping system is shown in Fig. 5.3a. A total of 116 sensors is distributed on cards with 14 sensors for the cells 2 - 8. On the end cells only 9 sensors can be placed since parts of the cell are covered by the conical discs. The detailed view of such a card is depicted in Fig. 5.3b.

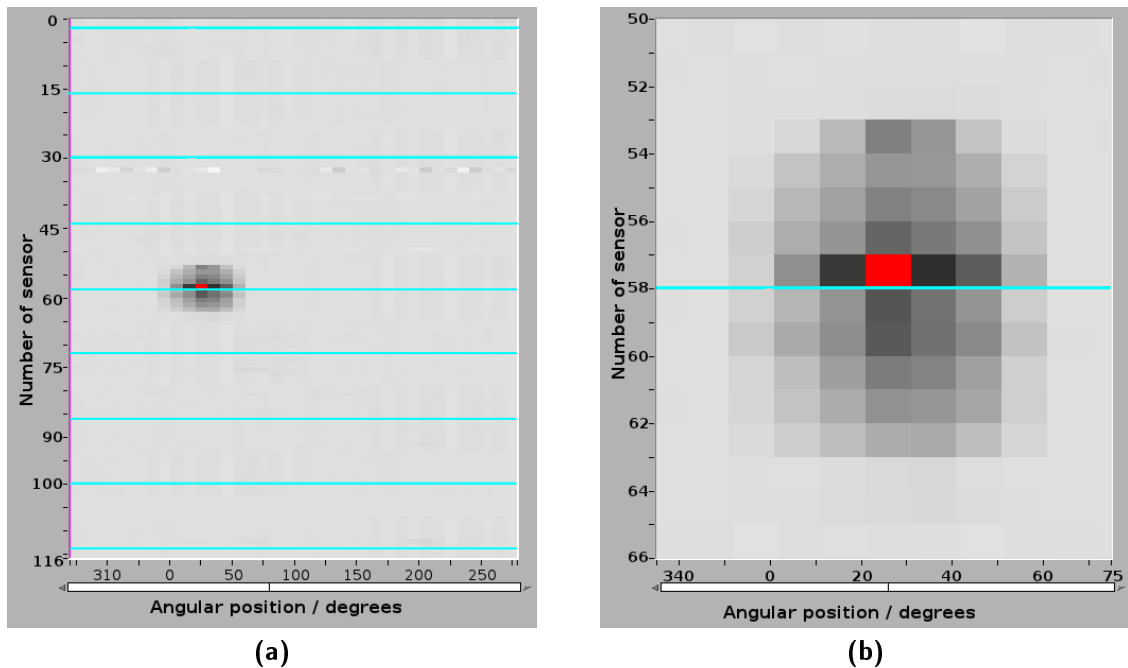


Figure 5.4: Typical result of a temperature mapping: 5.4a Full temperature map of all nine cells, equators are indicated by blue lines, the lowest cell has the number 1. The quench is situated in cell 5. Darker colour represents higher temperatures. The red spot is the hottest area. 5.4b Detailed view of cell 5

For obtaining a full temperature map of the cavity surface the sensors are set to one position, the cavity is driven to quench and the temperature change is recorded. Then the sensors are moved to the next position and the next measurement is started. The usual step size in-between the measurements is 10° . A typical result of such a temperature mapping is shown in Fig. 5.4. The left part of Fig. 5.4a shows the complete temperature map of the cavity for all nine cells. The angular position is on the horizontal axis while the vertical axis is labelled with the sensor number along the cavity axis. Numbering of the sensors starts with 1 in cell 9 at the top of the plot and ends with 116 in cell 1 at the bottom. The position of the equators is indicated by the blue lines. In this case, the cavity quenched in cell 5. Figure 5.4b shows a detailed measurement of the quench. Only a part of cell 5 is shown.

The advantage of the temperature mapping method is that, as the name suggests, a complete temperature map of the surface is obtained, showing not only location but also structure of the heating. For example the line-shaped heating patterns of impacting electrons from field emission can be seen on temperature maps. Also it is possible to make time resolved measurements and observe pre-heating of a defect if present. A full temperature mapping measurement however is time consuming. The measurement in all nine modes of a cavity takes several days. In addition the sensors have to be assembled and disassembled before and after every test, what takes a lot of time as well.

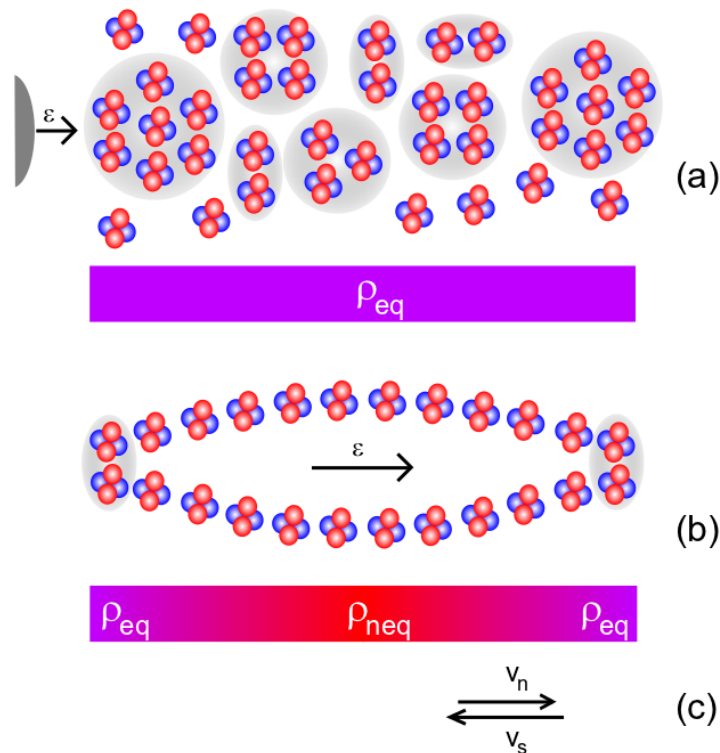


Figure 5.5: a) Mixture of superfluid Helium (groups with gray background) and normalfluid Helium (individual atoms) in equilibrium, energy pulse ε provided by quench at the left side, b) entropy wave disturbing the equilibrium, c) indicated movement to restore the equilibrium of the two components [75]

5.4 Second sound

Alternatively to the Tmap-system, the phenomenon of second sound can be used to determine the position of the quench during the vertical test.

Below its lambda point of 2.18 K at normal pressure Helium is in the superfluid state. The microscopic properties are best described in a two-fluid model as depicted in Fig. 5.5. An energy pulse as released at the quench site disturbs the equilibrium of the normal- and superfluid component by breaking up Cooper pairs from the superfluid state. The pulse propagates through the Helium in a wave-like motion, therefore the name second sound. At 1.8 K the propagation velocity is about 20 m/s.

Detection of the second sound wave is possible via Oscillating Superleak Transducers (OSTs). OSTs work similar to a condenser microphone. They consist of a housing with an insulated back electrode and porous membrane that is coated with a conducting material (e.g. gold) on the outer side. A schematic view of the detection of a second sound wave by an OST is shown in Fig. 5.6. The superfluid component is able to pass the membrane, the normalfluid helium can't. Thereby the membrane is moved by the pulse causing a change in the capacitance. With a DC voltage applied between the membrane and the

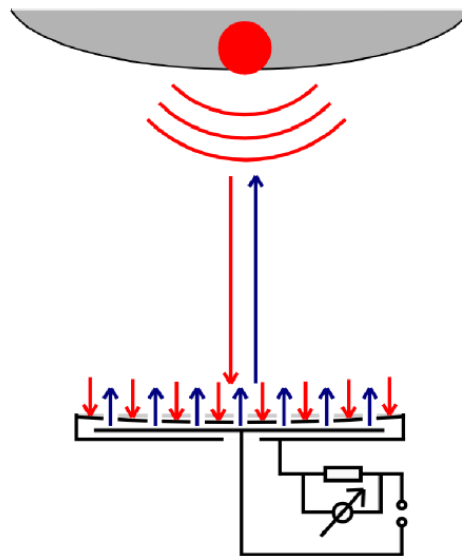


Figure 5.6: Schematic drawing of second sound detection with an OST: Superfluid Helium can cross the membrane while normalfluid is blocked. Oscillation of the membrane leads to a detectable signal. [77]

back-electrode the movement is detectable as a pulse. The first successful application of the OSTs for quench localisation in SRF cavities happened at Cornell University [76].

In order to determine the exact position of the quench spot on the cavity via second sound needs more than one OST. An array of OSTs (sixteen sensors in the current set-up at DESY) is placed around the cavity. When the second sound wave propagates to the different OSTs, different arrival times based on the distance between quench location and OST are can be measured. With a given propagation velocity of the second sound in superfluid helium the different arrival times of the signals are translated into the respective distance from the quench location to the OST. From all those distances and the known positions of the OSTs the position of the quench can be triangulated. The error for the obtained quench position is in the order of 5° in angular direction and 10 mm in longitudinal direction. An extensive description of the second sound set-up at DESY can be found in [78].

A big advantage of the second sound method over conventional temperature mapping, is that a small number of OSTs (compared to the number of sensors for a temperature mapping) is sufficient to detect quenches on the complete cavity surface. In addition, the OSTs are attached to the insert and can remain there, while the temperature mapping sensors are mounted to the cavity itself and have to be assembled and disassembled for every individual cavity and test. Also the measurement itself is quicker. In principle very few (in theory only one) quenches per mode of the cavity are needed for determining the quench location via second sound. A temperature mapping of the whole cavity with the rotating set-up in all modes takes several hours.

Since the second sound method is available at DESY numerous cavity tests have been

5 Cavity performance test at DESY

completed with temperature mapping and second sound measurement in parallel. The agreement for the location of the identified quench locations by both methods is very good [79].

CHAPTER 6

The optical inspection system

6.1 Motivation for an optical inspection system

The most interesting area of a cavity when investigating the thermal breakdown is the region around the equator. First, it is the area where the magnetic field on the surface reaches its highest value and thus can drive the cavity into a quench. And second, at the equator region the dumb-bells are joined by electron beam welding during the manufacturing process. The electron beam welding procedure is the best choice for joining the two parts and has been adapted and refined for the cavity production. Nevertheless it may influence the cavity performance if for example the welding seam is malformed with geometrical irregularities. In addition most defects have been observed in the vicinity or on the welding seam, although it is not always clear how the formation of such defects are related to the welding itself. Therefore an optical inspection of the equator region is desirable for quality control of the manufacturing process as well as for investigation of limiting features. The easiest way is to insert a commercially available borescope and looking at the surface, yielding images as in Fig. 6.1 and Fig. 6.2. The resolution is sufficient to see the welding seam and defects if they are large enough and are distinguishable from the surrounding material by high enough contrast. Smaller defects as well as the surface structure of the niobium can not be seen by such an instrument. Not only the limited resolution is problematic, but also the lighting with the point-like light-sources typical for borescopes is far from optimal.

A representative image of the equator region is shown in Fig. 6.3. The welding seam itself with a typical width of 3-5 mm is surrounded on either side by the heat affected zone (HAZ). The HAZ is the part of the niobium that has not been directly hit by the electron beam but the heat spreading from the welding seam was exceeding the re-crystallization temperature of niobium and lead to a larger crystal size. The HAZ may or may not be easily visible depending on the surface preparation status. Beyond the HAZ is the bulk

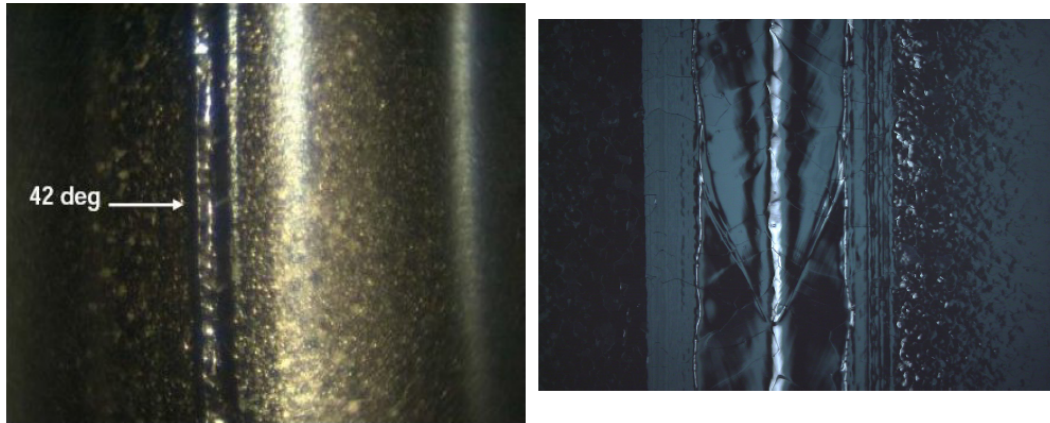


Figure 6.1: Comparison of pictures taken by the borescope system previously in operation at DESY (left) and by the Kyoto-camera system (right). The same v-shaped structure on the welding seam at 42 degree is visible in both pictures.

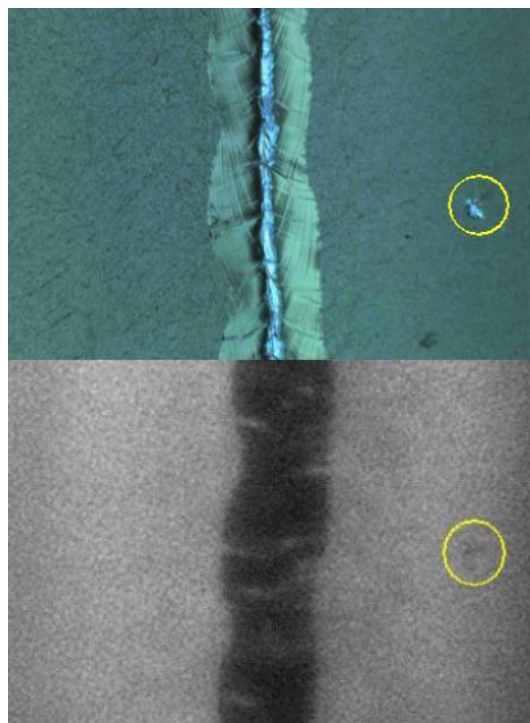


Figure 6.2: Comparison of images taken by a borescope system (lower part) and by the Kyoto-camera system (upper part). Both images show the same location. [80]

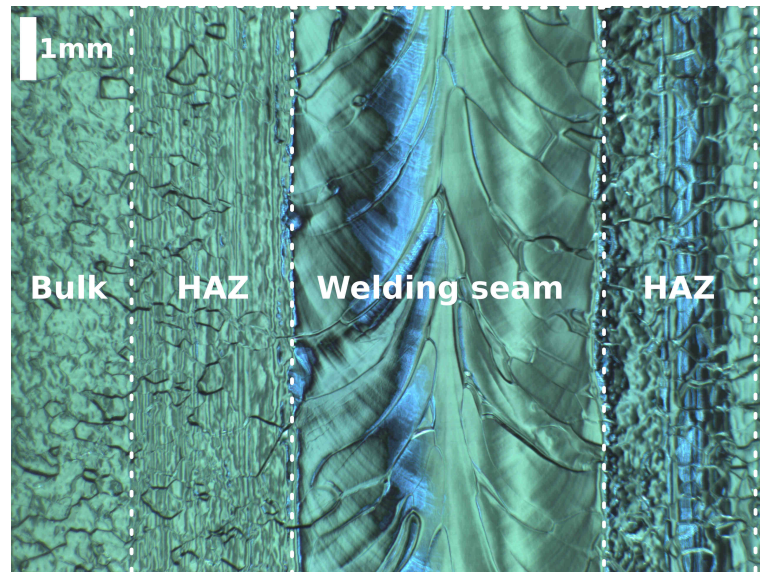


Figure 6.3: Relevant areas of an equator welding seam as obtained in optical inspection, indicated are the welding seam itself, the heat affected zone (HAZ) next to it and the bulk material

material that has not been influenced by the welding process. While the size of the welding seam and the HAZ are on the scale of some millimetres, defects are often significantly smaller, down to the order of micrometres. Hence an optical system that is capable to spot and investigate those defects needs a resolution smaller than $10\ \mu\text{m}$ but also has to have the possibility to see objects on the scale of some centimetres.

Even a defect free welding seam and surrounding area is not easy to illuminate at all. The niobium surface is extremely shiny, especially if electro-polished, and can create very bright reflexes of the incident light. Due to the cavity geometry the region is not flat and the welding seam can be protruding. In addition the seam has a pronounced substructure. Grain-boundaries, especially in large grain material cavities, may form significant steps in the surface. Defects can either be protruding or recessed into the surface forming pits and thereby are usually not well illuminated by a single point-like light-source.

Borescope systems neither satisfy the requirements in resolution nor illumination possibilities, which are needed for in-depth studies of the cavity welding seams and related defects or the surrounding niobium surface in different conditions. The inspection system that has been developed and will be described in the following section has been designed to provide the needed resolution as well as sophisticated illumination system.

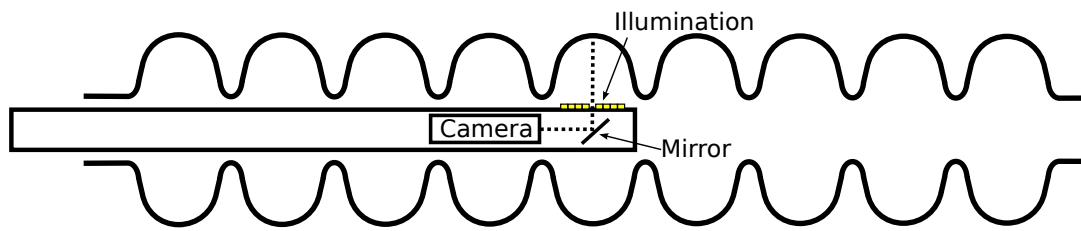


Figure 6.4: Schematic view of the camera system in use at DESY: The camera cylinder is inserted into a cavity

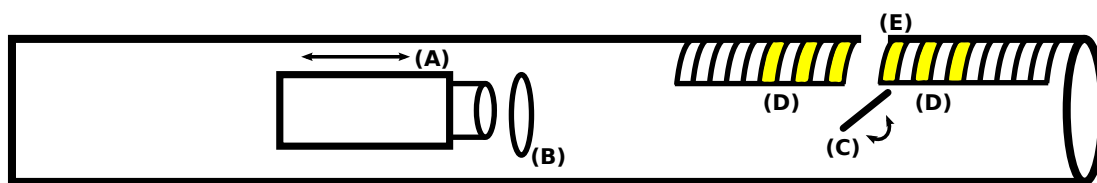


Figure 6.5: Detailed schematic of inner parts of the camera cylinder: (A) Moveable camera, (B) lens in front of camera, (C) rotatable mirror, (D) illumination system on both sides of the opening, (E) opening in the camera cylinder

6.2 Optical inspection tool

A schematic view of the system for optical inspection at DESY is depicted in Fig. 6.4. The camera is housed in a pipe that can be inserted into the cavity. It is looking in forward direction with a mirror directing the field of view towards the cavity surface. The illumination system is located on the outside of the tube around the opening for the camera. Figure 6.5 shows a detailed sketch of the camera pipe with its inner parts. The camera is sitting on a sledge and can be moved along rails in forward and backward direction by a stepping motor. This motion along the longitudinal axis is needed for focussing. By adjusting the distance between camera and surface the focal plane can be brought exactly to any feature of interest. In addition the differing equator and iris diameters are taken into account by moving the camera by the respective amount. 250 steps of the stepping motor are equivalent to 1 mm, guaranteeing the possibility for a very fine adjustment of the focus of the camera.

A mirror is positioned in front of the camera in order to direct the view of the camera from the forward direction to the cavity wall. The default position is a 45° angle for perpendicular inspection angle at the equator and at the iris. The mirror can be tilted around one axis. This allows to keep a perpendicular inspection angle for parts of the cavity in-between the equator and the iris. In order to inspect the whole cavity surface, the cavity is mounted to a fixture the allows its rotation around the longitudinal axis. A linear movement along the longitudinal axis of the cavity is possible as well.

The illumination system is located on the outer part of the camera tube. An array of stripes is located left and right of the opening for the camera. In addition, there is a central light inside the pipe that illuminates the surface in exactly the same direction as the view of

Table 6.1: Comparison of selected parameters for the camera systems version 1 and version 2

Parameter	Version 1	Version 2
Camera name	Toshiba Teli CSF5M7C3L18NR	Artray Artcam 900MI
Sensor type	3-layer CMOS	CMOS
Sensor size	1/1.8" 7.18 mm x 5.32 mm	1/2.3" 6.17 mm x 4.55 mm
Number of pixels	1480 x 1080 (physical) 1400 x 1000 (used)	3488 x 2616
Pixel size	5 μm	1.75 μm
Lens	VS-LD75 f/2.5 f=75mm	LM75JC1MS f/2.5 f=75mm
Effective resolution for g= 150mm	8.5 $\mu\text{m}/\text{pixel}$	3.5 $\mu\text{m}/\text{pixel}$
Connection	Firewire 400	USB 2.0
Illumination technique	electroluminescence	LED + light-guides
Number of illumination stripes	2 x 7	2 x 10 + 1

the camera under a 0° angle. All lights can be switched on and off individually and the intensity of the stripes as well as the central light can be dimmed. Being able to adjust the illumination is extremely important. The light of different stripes reaches the surface under different angles. Since the surface of the cavity, especially at the welding seams and at defects, is not completely flat, that allows to adapt to the surface topology and gain optimal illumination. In addition, the illumination of a defect from different directions with the individual stripes allows a measurement of the angle of the wall, resulting in the information whether the structure is a pit or a bump together with an estimate of the depth or height (see Section 6.2.3) of the defect.

The set-up for optical inspection of cavities at DESY is based on the camera that has been developed at Kyoto University and KEK [81]. The core parts of the system are the high resolution camera and the special illumination system. Two versions have been used at DESY. The first system was in operation from August 2008 and has been replaced by an improved version in October 2009. A comparison of the technical facts of the two cameras can be found in Table 6.1. The most important difference between the two cameras is the improvement in resolution from 1.5M pixel to 9M pixel. The second is the change of the illumination system. The first version was equipped with 2 x 7 electroluminescent stripes, while the second version was changed to 2 x 10 + 1 stripes. A combination of LEDs with light-guides is used to improve the variability of illumination, the maximum brightness and the durability of the illumination stripes. This change of the illumination technique also affects the colour of the images that are taken with the inspection system. The same surface appears to be more blue when inspected with version 1 and more green when inspected with version 2.

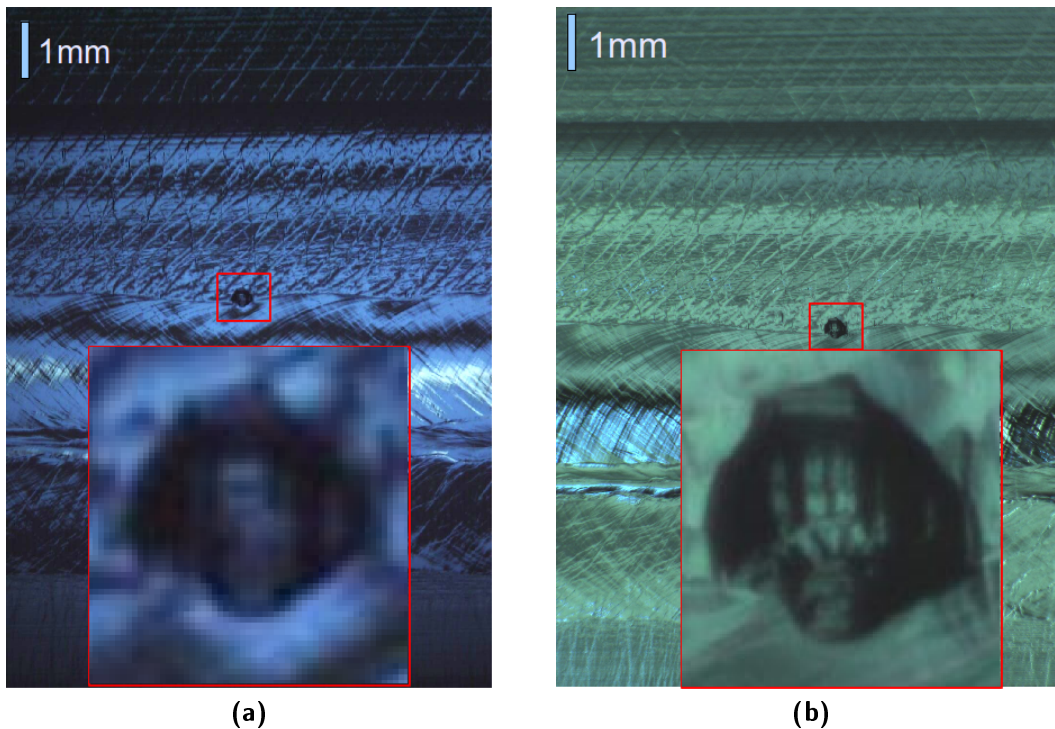


Figure 6.6: Comparison of images taken at the same location by the two different camera and illumination system versions. Note the change in color from blueish (6.6a) to greenish (6.6b) and the increase in resolution. The superimposed square on both depicts a magnification of the small boxed area.

The effect of the upgrade on the images is visible in Fig. 6.6. The more blueish image in Fig. 6.6a is taken with the old system. The greenish image in Fig. 6.6b stems from the new system. The increase in resolution of the camera is most visible in the magnification of the defect in the superimposed squares.

6.2.1 Camera properties and image size

An image taken with the camera in version 1 is equivalent to an area on the cavity surface of 8.5 mm x 12 mm and 9 mm x 12 mm in version 2. Taking into account the number of pixels of the sensors, the lens in front of the camera (see Table 6.1) and the object distance of $g = 150$ mm the effective resolution is 8.5 μm for system 1 and 3.5 μm for system 2. That resolution is sufficient to recognize features on the surface which are in the order of several 10 micrometres.

When changing from inspecting the equator to the iris, the camera is moved by the distance corresponding to the change in diameter keeping the focal plane fixed on the cavity surface. Thus, the covered surface area and with it the resolution is the same for equator and iris. At the equator the 9 mm image height correspond to an angle of 5° . For an in-

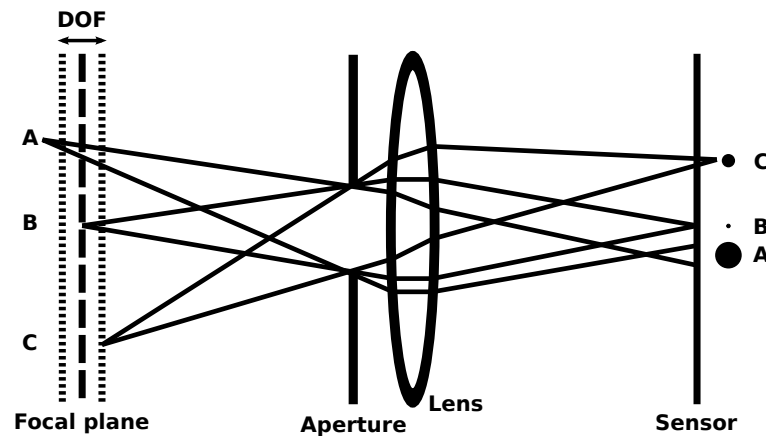


Figure 6.7: Illustration of depth of field: Points A, B and C are projected onto the sensor by lens and aperture. Depending on their position inside or outside the depth of field, they appear as a bigger point ("circle of confusion") on the sensor. A is outside the depth of field and appears defocused. B and C from inside the depth of field appear sharp.

spection of the whole equator images are taken in steps of 4° in order to have an overlap from image to image. This results in 90 images per equator. The diameter at the iris is smaller by a factor of three, resulting in an angle of 15° per image. At the iris images are taken all 10° .

6.2.2 Depth of field

The depth of field describes the distance between the nearest and the farthest object that appear sharp in an image taken by an optical system such as the combination of a camera with a lens. Figure 6.7 illustrates the depth of field. A system of a lens and an aperture projects three points, (A,B and C) onto a sensor. Point B is exactly in the focal plane and thus appears as a point on the sensor. Points A and C outside of the focal plane appear as circles. As long as this so-called circle of confusion is smaller than the resolution it appears sharp. Point C is just small enough to appear sharp. In other words, the depth of field is the region around the focal plane where the resulting circles of confusion are smaller than the resolution.

The tolerable size for the circle of confusion can be deducted from the acuity of the human eye, that is typically 1 arc second. The diagonal of an image viewed from a typical viewing distance has about 3000 arc seconds. A blur will be noticeable from 2 arc seconds on, so for an image taken by a sensor of diagonal size d the tolerable circle of confusion will be

$$Z \approx \frac{d}{1500}. \quad (6.1)$$

For a calculation of the depth of field, first the hyperfocal distance d_h has to be determined:

$$d_h = \frac{f^2}{k \cdot Z} + f \quad (6.2)$$

with f the focal length of the lens, k the aperture and Z the size of the circle of confusion for the given camera sensor. The hyperfocal distance represents the distance for which all objects that are between d_h and infinity appear sharp, if the lens is focussed at infinity.

Knowing d_h the region, which is depicted sharp can be calculated. This region is limited by the near point d_n and the far point d_f :

$$d_n = \frac{g}{\frac{g-f}{d_h-f} + 1} \quad (6.3)$$

$$d_f = \frac{g}{\frac{f-g}{d_h-f} + 1}. \quad (6.4)$$

g is the object distance.

The depth of field Δ_d is exactly the width of the above mentioned region:

$$\Delta_d = d_f - d_n. \quad (6.5)$$

With the values for camera sensors and lenses in version 1 and 2 (see Table 6.1) and the object distance $g = 150$ mm the depth of field evaluates to $\Delta_{d,1} = 61 \mu\text{m}$ for the system version 1 and $\Delta_{d,2} = 51 \mu\text{m}$ for the system version 2. Since the distance between camera and cavity surface is kept constant, the depth of field is the same for the equator- and the iris-images.

A large value for the depth of field gives the possibility to take images of objects with a large differences in heights, still all details appearing sharp. The surface roughness originating from grain boundaries for fine-grain cavities treated by BCP and EP is on the order of $2 \mu\text{m}$ to $5 \mu\text{m}$ [82]. The typical height differences in the welding seam and also steps at grain boundaries in large-grain cavities are within the range of the achieved depth of field, so that all features in one image can typically be sharp at the same time.

The depth of field of $50 \mu\text{m}$ to $60 \mu\text{m}$ is very sensitive to cavity positioning and deviations from the ideal round shape. During the inspection of a complete cavity the focus has to be adjusted numerous times. That requires either the continuous presence of an operator during optical inspection or the implementation of an autofocus mechanism.

6.2.3 Illumination system

The illumination system has been designed in such a way that it is able to produce very variable illumination patterns that suit the surface conditions of the cavity. Since the whole surface has more or less the same color, sufficient contrast has to be achieved by a combination of the illumination from different angles adapted to the surface structure. Illumination with an extended uniform light-source would yield an uniformly lit surface.

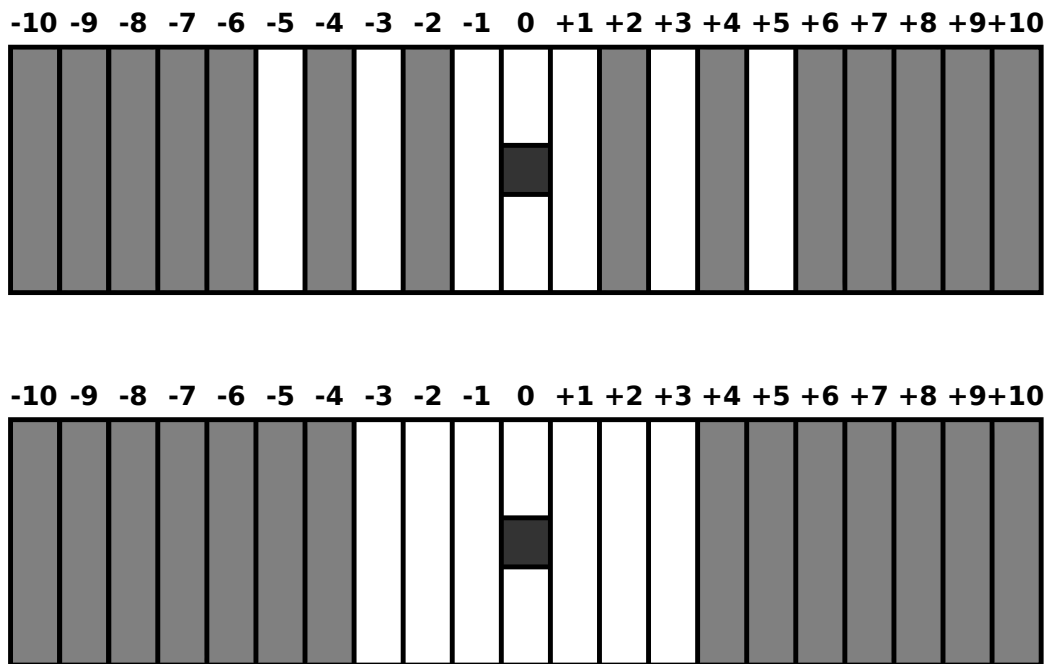


Figure 6.8: Standard illumination pattern for equator (upper part) and iris (lower part). Stripes are numbered from left to right, starting with -10 and ending with +10. Grey stripes are switched off, white stripes are switched on. The dark square in the center indicates the opening for the camera.

By alternating stripes that are switched on and off, the light reaching the surface from different angles creates areas of higher and lower illumination. The best illumination setting is one with maximum contrast where all areas are visible. Figure 6.8 shows patterns of illumination, which are routinely used for images at the equator and iris. While adapting the illumination for each image might improve the quality of the image even further, those above mentioned patterns have proven to give satisfying illumination in almost all cases.

In addition to maximising the contrast, the ability to switch the stripes of the illumination system individually gives the possibility to measure the topology of the cavity wall and determine whether a defect is a pit or a bump. An image of the area of interest, illuminated by only one stripe, is taken several times changing the stripe from image to image. Thereby the light is shining on the surface from a different angle for each image. If the reflection criterion is met for the given combination of stripe and angle of the wall at the defect, the surface yields a bright reflex in the image. Since the geometry of the set-up, e.g. distance from camera pipe to cavity surface, position of the illumination stripes, is known (see Fig. 6.9) the angle of the surface θ can be calculated. This method to obtain the profile and an estimate for the defect height or depth has been verified by comparison of the obtained values with the measurement by a laser microscope [83].

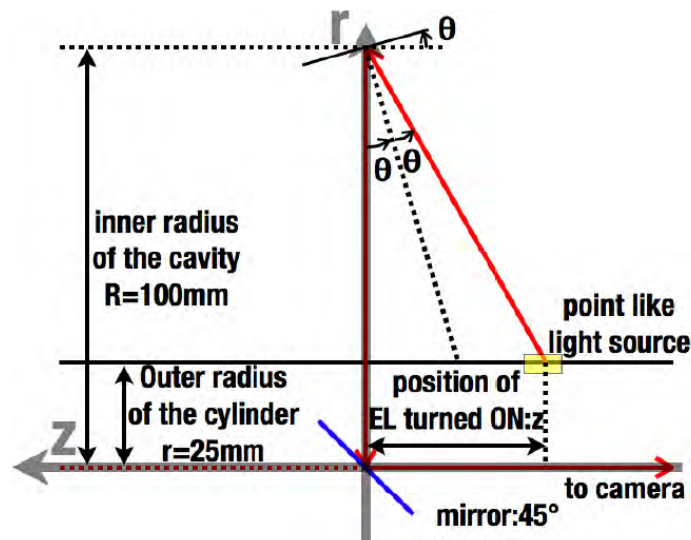


Figure 6.9: Geometric view of set-up for the measurement of the surface profile. From the known distance from the mirror to the cavity wall and the position of the lit illumination stripe the angle of the wall θ can be calculated [84]

6.3 Coordinate system

For the unambiguous description of the location of a defect on the cavity surface it is required to define a suitable coordinate system. The coordinate system in use for the optical inspection at DESY is described in [85] in detail. Beginning perpendicular to the input coupler flange the angle ϕ of this cylindrical coordinate system is counted clockwise when looking at the cavity from the short-endgroup side (see Fig. 6.10a). The iris- and equator-welds are numbered along the z -axis that points from the input coupler side to the long-endgroup side (see Fig. 6.10b). Considering an individual image from optical inspection, the absolute coordinates are often omitted. The location of a defect is then described by the cell number, the angle ϕ and the (projected) distance in the image from the welding seam.

6.4 OBACHT

The process of manually inspecting a complete cavity with the system as described above is time consuming and tedious. With 90 pictures per equator and 36 pictures per iris, the complete inspection including all nine equators, eight irides in-between the cells and the two transitions to the beam-pipes sums up to 1170 pictures. In the initial set-up all steps like positioning the cavity for the next picture, taking the picture and saving it with the correct file name including the position information have to be done by the operator. The complete inspection takes several hours, up to two working days.

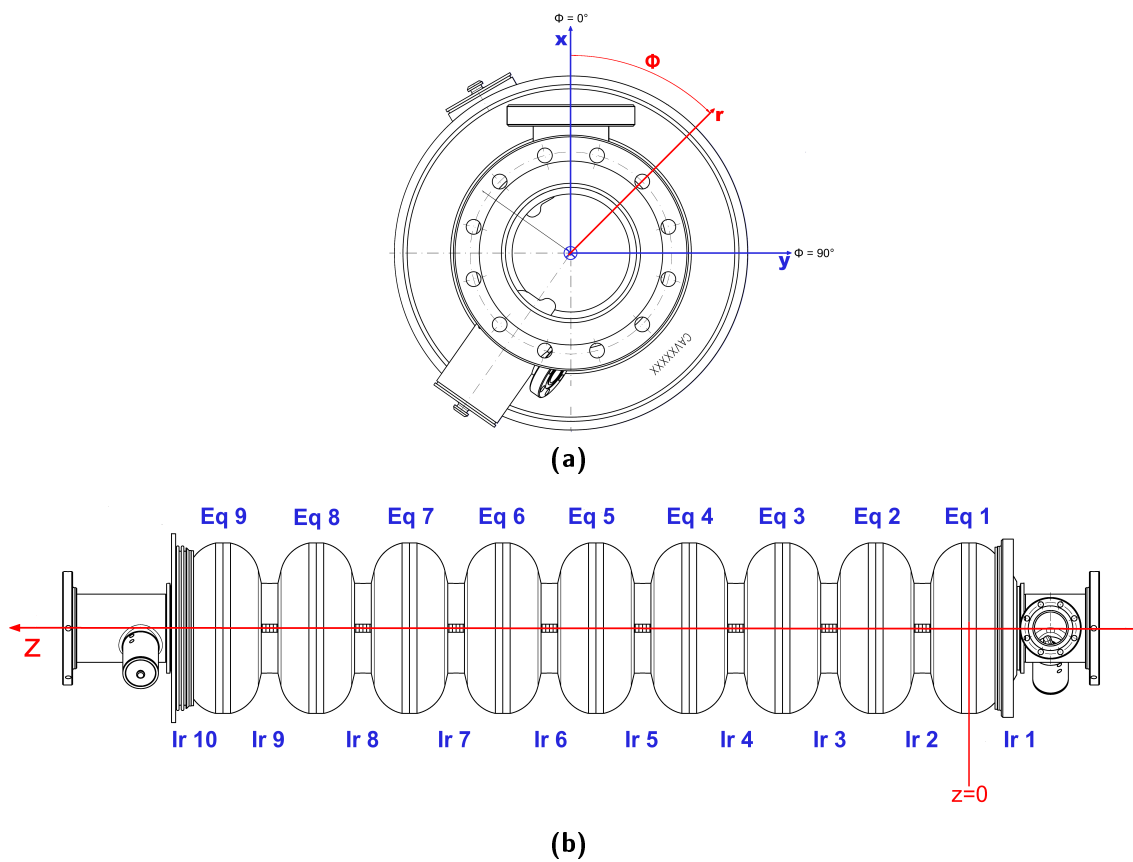


Figure 6.10: Definition of the cavity coordinate system. 6.10a: View of the cavity in the $r\phi$ -plane, $\phi = 0^\circ$ is perpendicular to the input coupler flange. The z -axis is pointing into the cavity. 6.10b: View of the cavity in the rz -plane with naming convention for the equators and irises. The origin of the coordinate system is in the first cell. [85]

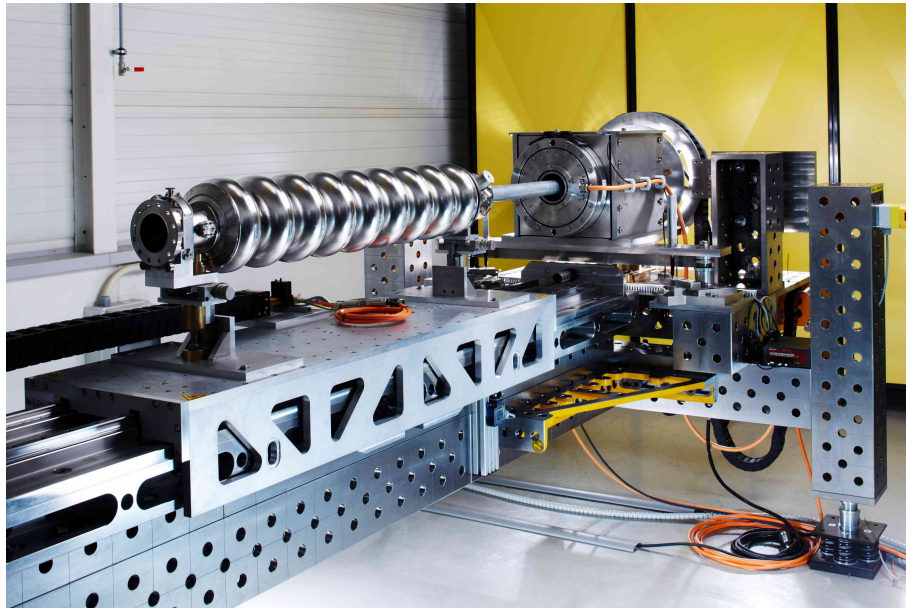


Figure 6.11: Photograph of the OBACHT setup

The first version of the camera cylinder was designed such that the direction of the camera was fixed pointing upwards and the cavity rotated, in order to cover the whole surface in angular direction. For a cavity without helium-vessel this is no problem, as the cells are rotationally symmetric around the beam axis and the cavity can be rotated easily by rolling on them. As soon as a cavity is welded to its helium-vessel, that symmetry is no longer accessible as the two-phase helium-pipe is sticking out off-axis on one side of the vessel. In addition the mass that has to be rotated increases significantly and is not as well balanced as in the case of a bare cavity. Therefore it is easier to rotate the camera. This aspect has been taken into account as of the second version of the camera system.

When studying the effects of the cavity treatment on the properties of the cavity surface, it is important to reproducibly take pictures at the same positions. With the manual positioning of the cavity and the manual "read-out" of the coordinates that the camera is looking at, the reproducibility is about 0.5 mm in the longitudinal and 0.5° to 1° in angular position.

All these experiences and requirements led to the design and construction of a new inspection system named OBACHT (**O**ptical **B**ench for **A**utomated inspection of **C**avities with **H**igh resolution on short **T**imescales). A photograph of OBACHT is shown in Fig. 6.11.

The main field of application for OBACHT is R&D in a laboratory. Therefore it has to be flexible in use with possibilities for modification. But it was also designed in such a way, that it could be deployed in the production environment of a cavity manufacturer. This demands robustness and reliability. A summary of technical details of the set-up can also

be found in [86].

The support structure is made of massive building blocks. They are precision-machined and have a breadboard-like raster of holes that allows maximum flexibility for adding of additional components or instruments later. The structure is resting on vibration damping feet. Together with the high mass of the whole structure this minimises vibrations that would otherwise affect the process of taking sharp pictures with the camera.

The cavity is mounted on a sled that is moved by a linear motor. The mounting structure for the cavity is designed in such a way that it can hold cavities without and with He-vessel. The camera cylinder is clamped into a rotating motor. The maximal possible rotation is 540° , so that enough margin is available for inspection of the whole 360° that are needed.

The motors are controlled by a programmable logic controller (PLC) and the overall control of the PLC and the camera as well as the illumination is implemented in LabView.

CHAPTER 7

Results of cavity inspections

7.1 Examples of inspected surfaces

The inspection of cavity surfaces reveals a zoo of features that differ from the standard uniform surface and welding-seams which are desired. In the scope of this work all in all 32 different 9-cell cavities, four 1-cell cavities and one 3-cell cavity have been inspected. The following paragraphs introduce and describe a collection of features that have been found in these inspections.

7.1.1 Standard welds

In Fig. 7.1 and Fig. 7.2 examples of a standard equator and an ideal iris weld are shown. The standard equator welding seam as shown in the middle of the image is broad, smooth and straight. The only visible surface-structure are grain-boundaries and the v-shaped re-solidification lines. Those re-solidification lines form when the cavity rotates under the electron beam during the welding. That causes the molten material to be "dragged along". The orientation is depending on the direction of rotation during the welding. Thus it may differ from cavity producer to producer and images taken in different cavities can have the v-shapes either pointing up- or downwards. The surface in the heat affected zone next to the welding seam is smooth to the intrinsic roughness of the individual grains on micrometer level.

The iris welding seam is smooth and straight as well (Fig. 7.2). The difference in colour of the equator and the iris image is due to the difference of the illumination technique (see also Section 6.2). Illumination is not as uniform as for the equator, since the iris is a lot closer to the camera cylinder. In addition, the surface moves out of focus much faster than at the equator due to the stronger curvature of the iris region. The illumination of the iris becomes even more challenging after surface treatment (Fig. 7.2b). Due to the extremely smooth surface the contrast between light and dark areas is more pronounced and the overall intensity has to be turned down in order to avoid overexposure of the reflecting

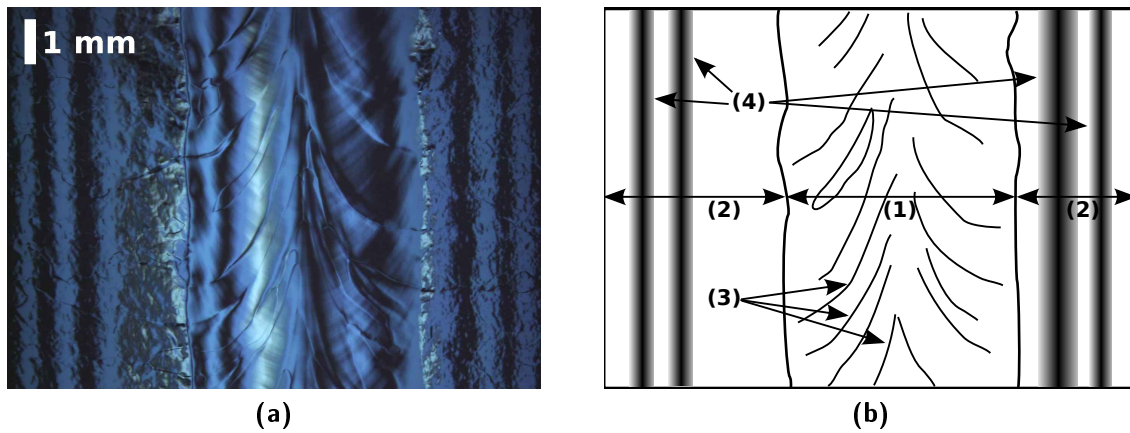


Figure 7.1: Example for an equator welding seam. 7.1a: Image as taken by the inspection system. 7.1b: Sketch with indicated features of interest. The welding seam (1) in the middle is flanked by the heat affected zone (2) on the left and right. The welding seam is covered by v-shaped re-solidification lines (3). Alternating areas of light and shadow (4) are created by the illumination.

areas. In addition the smooth and feature-poor surface makes it more difficult to adjust the focus than at the equator.

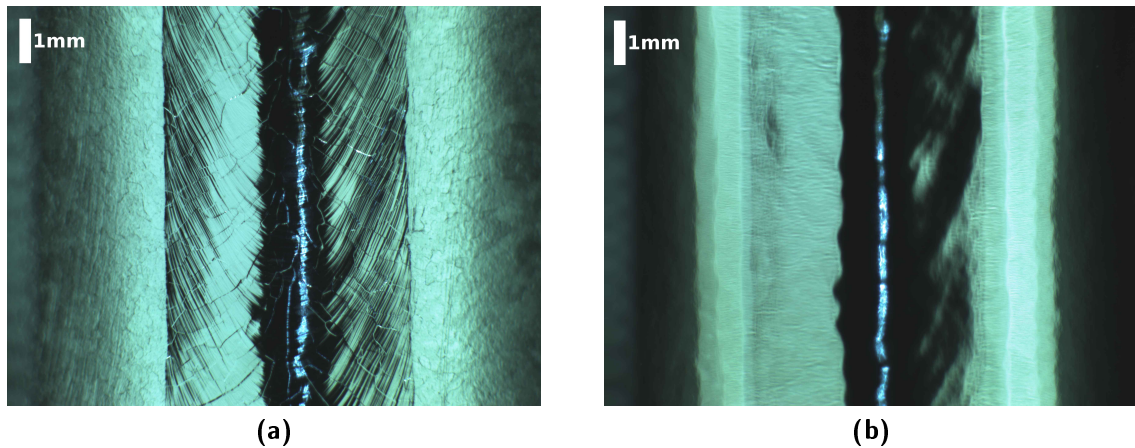


Figure 7.2: Example for a normal iris welding seam. Both images show the same location. 7.2a: Image before surface treatment. 7.2b: Image after electro-polishing. The surface is extremely smooth, making focussing a difficult task. The illumination setting is the same for both pictures. The difference in brightness and contrast originates from the change of the surface properties.

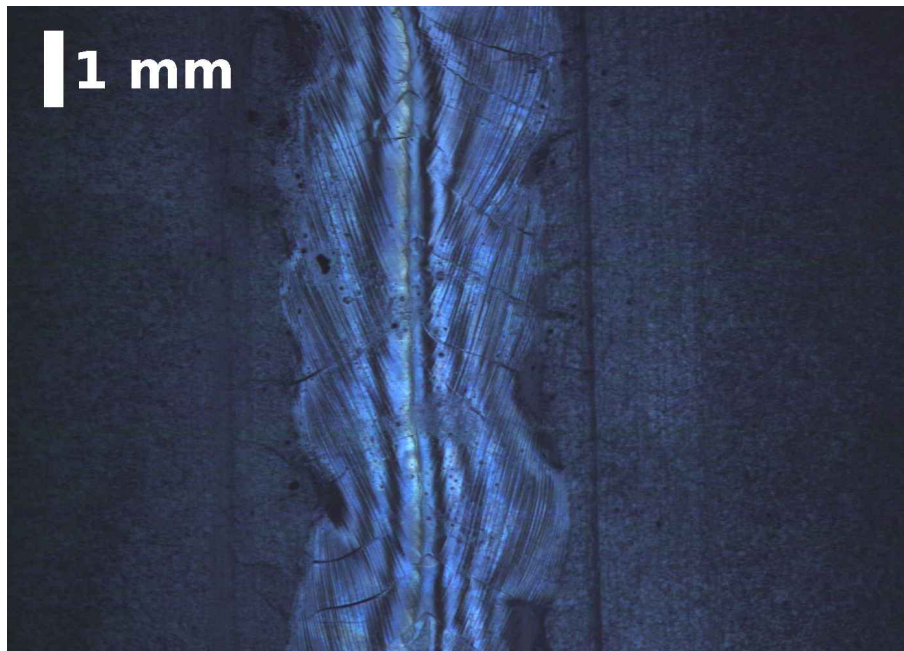


Figure 7.3: Curvy equator welding seam

7.1.2 Non-straight welding

In Fig. 7.3 an example for a non-straight welding seam is shown. Even though the central ridge of the seam is straight, the left and right edge of the seam are extremely wiggly. This indicates a non-stable welding process. Parameters that have to be kept stable in order to achieve a straight welding seam are e.g. the rotation of the cavity and intensity and positioning of the electron beam. In addition, if the cavity is not properly grounded it may charge up electro-statically and the electron beam can be deflected.

7.1.3 Weld-overlap

During the welding process after one full rotation there is an overlap where the electron-beam passes a second time. In Fig. 7.4 this area can be seen. When the electron beam is switched off, it forms a v-shaped structure on the welding seam while fading out. The v-shape is in the lower part of the image. The dark spot in the center of the image is an area that could not be illuminated completely.

These overlaps can usually be seen in the optical inspection directly after fabrication. After material removal in the surface preparation process they are usually not visible any more.

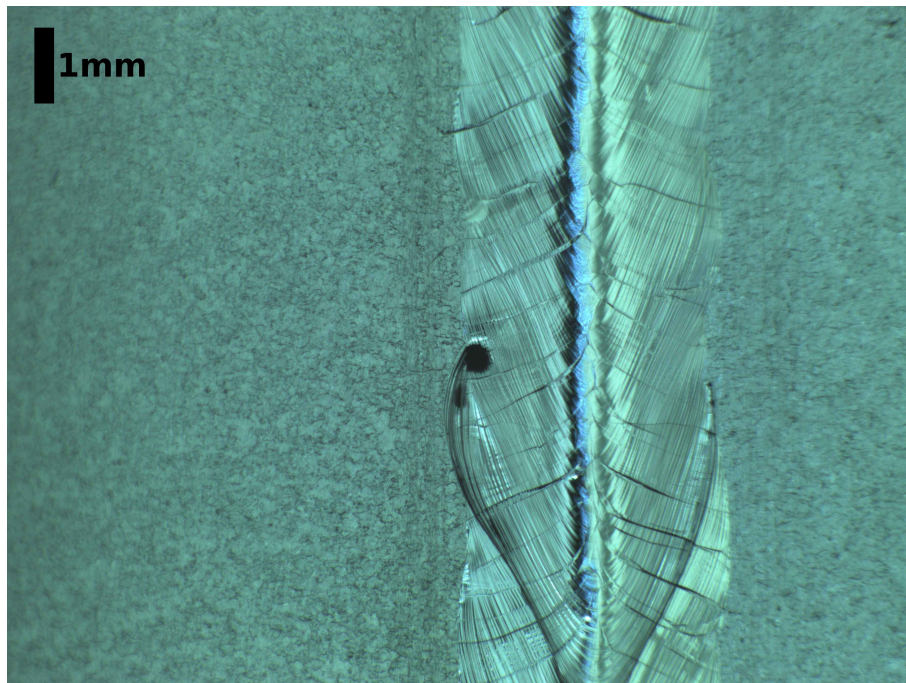


Figure 7.4: Zone of welding overlap at equator seam. The v-shaped structure is created by the electron fading out before being switched off. The black spot is an area that could not be sufficiently illuminated.

7.1.4 Welds in LG material

The surface of large-grain material cavities differs significantly from fine-grain ones. Grain size is on the order of up to several cm, so that grain-boundaries are not seen in every image. Figure 7.5 is an image of the equatorial welding seam with grain-boundaries. In this case a grain has formed reaching from the heat affected zone into the welding seam, forming a closed contour. The grain-boundary forms a steep step of some 10 micrometer. The whole grain lies deeper than the surrounding material by that amount. After electro-polishing (Fig. 7.5c) the surface of a large-grain cavity is extremely smooth. The steps at the grain-boundaries are smoothed out as well.

The steep steps in the large-grain cavities are not a problem for the maximum performance. More details about the performance of cavities from large-grain material are given in Section 7.5.

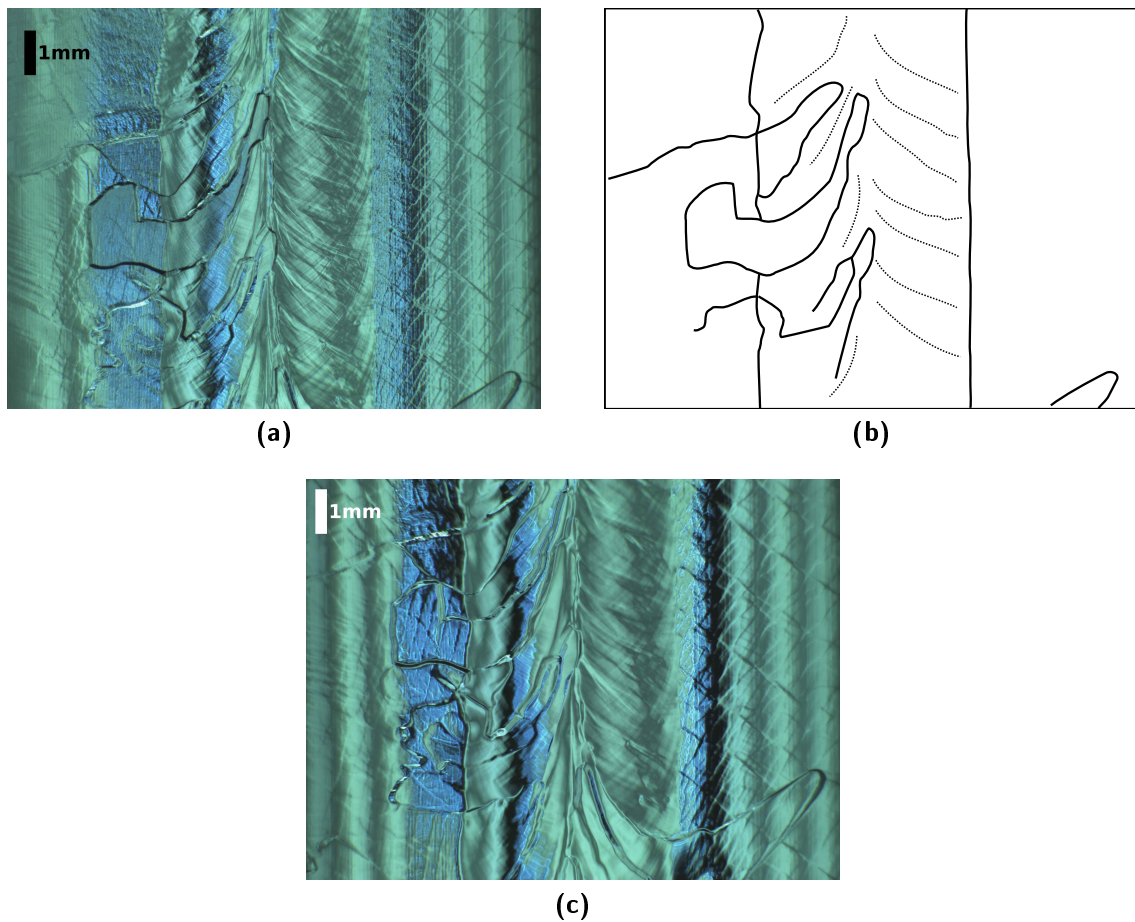


Figure 7.5: Example for pronounced grain-boundaries on the equator welding seam of a large-grain cavity. 7.5a: Image as taken by the inspection system. 7.5b: Sketch with grain-boundaries indicated as solid lines. Dotted lines are re-solidification lines. 7.5c: Image as taken by the inspection system, after EP treatment. Grain-boundaries are smoothed out

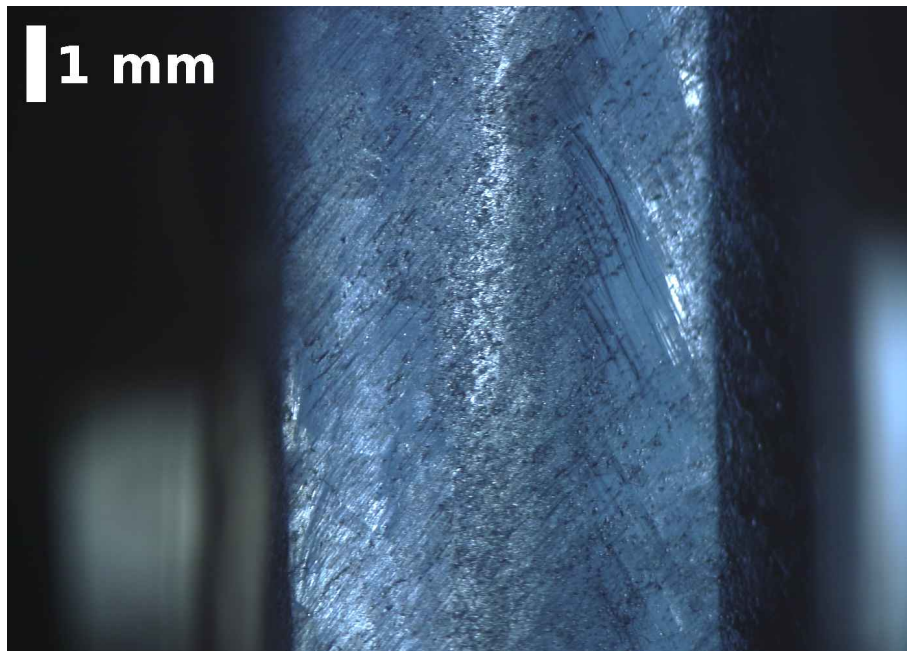


Figure 7.6: Example for ground area on iris weld

7.1.5 Grinding of welding seams

After the welding of the cavity and before chemical surface treatment it is possible to grind the surface if needed. Special conditions have to be met. The grains of the abrasive material have to be small enough so that the traces from grinding are not deeper than the thickness of material that is removed by chemical means afterwards. If that requirement is met, the ground areas will be smooth after the chemical treatment. A ground area at the iris weld before the subsequent chemical treatment is shown in Fig. 7.6. Only the small traces from the abrasive material are visible, the original structure of the iris welding seam has been removed completely.

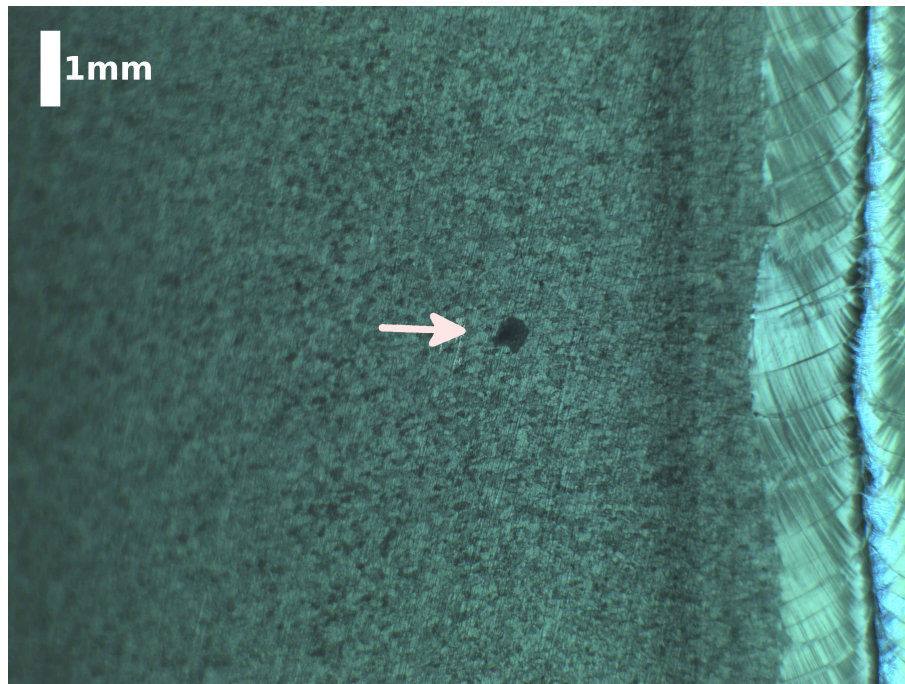


Figure 7.7: Black spot on the surface next to the welding seam

7.1.6 Spots and stains on the surface

In addition to special features in the surface topology there are also spots on the surface that are of different colour than the surrounding niobium. Most of the spots are of dark or black colour as the one in Fig. 7.7. The spot is about 3 mm left of the equatorial welding seam and has a diameter of about 400 μm . The size of such spots is typically in the range of few micrometre to more than a millimetre.

Some spots are only loosely attached to the surface and can be removed by ultra-sonic or high-pressure rinsing. Some are removed together with the surrounding niobium by BCP or EP and some are even defying chemical treatment and remain unaltered.

Three rainbow-coloured stains next to an iris weld are visible in Fig. 7.8. Observed after chemical treatment, these stains are likely to originate from the drying process of acid/water. However after a chemical treatment with proper rinsing and drying typically no stains are visible any more.

Whether such spots are a concern for cavity operation or not depends on material they consist of and at which step of the cavity preparation cycle they are observed. Drying stains at an intermediate step of the preparation have a high probability to be removed by the next chemical treatment or high pressure rinsing. Dark spots on the other hand might consist of some material that survives the subsequent processing steps (as in the example explained in detail in Chapter 7.3.2). Spots that are observed on the surface in an

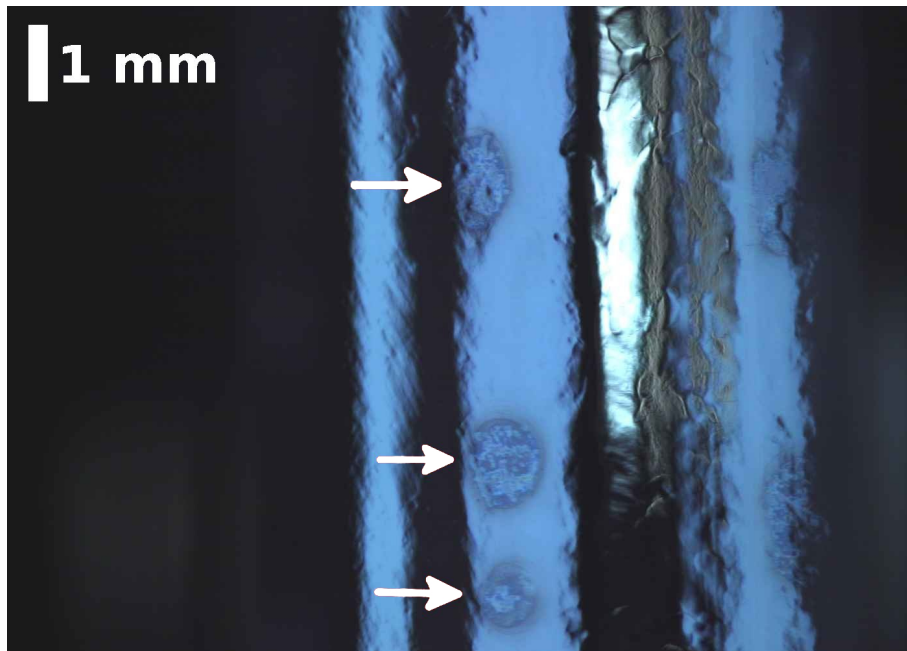


Figure 7.8: Coloured stains next to iris seam

inspection after a vertical test are always an indication that something during the surface preparation did not go as intended.

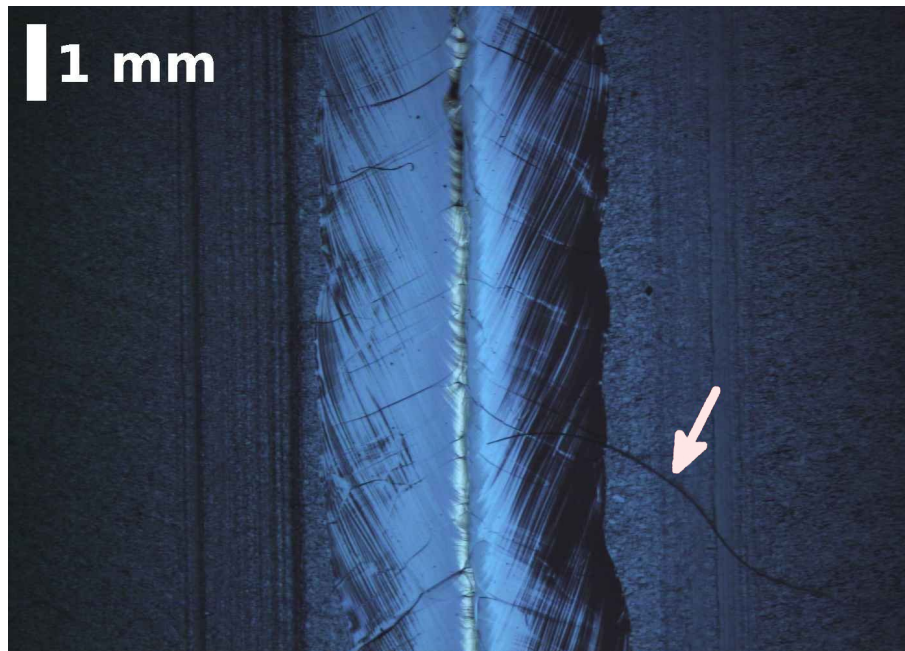


Figure 7.9: Example for dust and dirt on a cavity surface. The arrow points to a fibre across the right part of the welding seam

7.1.7 "Dirty" cavity surface

As soon as the cavity surface has been prepared for vertical testing, it is extremely clean and has to be kept in that state. After finishing the mechanical fabrication and before starting the surface preparation of the cavity, it is possible that dirt and dust enter the cavity and settle onto the surface. The same may happen if the cavity is opened outside a clean room after the initial surface preparation. In Fig. 7.9 an example of such a dirty surface is shown. In the lower right part of the image a fluff of several millimetre length is visible, lying across the welding seam. Such loose particles of dust and dirt are washed away by the cleaning procedure when the cavity is brought into the clean room or removed by chemical surface treatment and HPR at the latest.

Distinguishing dust and dirt from structures that belong to the surface is easy during optical inspection. One identifying property can be the shape (curled or wavy). An active method to identify dust and dirt is to vary the intensity of the illumination. While the reflecting niobium surface and its features change in brightness with the illumination, dust and dirt will usually stay pitch-black, not reflecting any of the light.

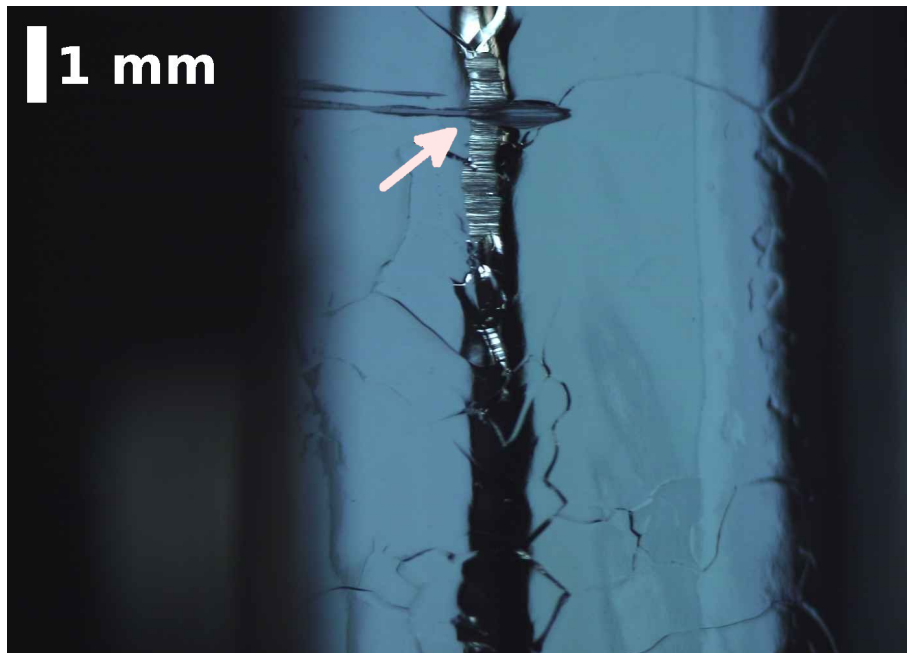


Figure 7.10: Scratch across the iris of cavity Z110

7.1.8 Scratches

Scratches are found almost exclusively at the iris. Representing the narrowest part of the cavities orifice, any tool or device that is inserted into the cavity during fabrication or surface preparation is most likely to touch an iris first. Scratches have to be avoided. They usually have sharp ridges and edges and are a deviating from the smooth round surface. Since the electric field has its largest values at the iris, the presence of scratches bears the potential risk of creating field emission (see Section 3.3.1). Such scratches are shown at the upper part of the image of Fig. 7.10. As expected the scratch is running in horizontal direction, in the direction that any tool inserted into the cavity moves. The scratch pattern consists of two parts: Many small scratches along the central ridge of the iris over a length of about 2 mm and a single narrow scratch on top of that, probably reflecting the shape of the intruding object or a multiple collision.

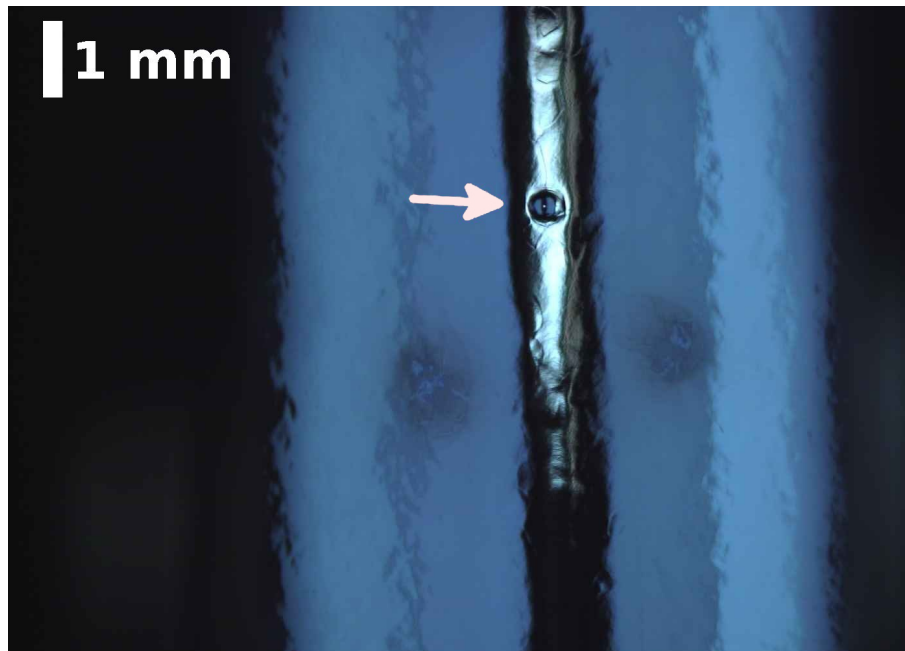


Figure 7.11: Circular pit on iris welding seam. The vertical black bar in its center motivated the name "cat-eye".

7.1.9 Pits and "Cat-Eyes"

In Fig. 7.11 a circular pit that is located exactly in the middle of the iris welding seam is shown. Its round shape and the illumination cause the appearance of a vertical black bar in its center, which motivated the name "cat-eyes". Their size may vary, but is typically between $100\ \mu\text{m}$ and $400\ \mu\text{m}$. A similar pit located at the equator is shown in Fig. 7.12. It is located directly on the border between welding seam and heat affected zone.

A second type of pits is depicted in Fig. 7.13. They are a lot smaller than the cat-eyes but also circular in shape. They may appear isolated or in groups. In this image it is a group of five and a group of three pits. But also groups of more than 15 pits have been observed. The position may be on the equator welding seam as in Fig. 7.13 or in the heat affected zone.

What all pits, cat-eyes or the smaller ones, have in common is that they only appear after a chemical treatment of the surface. This indicates a connection between the formation of pits and the chemical treatment, either due to the interplay of the niobium surface and the acid or due to the involvement of foreign material.

7 Results of cavity inspections

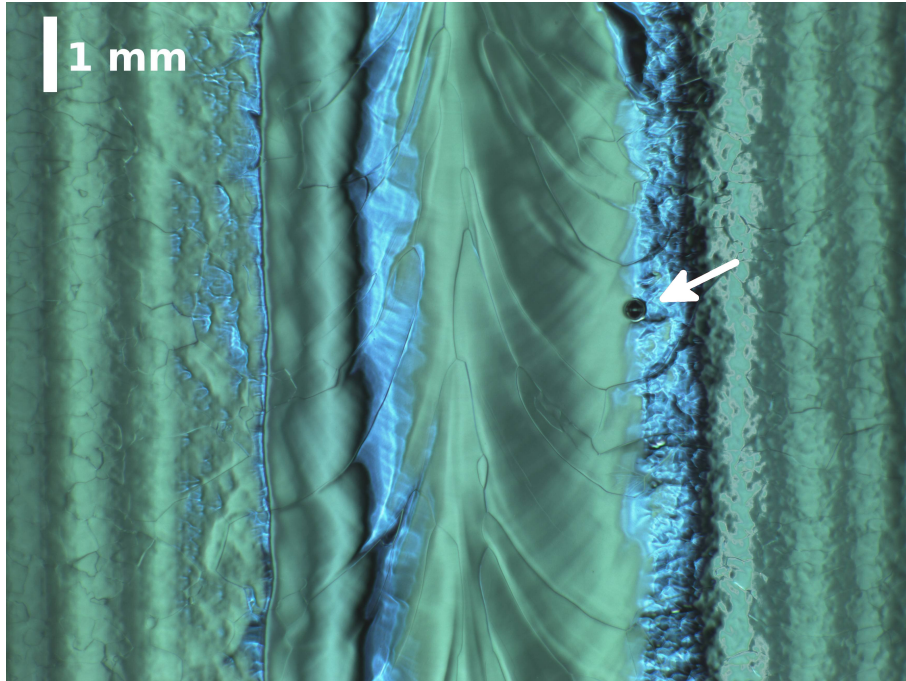


Figure 7.12: Circular pit at the equator. Note the position directly at the border between welding seam and heat affected zone.

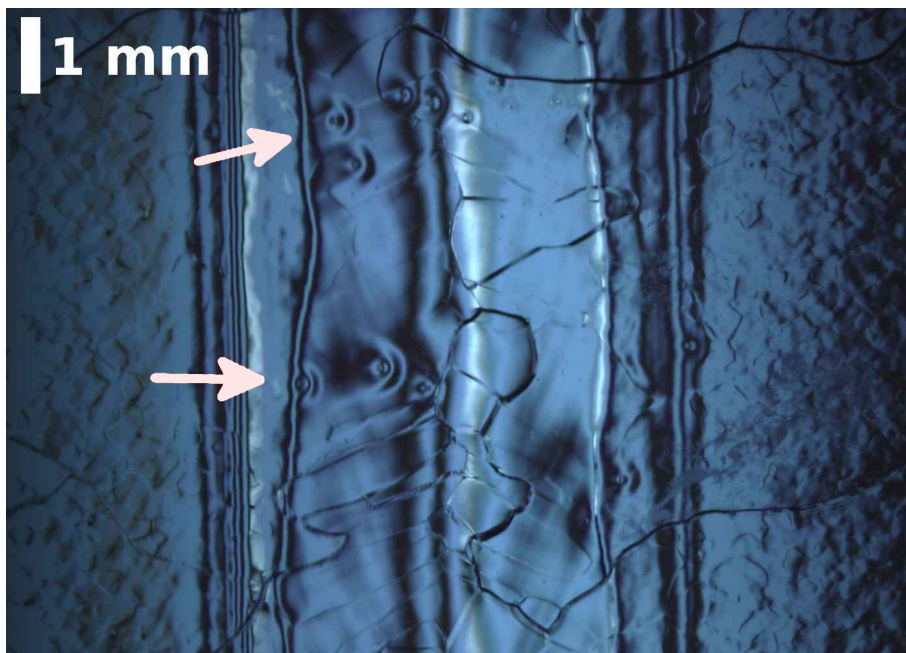


Figure 7.13: Small pits on equator welding seam

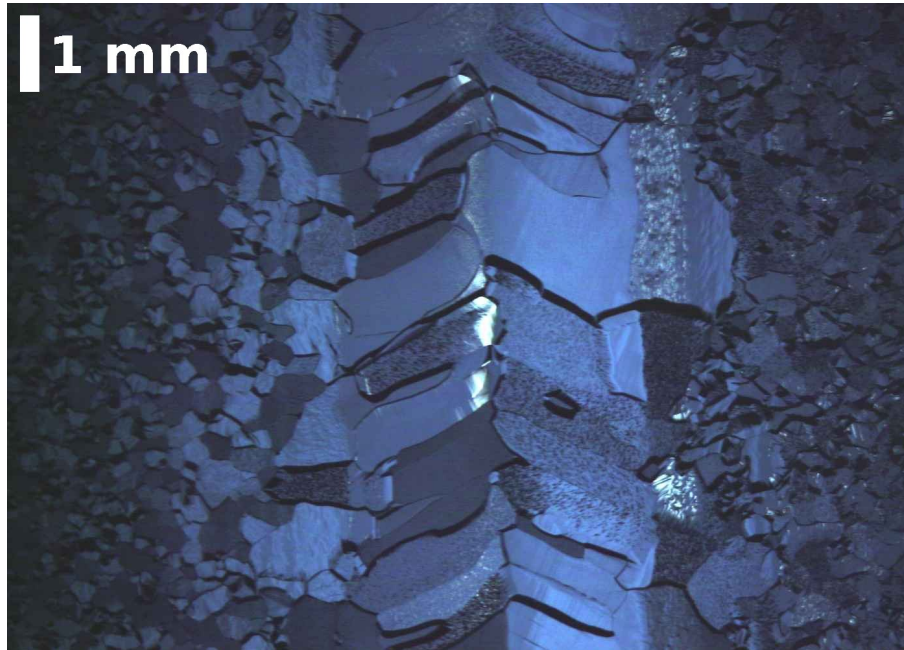


Figure 7.14: High steps between grains and rough grain surfaces in a fine-grain cavity

7.1.10 Pronounced grain-boundaries in fine grain cavities

The image of the equator welding seam in Fig. 7.14 was taken after the electro-polishing of the cavity. The surface is not smooth and shiny as one would expect. For a fine-grain material cavity the grain-boundaries on the welding seam and in the heat affected zone are extremely pronounced and form high steps. The surface is not even, there is a height-difference between neighbouring grains. Also some of the grains look extremely rough. The welding seam looked like this around the complete equator of this cell. All other eight cells looked normal.

The origin of the unusual surface structure is not known and it was a one-time observed feature. In this one case however the quench spot was located in this cell. At the quench location no particular feature, other than the generally unusual surface structure could be found.

7 Results of cavity inspections

Table 7.1: Risk assessment for optical features in pictures

Feature	Risk	
	Field emission	Quench
Non straight welding	none	none
Weld-overlap	none	none
Grinding of welding seams	none, if nothing is visible after final EP	
Spots and stains	depending on material	depending on material
"Dirty" cavity surface	high	depending on material
Scratches	high (field enhancement)	usually not
Pits and "Cat-Eyes"	if located at iris	yes
Pronounced grain boundaries	possible field enhancement	possible field enhancement

7.1.11 Risk assessment for optical features

Not all features presented in the sections before are of danger for the performance of the cavity. Table 7.1 summarises the possible risks. The risk is split into field emission and quench. Non straight welds and the weld overlap do not include a risk for the performance of the cavity, as long as the welding seam meets the specifications and is welded through. Grinding is also not a problem, if nothing remains (e.g. is visible) after the final chemical surface treatment step. Spots, stains and "dirt" or dust on the cavity surface carry a high potential for field emission when located at the iris. The risk to cause a quench is more dependant on the material. In principle it is also relevant at which step of the surface treatment process the spots, stains or dust are observed, as they may be removed by further processing. Scratches at the iris are very dangerous to create field emission when located at the iris, due to field enhancement at sharp protruding features. At the equators scratches are usually not observed. Pits and cat-eyes might also be sources for field emission if located at the iris, single pits at the equators seem not to be a problem for quench. Although large groups of pits have been observed at known quench locations. Pronounced grain boundaries are possible source for field enhancement at either iris or equator.

7.2 Linking images and cavity performance

The variety of features found in an optical inspection image of the cavity as presented in 7.1 do not necessarily imply a negative influence on the cavity RF performance. The optical properties of the surface have to be linked to the electrical properties, i.e. the rf-performance of the cavity at 2 K.

Thus the combination of optical inspection with the other diagnostic tools during vertical test such as mode measurement, Tmap and second sound measurement have to be combined and compared for agreement in the location of the quench spot and features found in optical inspection.

Optical inspection of the surface is done either before the vertical testing of the cavity or after the test. Both ways have their drawbacks. If the inspection is done before the test usually a chemical treatment of the cavity is needed in order to ensure a clean surface for the test. Thus the state of the surface is not exactly the same in optical inspection and vertical test. If special care is taken that as little dust as possible enters the cavity during inspection, an additional HPR might also be sufficient.

If the vertical test is done first, the limiting spot in the cavity (quench-location) may already be known from Tmap or a second sound measurement. Thus the respective spot on the inner surface can be inspected in great detail for possible defects or other conspicuous features. But if optical inspection is only done after the vertical test, the "history" of the surface is not known and possible evolutions of defects can not be monitored. However the inspection after the vertical test is the most important one when aiming to understand how the optical properties of the surface are connected to the rf-performance. The following section presents a couple of examples where the location of the limiting defect could be found and analysed in detail.

7.3 Analysis of individual cavities

In order to allow a detailed study of the defect area, the three following cavities have been dissected. Round samples with a diameter of 4 cm have been cut with the defect in their center. The size of the samples made it possible to investigate the defects by means of profilometry, optical microscopy and scanning electron microscopy (SEM) including element analysis like energy-dispersive electron spectroscopy (EDX) and Auger spectroscopy.

7.3.1 AC126

In the vertical test no. 5 AC126 was limited at 20.4 MV/m. Tmap and second sound measurement consistently identified the quench location in cell 2 next to the equator near 85° (see Fig. 7.15a). Optical inspection of the cavity subsequent to the vertical test revealed an almost circular, rainbow coloured stain with a diameter of 4 mm (see Fig. 7.15b). Three more stains were found in cell 2 and four in cell 3. They are spaced exactly 90° from

7 Results of cavity inspections

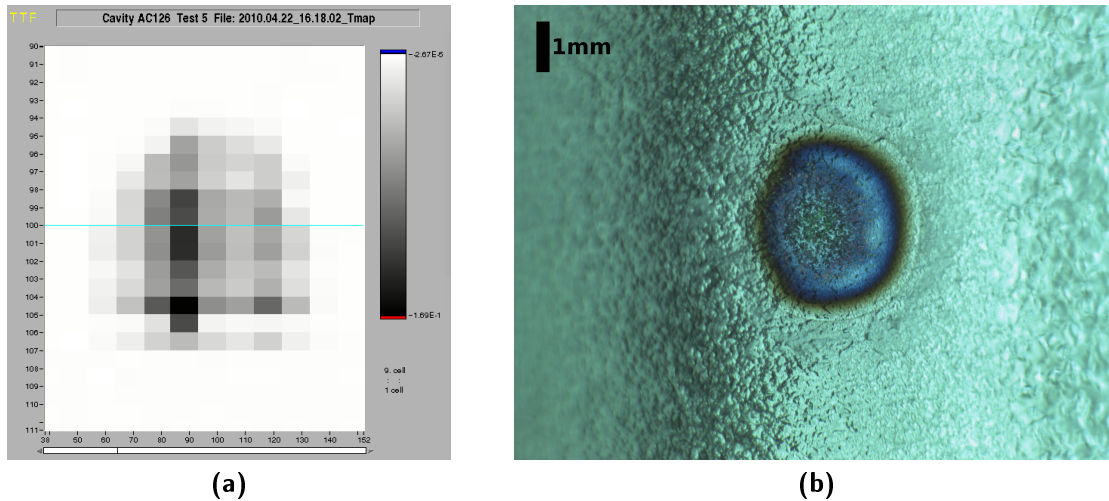
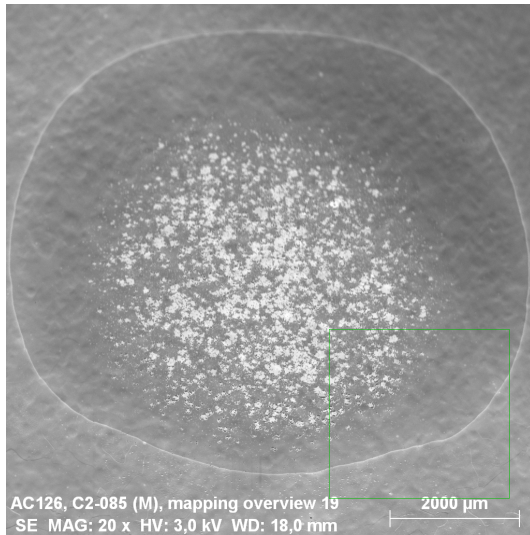


Figure 7.15: 7.15a: Hotspot located by Tmap in cell 2 at 85 degrees near equator of AC126, 7.15b:Optical inspection image of the respective location

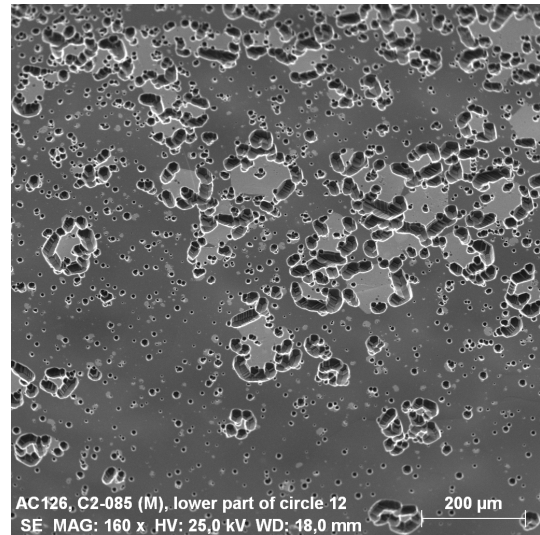
each other; the pattern in cell 2 rotated 45° with respect to the one in cell 3. This matches exactly the layout of the nozzles in the HPR system and it is assumed that the stains have been produced by an incident where the motors that move the cavity with respect to the nozzles stopped and the water jets hit the surface for a longer time than usual. A reason why the motors could have stopped could not be found retrospectively.

SEM images of the sample cut from AC126 are shown in Fig. 7.16. Figure 7.16a shows the full circle that is visible in the optical inspection image. What looks like white spots in the SEM image are in fact round areas that are surrounded by small crystals (Fig. 7.16b, Fig. 7.16c and Fig. 7.16d) that have grown on the surface. The rainbow coloured fringes of the the spot suggest oxidation of the niobium on the surface by the impinging water jet. A line scan with the EDX across the boundary of the circle confirms this speculation. As visible in Fig. 7.17 the abundance of oxygen is higher in the inner part of the circle and dropping towards the boundary, then remains constant.

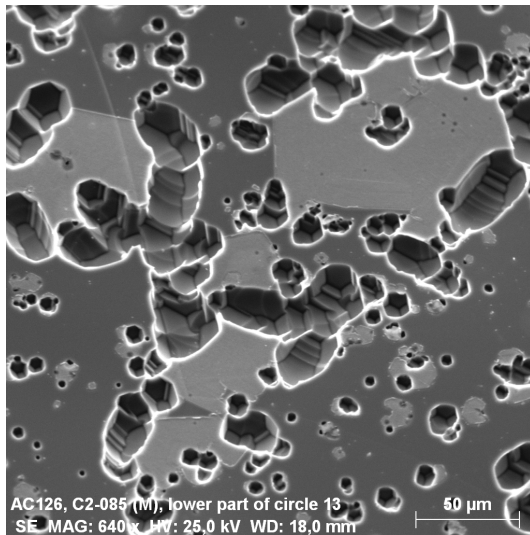
The thickness of the oxide layer was measured by Auger spectroscopy for one of the samples [87]. On one of the inner rings the oxide layer was found to be 195 nm and on one of the outer rings 32.5 nm, while the oxide layer outside the rings only is 13 nm thick.



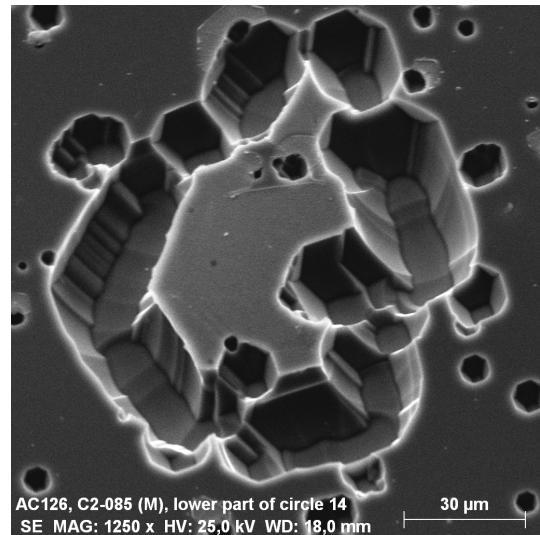
(a)



(b)



(c)



(d)

Figure 7.16: 7.16a: SEM image of the defect at the quench location in AC126, 7.16b, 7.16c and 7.16d: Detailed view with increased magnification of the crystal structures grown on the surface

7 Results of cavity inspections

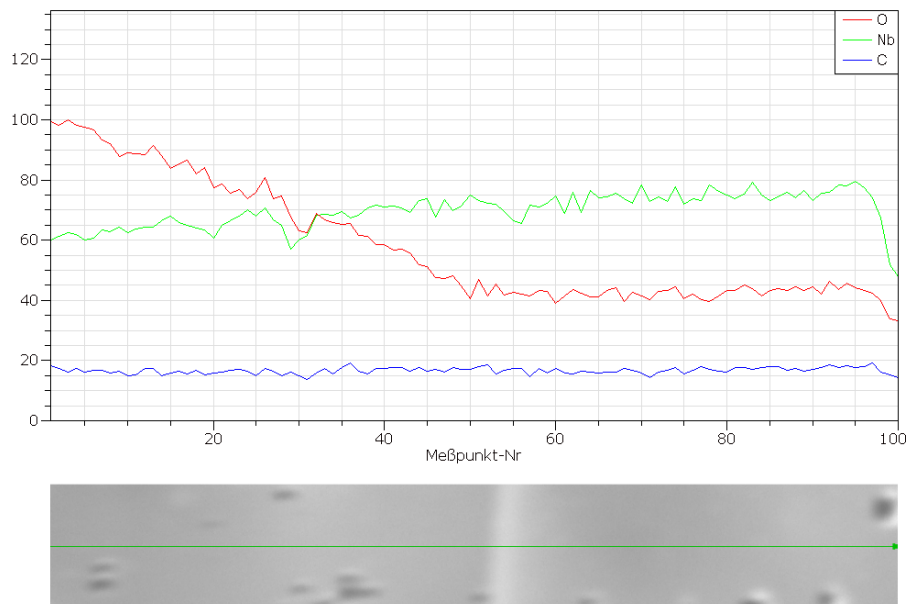


Figure 7.17: Element abundance for oxygen, niobium and carbon along a line from inside (left) to outside the circle (right) in AC126

7.3.2 Z161

In the optical inspection of Z161 following the welding, before the first chemical treatment of the surface, dark spots were found close to the equator welding seams in several cells. An additional cleaning step in the ultrasonic (US) bath was performed but only reduced the number of spots by roughly a factor of 2. It was decided to go on with the standard cavity preparation process anyhow. After the bulk surface removal of $112\ \mu\text{m}$ by EP some of the spots were still present. The removal of the spots on the surface is summarised in Figure 7.18. For each cell the angular position of a black spot is marked. The initial state of the surface is depicted in Figure 7.18a. After the US rinsing the number of spots, especially in cells 8 and 9 decreases (see Fig. 7.18b). The bulk- and final EP reduced the number of spots further (Fig. 7.18c and Fig. 7.18d). Now there is a distinction between spots that are clearly visible and spots that are only barely visible and only have been noticed, because their location was already known from the previous inspections. The complete list of spots is given in Table B.1 and Table B.2.

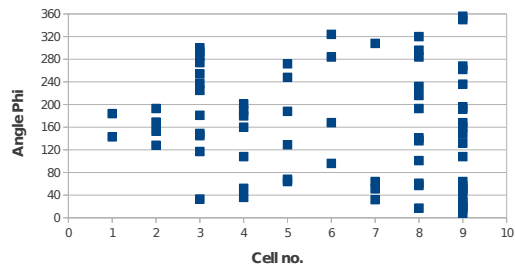
Some spots have not been affected by the EP at all. As can be seen in Fig. 7.19 the surface structure has not been altered and is still the same as before the EP. In addition, the spots are now protruding from the surface as plateaus. Their height is about the same amount as the surrounding material that has been removed.

The vertical test of Z161 was carried out with Tmap and 2nd sound measurement, since a low accelerating gradient and quench at one of the suspicious spots was expected. Indeed one of the defects was confirmed as the origin of the quench (see Fig. 7.20). As expected the cavity was limited at a low gradient of $13.4\ \text{MV/m}$ with $Q_0 = 1.4 \times 10^{10}$.

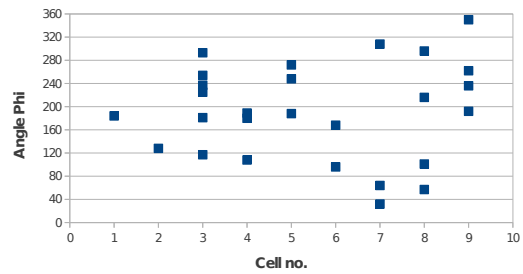
Cavity Z161 was a very good candidate for dissection because the defects were spotted very early, which means that they could be closely monitored through all preparation steps and their origin has to be related to the fabrication itself and not the surface preparation process afterwards. In addition the cavity was limited at a very low gradient in the vertical test ($13.4\ \text{MV/m}$) and several of the observed defects were identified as the quench locations by Tmap and second sound in different modes. All quench locations and several other interesting structures have been extracted from the cavity.

Sample A was cut from cell no. 2 at 128° , the location of the quench in the π -mode (and $\frac{8\pi}{9}$ -, $\frac{4\pi}{9}$ -, $\frac{3\pi}{9}$ - and $\frac{2\pi}{9}$ -mode). The SEM image of the defect is shown in Fig. 7.21a. The defect is clearly protruding from the surrounding material. Figure 7.21b shows a close-up view of the plateau in the centre. The height of the plateau with respect to the level of the surrounding area corresponds to the amount of material that has been removed by EP in total. Small crystals that are sitting on the plateau can be seen in Fig. 7.21b. The EDX analysis of the plateau area of the defect showed a very high content of aluminium. The hypothesis is that during the preparation for electron beam welding aluminium swarfs have been produced and got into the cavity. Particles sitting in the heat affected zone were melted and formed a thin layer of aluminium on the niobium surface. Since aluminium is not removed by the EP process, it protects material below the film from removal as well

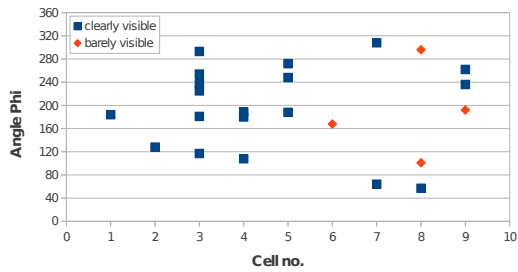
7 Results of cavity inspections



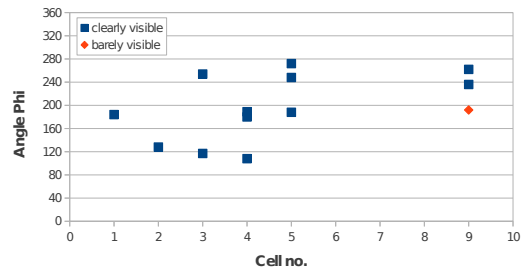
(a) Initial state



(b) After US rinsing



(c) After Bulk-EP



(d) After final EP

Figure 7.18: Black spots on the surface of Z161: (a) Initial state of the surface after fabrication (b) Reduced number of black spots after US rinsing (c) After bulk-EP: Some spots are clearly visible and some have been almost removed and are barely visible (d) After final EP most spots have been removed

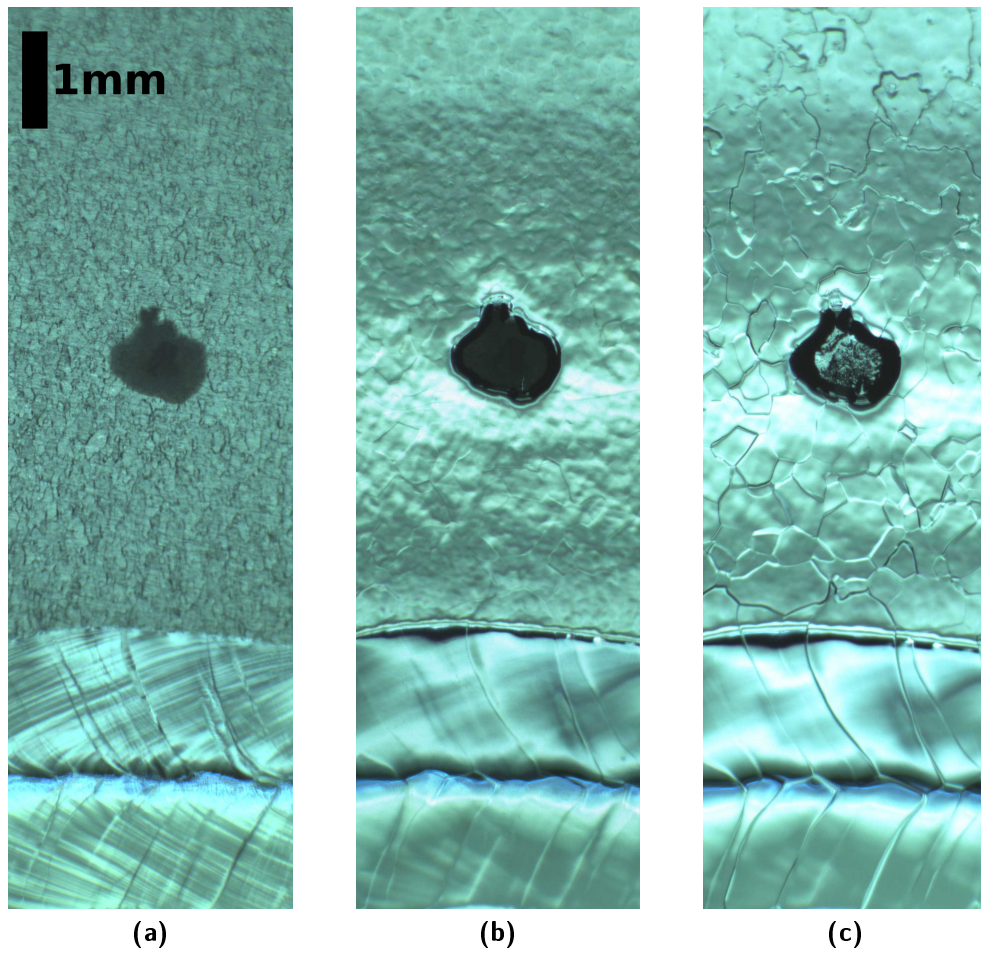


Figure 7.19: Evolution of a defect in Z161: (a) Spot before surface treatment, (b) after initial EP, (c) after final EP and vertical Test. The defect has hardly been affected by the EP process.

7 Results of cavity inspections

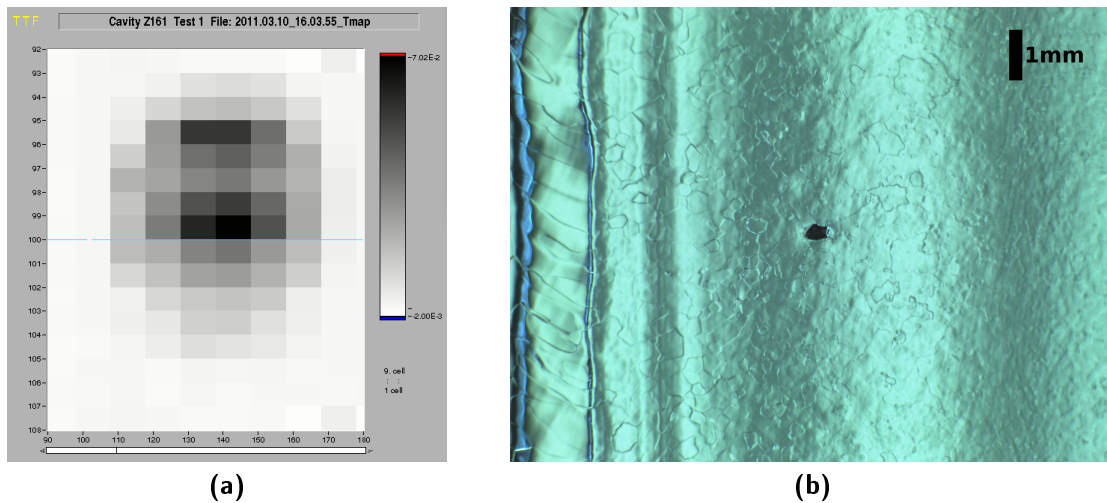


Figure 7.20: 7.20a: Hotspot located by Tmap in cell 2 at 128 degrees near equator of Z161, 7.20b: Optical inspection image of the respective location

and a plateau is created. The source of the aluminium particles is thought to be identified and eliminated.

This defect can be compared with the simple model for thermal breakdown in Section 3.3.2.

The defect is not circular as in the model, but an equivalent circle with equal area can be derived. Assuming an elliptical shape with a major axis of $430\ \mu\text{m}$ and a minor axis of $340\ \mu\text{m}$, the equivalent circle has a radius $a = 191\ \mu\text{m}$. The surface resistance R_s has to be derived from the electrical resistivity of aluminium. A comprehensive review of the resistivity of aluminium can be found in [88]. The quoted value for the resistivity of very high purity aluminium at 2 K is too low and would result in unrealistic high quench fields. Since the aluminium contamination is assumed to be originating from the fabrication process, it is most probably not high purity aluminium, but an alloy. Thus the resistivity is expected to be higher. Extrapolating from the low-purity part of the collection of resistivities in [88] a resistivity in the range of $1 \times 10^{-9}\ \Omega\text{m}$ to $1 \times 10^{-8}\ \Omega\text{m}$ is plausible. Considering the skin effect at 1.3 GHz that results in a surface resistance $R_s = 2\ \text{m}\Omega$ to $7\ \text{m}\Omega$. This is also comparable to the value of $R_s = 10\ \text{m}\Omega$ that is given in [38] for defects of normal conducting niobium. With the defect size $a = 191\ \mu\text{m}$ and the surface resistance $R_s = 2\ \text{m}\Omega$ to $7\ \text{m}\Omega$ Eqn. (3.12) evaluates to $H_{max} = 500\ \text{Oe}$ to $890\ \text{Oe}$, corresponding to an accelerating gradient of $E_{acc} = 11.72\ \text{MV/m}$ to $20.8\ \text{MV/m}$. This is in good agreement with the actual quench at $E_{acc} = 13.4\ \text{MV/m}$

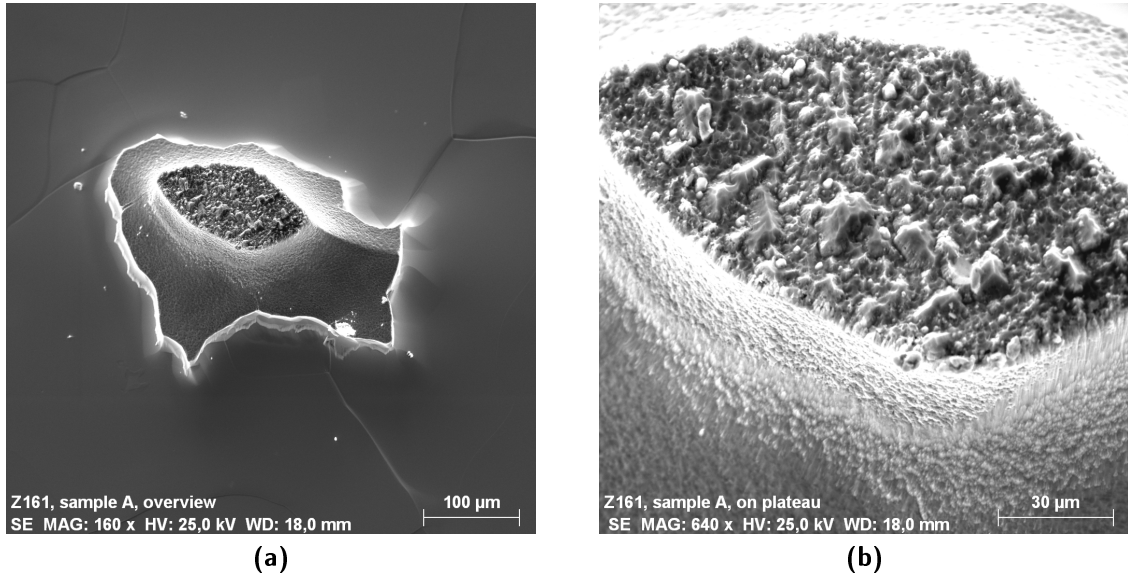


Figure 7.21: SEM image of the defect at the quench location in Z161 7.21a: Overview of the defect 7.21b: Close-up of the structures on the defect plateau

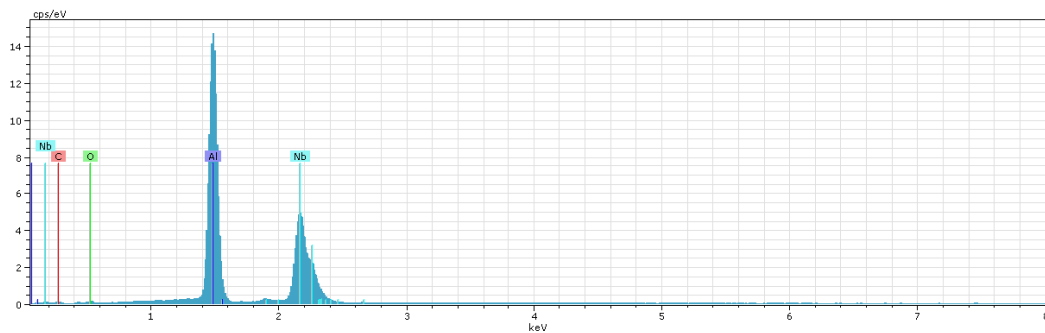


Figure 7.22: EDX spectrum of the defect on the quench location extracted from Z161. Besides the expected niobium (Nb) and minimal traces of oxygen (O) and carbon (C) a strong signal of aluminium (Al) is present.

7.3.3 Z130

The cavity Z130 was limited at 17.3 MV/m in the π -mode in the vertical test no. 1. For the second vertical test, the Tmap system was added for localisation of the quench location. The π -mode in the second test was limited by quench at 16.6 MV/m. The hotspot was located in cell no. 1 around 345° . The optical inspection that was carried out after the vertical test did not show any suspicious features in the respective area on the inner cavity surface.

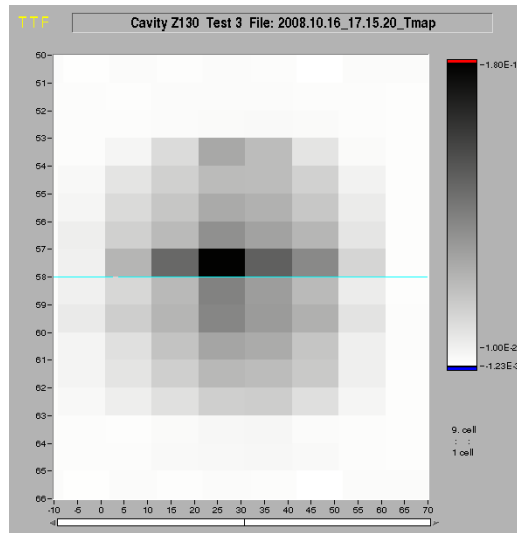
Another hotspot was found in cell no. 5 around 25° for the $\frac{3\pi}{9}$ - and $\frac{1\pi}{9}$ -mode. The quench occurred at a gradient of 22 MV/m. The temperature map with the hot spot for the $\frac{3\pi}{9}$ -mode is shown in Figure 7.23a. The optical inspection of this location revealed a defect on the equator welding seam. The optical inspection image is shown in Figure 7.23b. The defect is located on the left edge of the equatorial welding seam. It is of more or less round shape with a diameter of about 700 μm . The size of this defect does not fit the expectations for the size of a quenching defect in Chapter 3.3.2.

The area with the identified quench location in cell no. 5 has been extracted from the cavity for detailed investigation. Element analysis showed no inclusions of foreign material [89]. The result of a measurement with a profilometre is shown in Figure 7.24. The maximum difference in height in the profile is 265 μm .

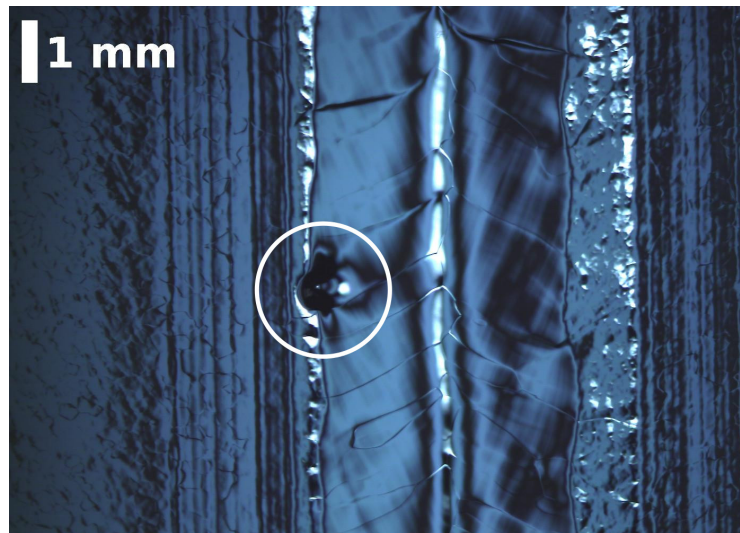
An image taken by SEM is shown in Figure 7.25. It depicts the left part of the round defect. The edge of the circular defect is a sharp step. Small substructures on the order of few micrometres are present. This substructure is better suited to fit the expectations for a relation between defect size and quenching gradient and makes clear that it is important not only to consider the macroscopic, optically visible structure, but also the microscopic substructure. More on defect sizes is given in Section 7.4.

7.3.4 AC151

The large-grain cavity AC151 reached 26.7 MV/m in test no. 2 after BCP-treatment and additional HPR-cycles that were performed to remedy the field emission present in the first test. The next surface treatment was a removal of 48 μm by EP. The limitation in test no. 3 were Q-switches (see Section 3.3.4) around 18 MV/m to 20 MV/m. Mode-measurements indicated the origin of the Q-switch in one of the end-cells, so the next test was done with a "Quick-Tmap " on one end-cell and temperature sensors attached to the HOM couplers. The Q-switch now occurred at 16.7 MV/m (see Fig. 7.26) and strong heating of up to 14 K was observed at the base of HOM coupler 2 at the long-endgroup side. In the optical inspection subsequent to the vertical test the tip of the antenna of HOM coupler 2 was found damaged. Instead of smooth and shiny as usual the antenna



(a)



(b)

Figure 7.23: 7.23a: Hotspot located by Tmap in cell 5 around 25 degrees near equator of Z130, 7.23b:Optical inspection image of the respective location. A circular defect is visible on the left edge of the welding seam.

7 Results of cavity inspections

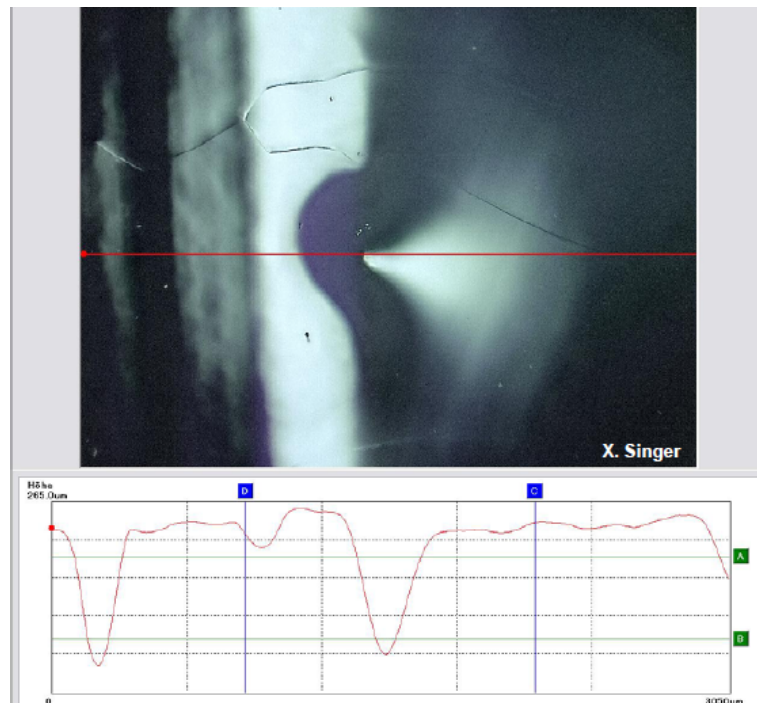


Figure 7.24: Profile of the defect in Z130. The maximum difference in height is 265 μm . [89]

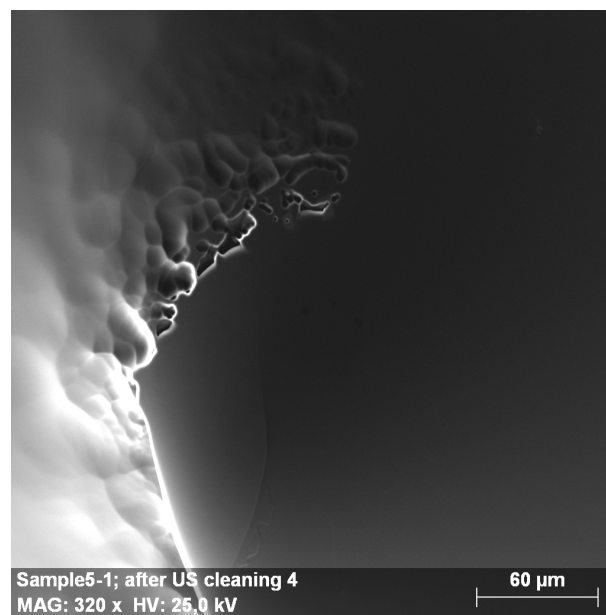


Figure 7.25: SEM image of the left edge of the round defect extracted from Z130. Small substructures on the order of few micrometers and sharp edges are visible.

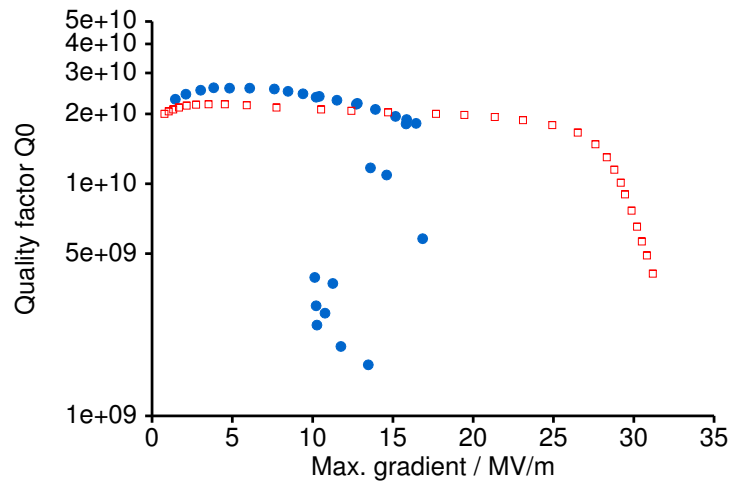
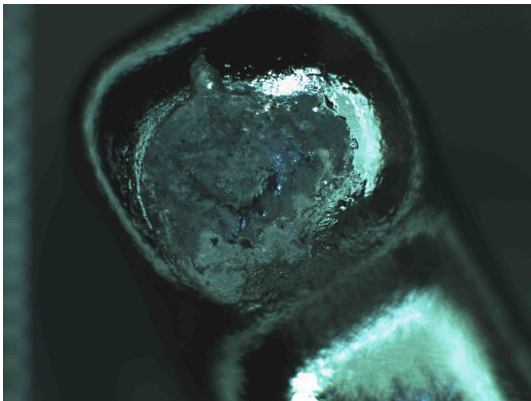


Figure 7.26: Q(E)-curve of AC151 in test no. 4 with Q-switches starting at a gradient of 16.7 MV/m (blue circles) and Q(E)-curve in test no. 5 after the successful repair (red squares)



(a)



(b)

Figure 7.27: 7.27a: Optical inspection image of the damaged antenna tip at HOM 2 in AC151. An undamaged tip is smooth and shiny. 7.27b: Damaged HOM antenna seen from outside the cavity

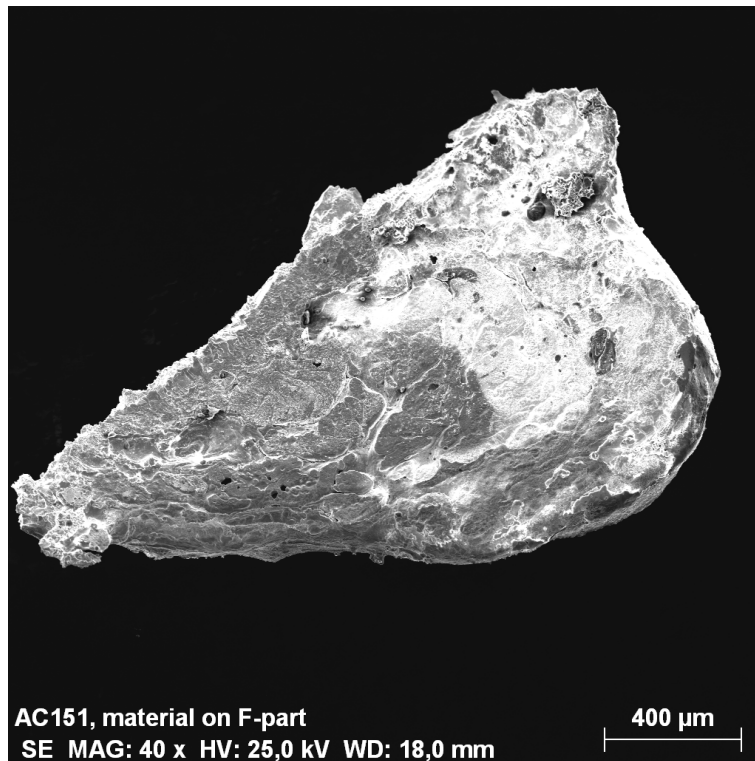


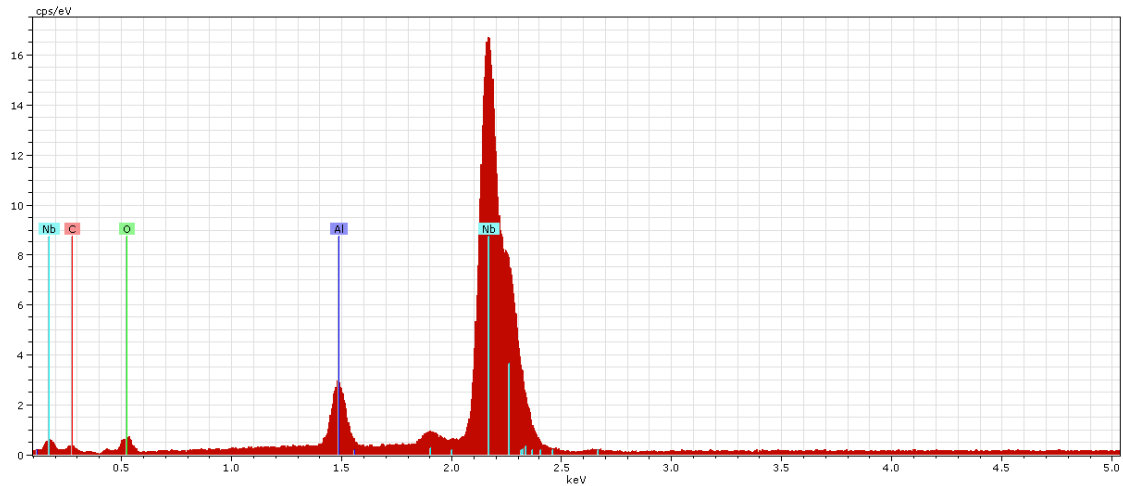
Figure 7.28: SEM picture of the sample extracted from the HOM antenna in AC151

was rough and dull (Fig. 7.27a). Looked at from the side the round shape of the tip had been flattened (Fig. 7.27b).

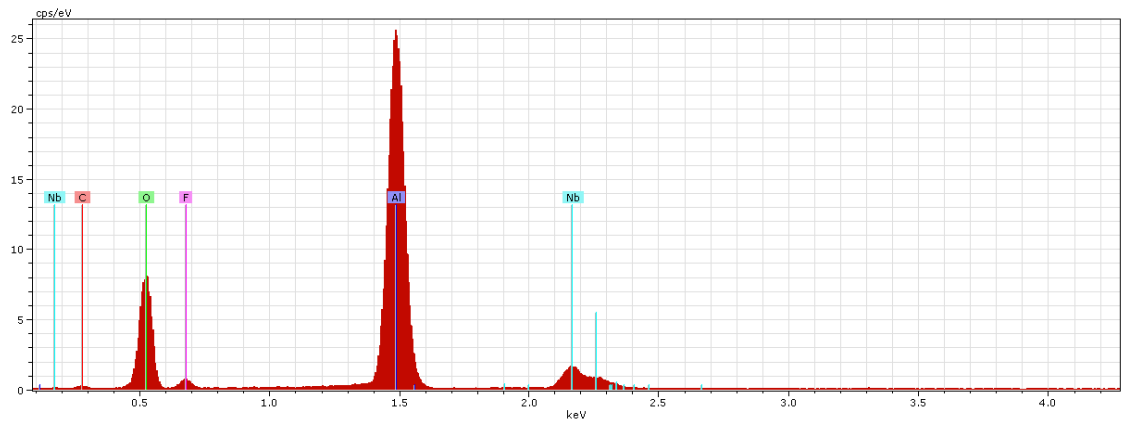
A small sample of material was taken from the damaged location for analysis for foreign material. An SEM picture of the extracted sample is shown in Figure 7.28. After the extraction of the sample the antenna was ground to restore the original round form and remove any foreign material. In addition a short local etching was applied after the grinding and the whole cavity was treated with another 12 μm EP.

The cathode of the EP system that was used in the surface-treatment of AC151 was inspected as well. The Teflon wrapping was damaged and there were scratches on the aluminium at a location corresponding to the position of the HOM coupler. An element analysis of the material sample taken from the damaged location is shown in Fig. 7.29. High content of aluminium is visible in the spectra as well as traces of fluorine originating from the Teflon wrapping (Fig. 7.29b).

Foreign, non-superconducting material on the tip of the HOM coupler explains the Q-switch behaviour that was observed. The aluminium heats up in the RF field and as the surrounding niobium is not able to transport away the excessive heat with increasing field gradient, parts of the niobium become normal-conducting as well. That transition is visible as the sudden drop in Q in the Q(E)-curve.



(a)



(b)

Figure 7.29: EDX-spectra of two different spots on the sample extracted from the HOM antenna in AC151: (a) Mostly niobium with increased aluminium content (b) Extreme high aluminium content with oxygen and niobium. Some fluorine from the Teflon wrapping of the EP cathode is visible as well.

7 Results of cavity inspections

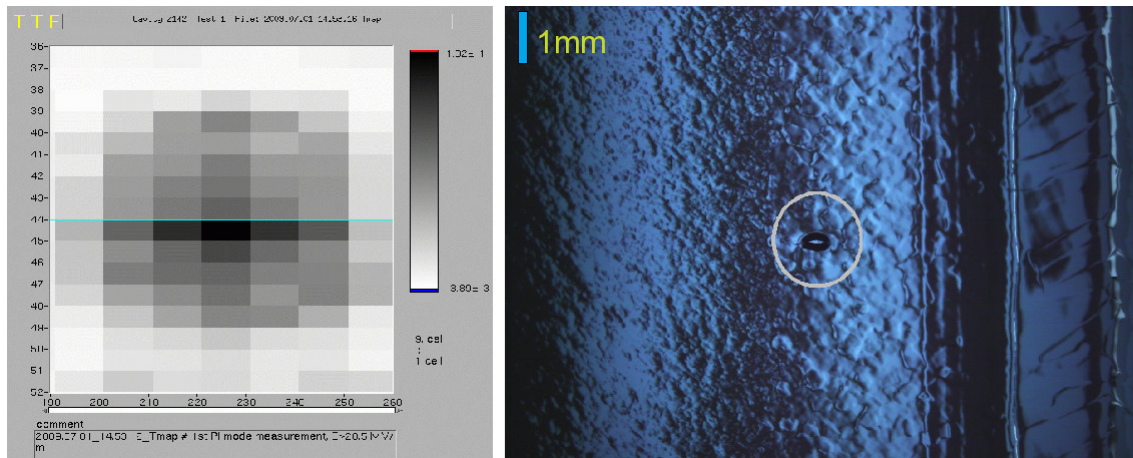


Figure 7.30: Limiting defect in cavity Z142: Hotspot located by Tmap in cell 6 during quench at 20 MV/m and picture of the respective area in the cavity with defect

7.3.5 Z142

Cavity Z142 was limited at $E_{acc} = 20$ MV/m in the π -mode. In Figure 7.30 the corresponding temperature map is shown on the left side. A hotspot was found in cell 6 close to the equator. The right part of Figure 7.30 shows the picture of the respective area on the inner surface of the cavity. At the quench location there is a defect of elliptical shape with a major axis of $540 \mu\text{m}$ and a minor axis of $360 \mu\text{m}$. It is a hole in the surface and in the middle a straight line of reflections is visible.

The defect at the quench location had already been observed earlier. The evolution of this defect is shown in Figure 7.31. After the bulk EP the defect already had the same shape and size as after the final EP and test. Only the reflection in the center is missing. Looking at the pictures of the inspection before the surface treatment and with the knowledge of where to look, a hint of the defect is visible as well. Although, it is not yet a pit. Only a straight line in the middle is visible. The fact, that the defect is already visible before any surface treatment indicates that the defect originates from the manufacturing process itself. Either it was a cavern in the surface that has been uncovered by the removal of the overlying surface or it was foreign material, that has been removed by EP a lot faster than the surrounding niobium.

7.3.6 AC71

An example for the successful improvement of a cavity by the removal of a defect is cavity AC71. The optical inspection of AC71 was performed at KEK. A scratch was found at the iris between cells 1 and 2 and it was decided to use the opportunity for grinding that scratch at KEK as well. Before and after the grinding the scratch-location was sponge-

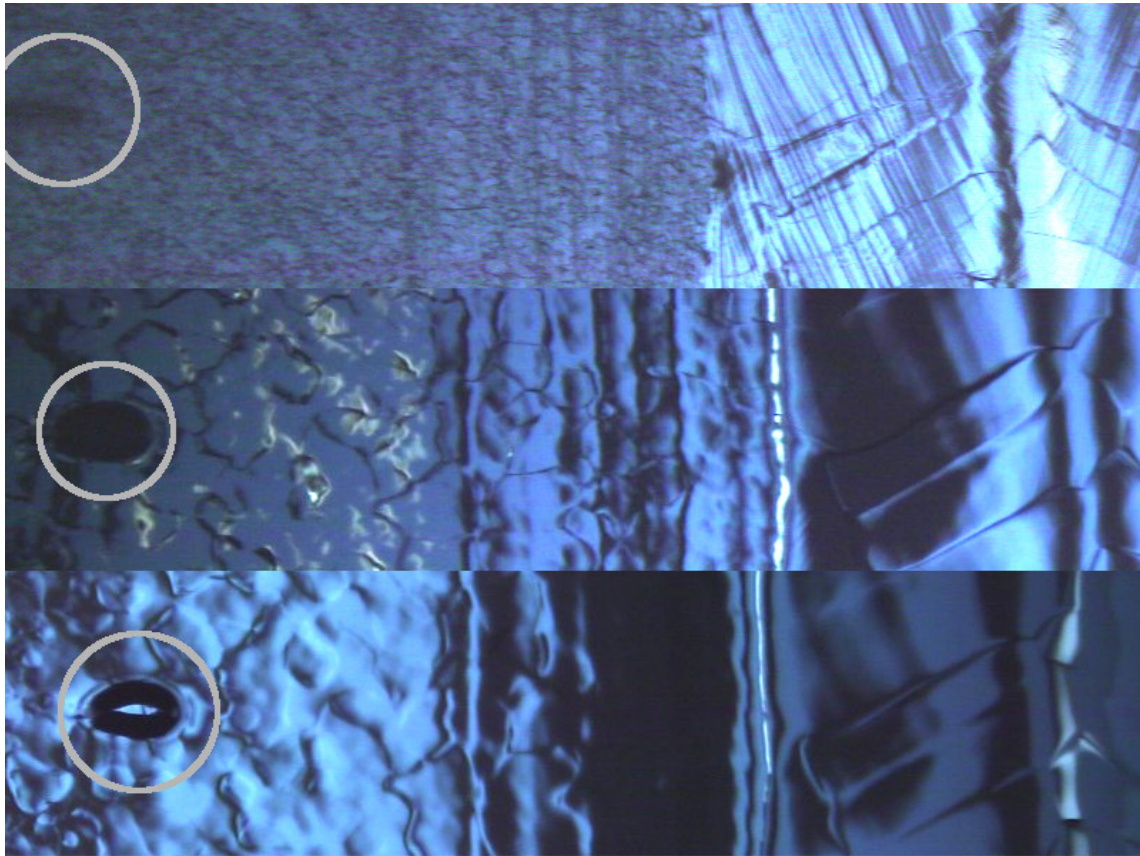


Figure 7.31: Comparison of the same defect in Z142 at three different surface preparation stages: Before surface treatment (upper part), after bulk EP (middle part) and after final EP (lower part)

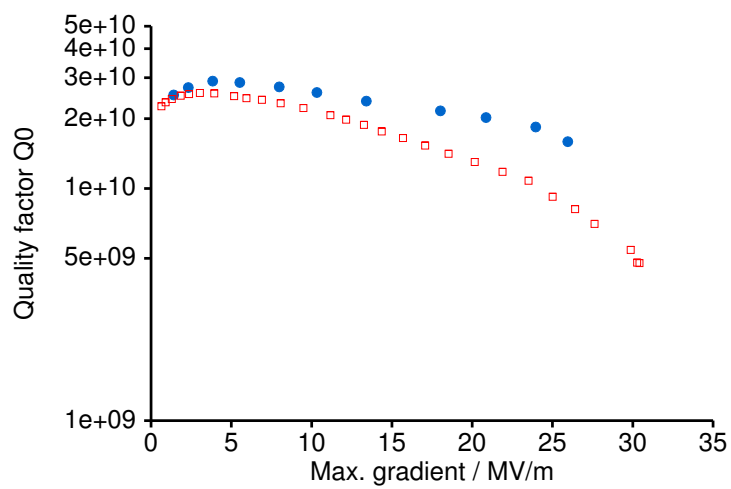


Figure 7.32: Q(E)-performance of AC71, before (blue circles) and after (red squares) grinding of a scratch on the iris between cells 1 and 2

7 Results of cavity inspections

wiped with ethanol. After the grinding of the scratch 30 μm EP followed by an ultra-sonic rinse with ultra-pure water and a HPR were carried out at KEK as well. The improvement in Q(E)-performance is shown in figure 7.32. Before the grinding the cavity was limited at 26.0 MV/m. In the vertical test after being sent back to DESY, AC71 reached 30.4 MV/m. This is an example for the effectiveness of the combination of optical inspection and local guided repair methods.

Table 7.2: Selection of defects for analysis of dependency between defect size and limiting gradient. The area is given for the size as some defects are almost circular and others elliptical. All defects have been identified as quench spots by Tmap or second sound measurement

Cavity	Cell	Angle	Defect size (area)	Test No.	Acc. gradient
Z161	3	117°	0.16 mm ²	1	21 MV/m
Z161	5	272°	0.80 mm ²	1	22 MV/m
Z161	2	128°	0.12 mm ²	1	14 MV/m
Z142	6	211°	0.15 mm ²	1	20 MV/m
AC120	5	132°	0.05 mm ²	3	33 MV/m
Z130	5	18°	0.35 mm ²	3	22 MV/m
Z131	1	36°	0.05 mm ²	3	18 MV/m

7.4 Defect size and quench field

Starting from calculation for the breakdown field of a defect with a thermal model as in Section 3.3.2 one expects higher breakdown fields for smaller defects and vice versa. A collection of defects for analysis of the interdependency of defect size and quenching gradient are summarized in Table 7.2. Only defects that have been confirmed as quench location by second sound or Tmap have been taken into account. Since some defects are circular and others are highly elliptical, the area of the defect is given as a measure for the size. Where multiple defects are given for one cavity a full mode-measurement was carried out and the cavity quenched at different locations. The given accelerating gradient is the field in the respective cell.

The data from Table 7.2 is plotted in Figure 7.33. From the simple thermal model smaller defect size would be expected for higher gradients. It seems that there is no direct relation between the defect size and the gradient at which the defect quenches in this data sample. In a similar analysis at KEK the result looks different [90]. The correlation between quench field and the profile of the problematic defect is shown in Fig. 7.34. Here smaller defect sizes are observed for higher quench fields.

7 Results of cavity inspections

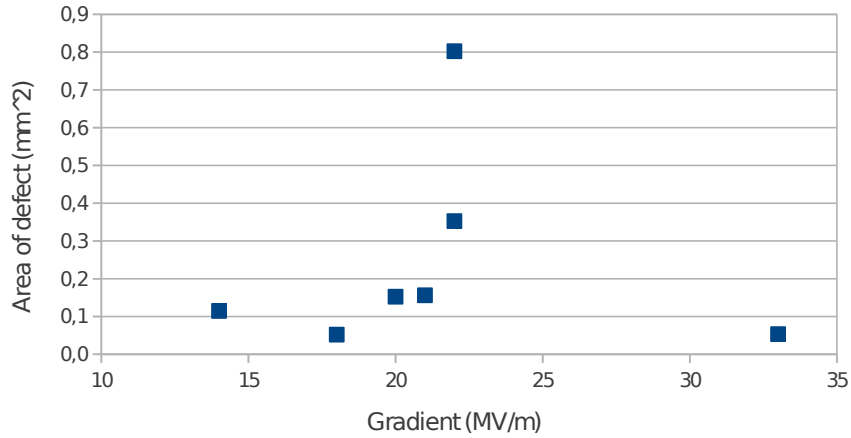


Figure 7.33: Dependency between the defect size (geometric area) and the gradient at which it quenched for cavities processed and measured at DESY

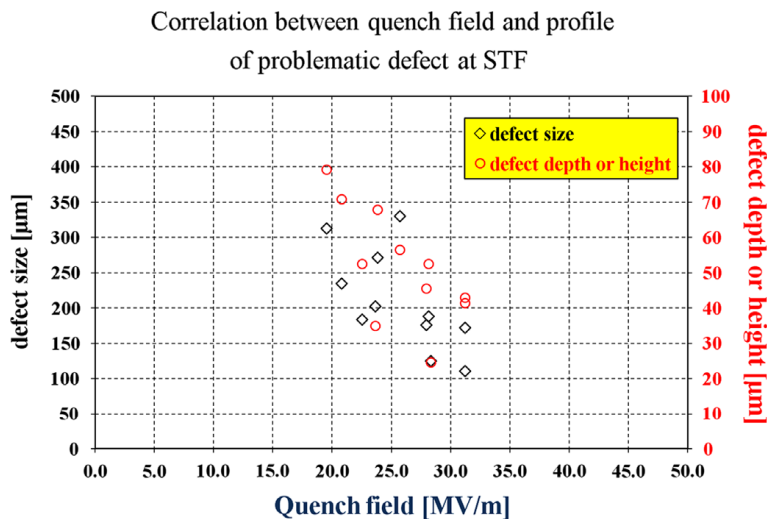


Figure 7.34: Dependency between the defect size (diameter) and defect height or depth and the gradient at which it quenched for cavities processed and measured at KEK [90]

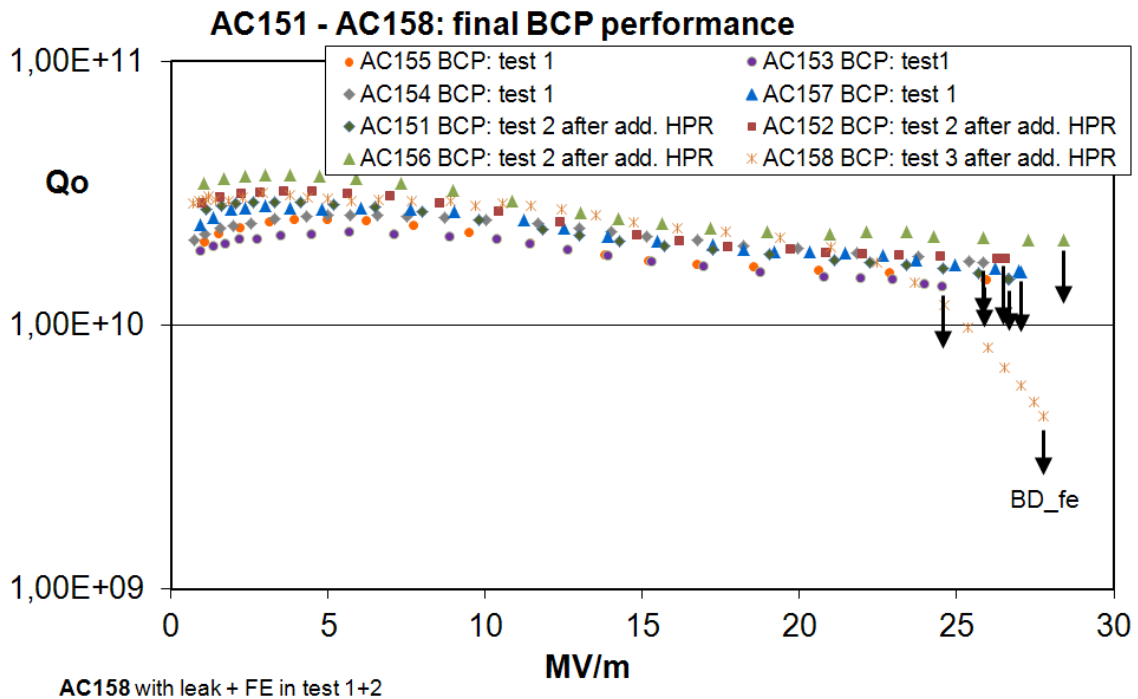


Figure 7.35: Q(E) results of large grain cavities after BCP treatment [4]

7.5 Large Grain Cavities

The preparation and testing of the batch of eight large grain cavities AC151-AC158 has been closely followed by optical inspection. All of them have been inspected upon arrival from the manufacturer with an untreated surface. The next inspections followed after the main surface removal of about 100 μm by BCP. After that inspection the final BCP treatment of 20 μm to 30 μm was performed, followed by the vertical test for all cavities. The Q(E)-results of the cavities in the vertical test is shown in Fig. 7.35. The maximum accelerating gradient of the cavities is in the range of 24.5 MV/m to 28.5 MV/m. For three out of the eight cavities (AC151, AC156 and AC157) optical inspection was done directly following the vertical test. For the other five cavities the next optical inspection was done at an intermediate step of the subsequent EP treatment.

The Q(E)-performance after EP treatment is shown in Fig. 7.36 for five cavities. The maximum accelerating gradient is now in the range of 31 MV/m to 45.5 MV/m. All cavities have improved in performance.

The optical inspections of the cavities revealed no obvious defects in the surface in the surrounding area of quenches that have been located by either Tmap or second sound measurement. The only features that can be seen on the generally very smooth surface of the large grain material are small etching pits and grain boundaries. The small etching

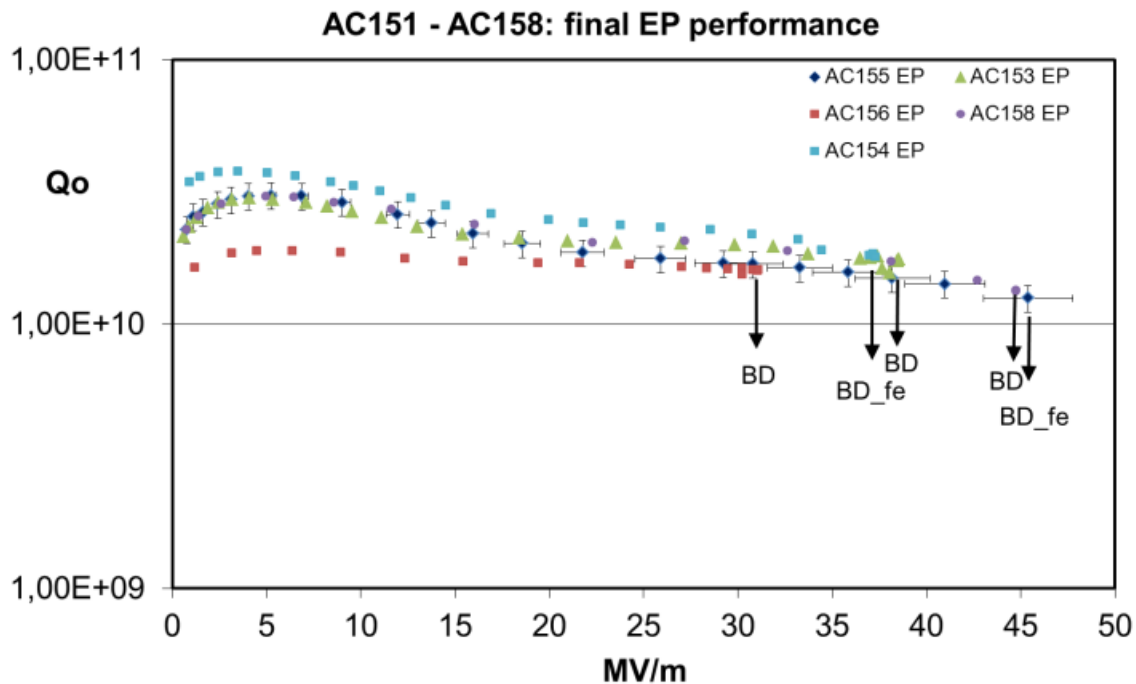


Figure 7.36: $Q(E)$ results of large grain cavities after EP treatment [4]

pits can be observed all over the cavity. The presence of grain boundaries is something special, compared to fine grain material. Since the grain size in the large grain material is on the order of centimetres, compared to the micrometre scale of the grains in fine grain material, a grain boundary would not have to be present necessarily at the quench location. For the inspected quench locations in the cavities AC151 to AC158, a grain boundary was always present in the vicinity. Grain boundaries in large grain material are very steep and sharp-edged in comparison to fine grain material. The sharpness of the edge is affected by the surface treatment. BCP tends to make edges more sharp while EP generally smoothens sharp features and makes them more round.

The effect of the different surface treatment on the grain boundaries in large grain cavities is exemplarily depicted in Fig. 7.37. The left part of the image shows the surface after the initial BCP treatment of 102 μm surface removal. The welding seam is at the left edge of the image, going from top to bottom. A grain boundary step is running perpendicular to the seam. As can be seen from the shadows that are cast by the incident light, the step is very steep and on the order of several 10 μm . The same spot is shown in the right part of the image after an additional surface removal of 20 μm by BCP and 72 μm by EP. As expected from the EP treatment, the grain boundary step is much smoother and more rounded.

The lack of obvious defects and the presence of the grain boundaries gives rise to the assumption that the grain boundaries and their change in geometry from the first test after BCP treatment to the second test after EP are related to the limitation of the gradient and

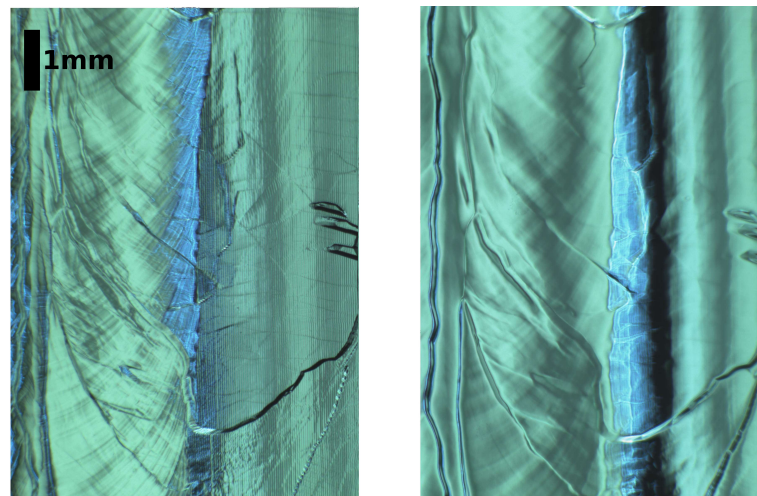


Figure 7.37: Comparison of the same grain boundary in AC158 before (left side) and after EP (right side)

thus the improvement in performance. [91] uses a model of magnetic field enhancement at grain boundaries leading to partially quenching at the grain boundaries to successfully simulate high-field Q-slope behaviour. The magnetic field enhancement at the sharp edges of the grain boundaries would be a possible explanation for the behaviour of the large grain cavities. Since the EP removes the sharpness and leads to bigger radii the enhancement after the EP is smaller, thus resulting in larger possible accelerating fields.

CHAPTER 8

The ILC yield database

A global cavity database has been established in order to collect the results of cavities that have been manufactured, treated and tested within the world wide R&D effort towards the ILC. This way of consistently collecting the cavity data from different laboratories allows for the monitoring of the goals that have been set for the cavity gradient in the GDE cavity R&D programme. The goals were to achieve 50 % process yield in 2010 and 90 % production yield in 2012; both at a gradient of 35 MV/m with $Q_0 \geq 8 \times 10^9$ [92]. Part of the installation of the database were the definition of the criteria for cavities to enter into the yield calculation. A group with an expert from each participating laboratory was formed to set up those criteria and enter the data of their respective data.

Technically, the database has been implemented as an adaptation of the cavity database at DESY within the TESLA Technology Collaboration [93], that is operating successfully since several years.

The database is available via a web-frontend. The data is entered in a separate web-form that is password protected. Only the designated experts of each laboratory have access and are in charge of entering their respective data. In the openly accessible part all the data of the included cavities is available. In addition with the simple press of two buttons it is possible to create the up-to-date yield plots according to the standardised rules. All cavities in the database that meet the selection criteria are included in these plots. It is also possible to create own selections of cavities and receive yield plots for this special selection.

8.1 Selection criteria

In the following, the selection criteria for the standard yield plots are described. Two yield plots are created by default. The first pass plot includes only the results for the initial test of cavities after their manufacturing. If a cavity doesn't reach the design goal for the gradient or quality factor in the first test, a re-treatment is necessary. Possible treatments are for example surface removal of another few ten micrometres by EP or high

pressure water rinsing. The result of a second test after such a re-treatment is included in the second pass yield plot.

8.1.1 First pass

The first requirement is that the mechanical manufacturing of the cavity has been done by what is considered a qualified vendor. That is the case, if a number of cavities has been built surpassing the specifications. For the yield plots only the ILC baseline cavity, the 9-cell TESLA shape cavity, is considered as it is well established and has successfully been built and operated over the past years. The cavities have to be built from fine grain material. The yield analysis only includes cavities with the full baseline treatment: two steps of EP (bulk removal and final treatment) followed by the appropriate cleaning steps, 800 °C degassing, 6 HPR cycles and baking at 120 °C. Cavities with full BCP or BCP flash processing are not taken into account. Also cavities with treatments that are still considered experimental, as vertical EP or tumbling, do not enter the yield plot.

For all cavities that meet the criteria above, the result of the first vertical test after completion of the fabrication and surface preparation is used for the yield plot. The test has to be regular, the performance of the cavity should not be limited by the testing system or other problems. If the test fails due to non-cavity reasons, the result of the next test is used, assuming that the cavity has not been treated in-between.

The result of what is called the "standard yield plot" is shown in Figure 8.1. Figure 8.1 includes all cavities that meet the above mentioned criteria, a total of 52 cavities. The plot holds the integrated data over time. The oldest test result is dating back to beginning of 2007 and the newest is from end of 2012. The yield at 35 MV/m is around 35 %. Binomial errors are given as errorbars.

8.1.2 Second pass

For the second pass yield plot also cavities with a re-treatment are considered. The selection criteria for the second pass plot are the following: Only cavities that are in the first pass plot can be in the second pass plot. For cavities, that reach or surpass 35 MV/m, it is assumed that they would not be processed further in the ILC cavity production. Therefore the result from the first test is also included in the second pass yield plot, even if a further test result should exist. It is possible, that a cavity doesn't reach 35 MV/m in the first test, but is not treated and tested a second time. That can be the case, if the cavity surpasses another gradient threshold, e.g. the 23.6 MV/m for the European XFEL. The cavity is then considered good enough, for its current goal.

For the re-treatment, the same procedures are allowed as in the first pass. In addition the treatment "HPR only" is included for cavities that only have received a high pressure water rinsing between the two tests, in most cases due to field emission in the first test.

Applying those additional criteria to the overall cavity data, the resulting yield plot looks

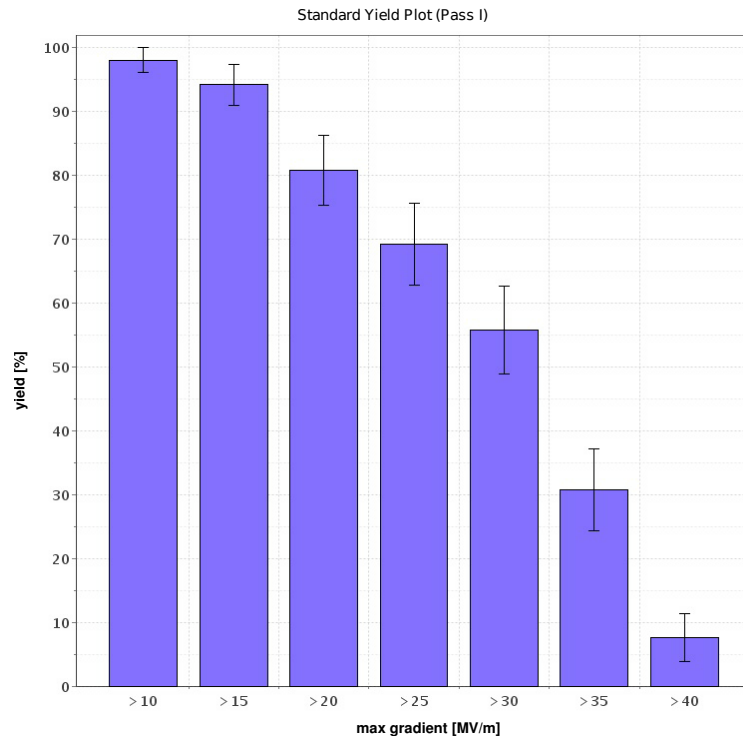


Figure 8.1: First pass yield plot of ILC cavity data, the yield plot includes 52 cavities. The yield at 35 MV/m is around 30 %

as shown in Figure 8.2. The plot now includes 38 cavities. The yield at 35 MV/m is now around 60 %.

8.1.3 Time evolution of the yield

In addition to just look at the current yield plot that includes all cavity tests up to the date the plot is produced, it is of interest to see the evolution of the yield over time. There are two possible ways of illustrating the time evolution. One is to take snap-shots in time of the standard yield plot that includes all cavities and merge all those snap-shots in one plot, as in Fig. 8.3. The other is to make differential plots presenting the yield at a certain gradient threshold including only the cavities of a certain time window as in Fig. 8.4.

In both options it is clearly visible, that the yield of the ILC R&D cavities increases over time. In the differential version the results of the effort to improve the cavity production and treatment as well as re-treatment options (especially visible in the second pass) is even more pronounced. For the bin of 2010-2012 the second pass yield has improved to $(75 \pm 11)\%$ at 35 MV/m and even $(94 \pm 6)\%$ at 28 MV/m.

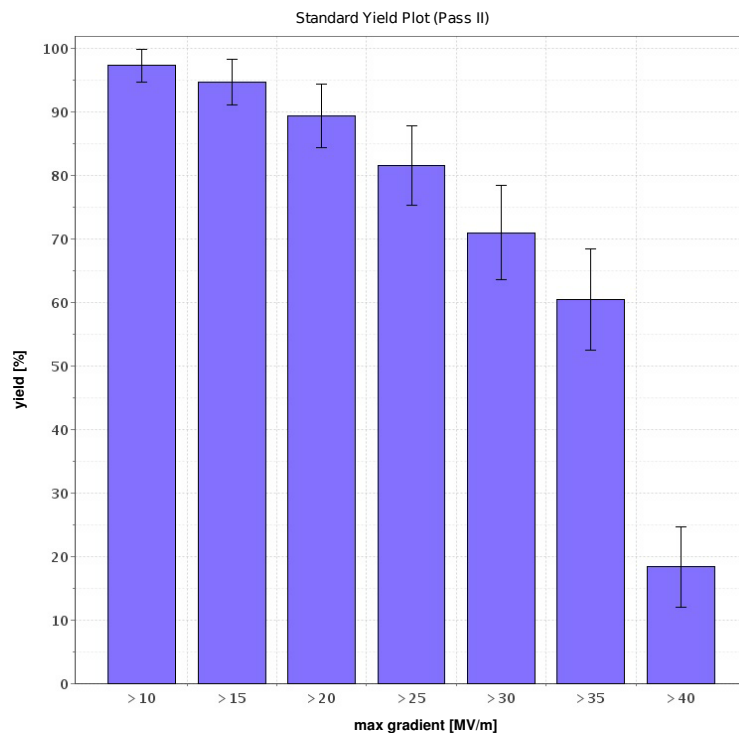
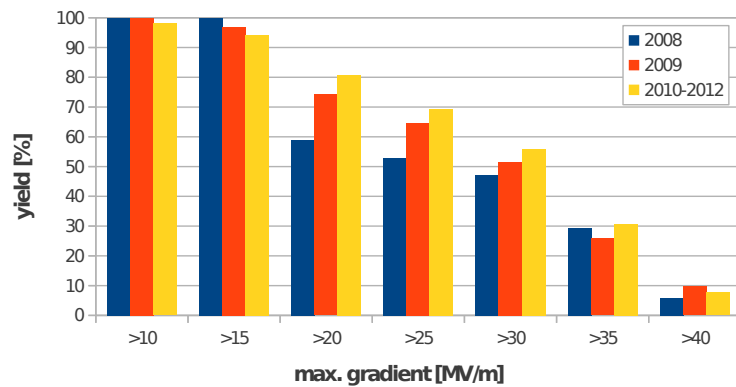
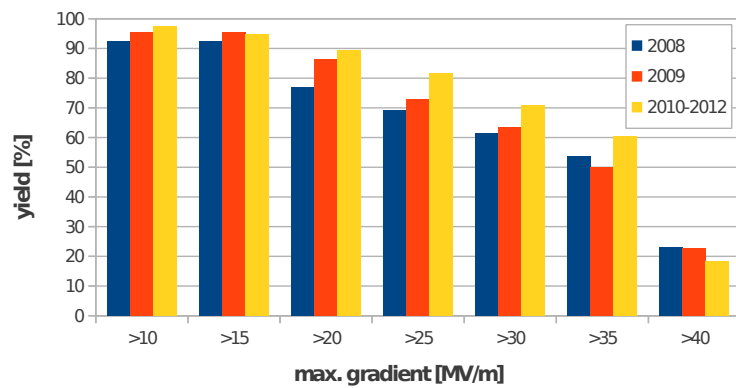


Figure 8.2: Second pass yield plot of ILC cavity data, the yield plot includes 38 cavities. The yield at 35 MV/m is around 60 %

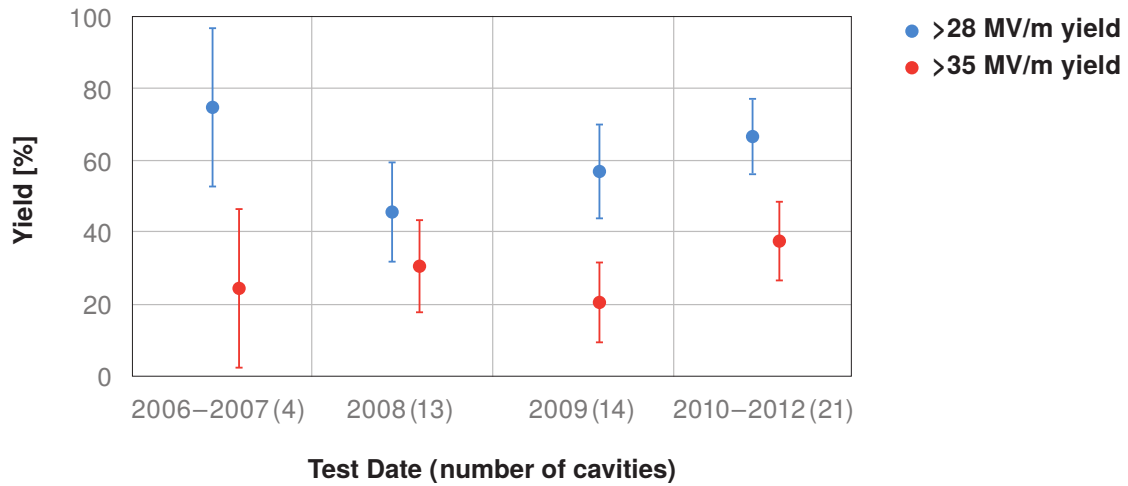


(a) First pass yield

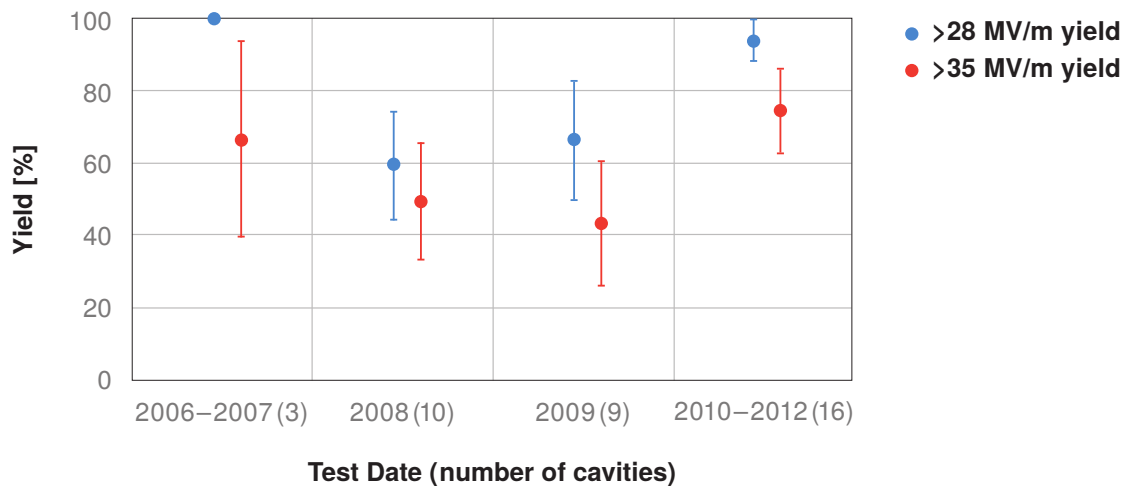


(b) Second pass yield

Figure 8.3: Time evolution of ILC cavity yield, three snap-shots of the yield histogram for the end of 2008, 2009 and 2012 are shown.



(a) First pass yield



(b) Second pass yield

Figure 8.4: Yield plots for first and second pass as function of time. The two gradient thresholds are 28 MV/m and 35 MV/m. For each time-span the number of cavities is given in parentheses. [92]

CHAPTER 9

Summary

This work was part of the global R&D effort that aims towards high accelerating gradients combined with a high yield for superconducting cavities for the ILC. The particular focus was optical inspection as a tool to study the inner surface of 1.3 GHz SRF cavities by using a novel inspection system from the collaboration of KEK and Kyoto University. With its combination of camera and adaptable illumination system pictures of unprecedented detail could be obtained from the inner surface without the need to dissect and thereby destroy the cavity. The insight from the analysis of these pictures has proven optical inspection to be a valuable addition to the number of quality assessment tools during cavity production.

The R&D on superconducting cavities in the last decades has improved their performance further and further. The last step for the European XFEL was the step from laboratory to a "series product". The complete production and preparation of the cavities is carried out by industry. With its 800 superconducting cavities the European XFEL will be the largest SRF accelerator world wide. Constituting 5 % of the intended total number of cavities of the ILC it is an optimal test bed how mass production could work and which tools for quality assessment would be beneficial.

In preparing the production of the European XFEL, a total of 32 different 9-cell cavities from the R&D phase have been inspected, supplemented by four 1-cell cavities and one 3-cell cavity. Most of the 9-cell cavities have been inspected several times during different stages of the surface preparation. This allowed monitoring of changes of the surface by the removal of material and tracking the evolution of defects. Findings from that data-sample are presented in this work.

Based on the experience gained with one of the first available models of the inspection system during the investigation of such a relatively large number of cavities, valuable feed-back for the improvements of the later versions could be given. In the final stage the KEK/Kyoto-camera was incorporated into a completely new inspection set-up at DESY. Within this work the optical inspection set-up OBACHT has been developed. Its parameters have been derived from the experience from the inspections with the early models.

OBACHT was designed and built to fit both the requirements of versatility in a laboratory as well as the robustness and reliability in a production environment. It is now able to perform optical inspections with the need for minimal operator interference in shorter times as in the manual set-up and is used in parts of the European XFEL series-production.

In the inspected cavities a number of examples have been observed, that differ from the smooth surface that is taken as a reference. These deviations have been catalogued. Not all features that are deviating from the standard in an optical picture automatically limit the cavity performance. The pictures from optical inspection have been compared with results from other methods, that determine the quench location by its generation of heat under operating conditions, like Tmap and second sound. In case of agreement the respective locations have been investigated in detail. Of special interest are those defects that lead to the breakdown of superconductivity. If responsible for a quench at low accelerating gradients, those defects are usually detectable with the available resolution and are also localised. Sometimes only one defect is limiting the performance of the entire 9-cell cavity and after removal the overall reachable accelerating gradient can be significantly higher.

While not all features that look suspicious limit the performance, there is also a number of cases where quenches occurred at positions without visible surface signature. Possible explanations are, that either the defect was too small in order to be seen with the available resolution, the defect is not on but hidden below the surface or simply not visible, as for example a transparent film.

In three special cases it was possible to dissect the cavity for further analysis. Through the additional investigation methods that were available for the extracted samples it was possible to trace the defect back to foreign material introduced during the production process as in the case of Z161 or defects from irregularities during the surface processing as in AC126.

Two types of limitations can be distinguished: those that are introduced due to deviations from the optimal process of cavity production and surface treatment and those that are of more fundamental nature. The former ones have been found in Z161 with aluminium as a foreign material, AC126 with marks from an error during high pressure water rinsing or AC151 with a collision between the cavity and the electropolishing cathode. Also Z142, where the defect could be traced by optical inspection through all steps of manufacture back to the state of the cavity directly after welding, is an example for cavity production related defects.

An example for the second type of limitations is the batch of eight large grain cavities. Their performance in the vertical test increased significantly after surface treatment by electropolishing compared to the earlier test results after buffered chemical polishing. In the subsequent optical inspections during their surface treatment no obvious defects were observed. Also at the quench locations indicated by Tmap and second sound nothing special was observed. The only feature that is common to all quench locations is the presence of grain boundaries. A possible explanation for the better performance is thus a rounding

of the grain boundaries by the electropolishing, as opposed to the much sharper edges produced by the buffered chemical polishing.

In the scope of this thesis the ILC global yield database was implemented as a tool to collect and assess the results of the international R&D effort on SRF cavities at the different labs. During its development the yield and rules for the selection of cavities for first and second pass of treatment have been defined. This ensures the comparability of the worldwide results. The ILC yield DB has helped to track and evaluate the progress towards achieving the R&D goals of the ILC, as published in the technical design report.

Optical inspection of the inner surface with a high resolution camera, as described in this thesis, is now a well established method for quality assessment during the production of superconducting cavities. It is being used in parts of the European XFEL series-production and has given valuable feedback to the cavity manufacturers in order to refine the production process. By identifying defects and their likely origins it is possible to understand the discrepancy between individual nine-cell cavities reaching record results of 45 MV/m and the production of bigger numbers still scattering around significantly lower values. The feedback from optical inspection helps to understand which parts of the production process have to be monitored and corrected especially.

Once detected, defects can be addressed and removed by adequate repair techniques, e.g. grinding. If integrated at intermediate steps of the production process optical inspection is able to detect possible problematic features early and to take countermeasures. Thereby it contributes to raising the maximum gradient of individual cavities and yield at high gradients of an overall production.

The current recipe for cavity production and preparation has proven to effectively result in high accelerating gradients. Pursuing each step with highest elaborateness, aided by optical inspection, ought to get rid of limitations at low accelerating fields and yield cavities up to the ILC requirements. All this adds to the needed know-how and will help to achieve the goals during a mass-production for the ILC.

APPENDIX A

Data for yield plots

A Data for yield plots

No.	Cavity	Test Date	Max. Eacc [MV/m]
1	TB9ACC013	01.Dec.08	41.80
2	TB9ACC014	09.Feb.09	41.50
3	TB9AES008	26.Aug.09	41.10
4	TB9AES007	16.Mar.10	41.00
5	MHI021	12.Apr.12	38.90
6	AC122	26.Aug.08	38.88
7	AC115	11.Dec.07	38.60
8	MHI017	06.Feb.11	38.40
9	CAV00004	06.Mar.12	38.09
10	TB9RI019	11.Jun.10	38.00
11	TB9AES010	06.Nov.09	37.70
12	CAV00002	09.Mar.12	37.58
13	MHI012	11.Nov.10	37.50
14	TB9ACC011	21.Aug.08	37.00
15	MHI013	25.Nov.10	36.20
16	TB9ACC012	07.Jul.08	35.10
17	Z134	13.Nov.09	34.94
18	AC125	15.Jul.08	34.59
19	AC150	30.Jan.09	34.33
20	TB9AES009	18.Aug.09	33.40
21	TB9RI018	15.Apr.10	33.10
22	Z143	09.Oct.08	32.57
23	Z106	21.Feb.07	31.70
24	MHI022	10.May.12	31.50
25	AC127	13.Feb.09	31.25
26	TB9ACC016	14.Dec.09	31.20
27	Z162	24.Mar.11	31.01
28	TB9RI027	09.Sep.10	31.00
29	MHI018	16.Feb.12	31.00
30	ACCEL7	05.Sep.06	29.00
31	CAV00001	09.Feb.12	28.42
32	AC149	28.Jan.09	26.51
33	MHI019	01.Mar.12	26.30
34	AC146	06.May.10	26.13
35	AC124	05.Feb.09	26.01
36	Z137	24.Feb.09	25.23
37	Z139	12.Sep.08	24.93
38	MHI015	03.Feb.11	22.50
39	TB9RI028	01.Oct.10	22.00
40	MHI016	19.May.11	20.77
41	Z142	01.Jul.09	20.58
42	TB9AES005	27.Mar.09	20.50
43	ACCEL6	12.Dec.06	19.00
44	Z141	16.Apr.08	18.29
45	TB9ACC015	02.Jul.08	18.00
46	Z130	01.Sep.08	17.30
47	Z131	20.Aug.08	17.17
48	Z132	19.Aug.08	16.83
49	AC126	05.Sep.08	16.37
50	MHI014	20.Jan.11	15.00
51	TB9AES006	30.Apr.09	14.10
52	MHI020	15.Mar.12	9.00

(a) First pass

No.	Cavity	Test Date	Max. Eacc [MV/m]
1	TB9ACC013	01.Dec.08	41.80
2	TB9ACC014	09.Feb.09	41.50
3	ACCEL7	18.Jan.07	41.20
4	TB9AES008	26.Aug.09	41.10
5	Z143	12.Nov.08	41.00
6	TB9AES007	16.Mar.10	41.00
7	AC146	04.Aug.11	40.18
8	TB9ACC012	21.Jul.08	39.90
9	TB9ACC016	11.Feb.10	39.30
10	TB9RI018	02.Jun.10	39.00
11	MHI021	12.Apr.12	38.90
12	AC122	26.Aug.08	38.88
13	TB9RI028	18.Oct.10	38.80
14	AC115	11.Dec.07	38.60
15	MHI017	06.Feb.11	38.40
16	CAV00004	06.Mar.12	38.09
17	TB9RI019	11.Jun.10	38.00
18	TB9AES010	06.Nov.09	37.70
19	CAV00002	09.Mar.12	37.58
20	MHI012	11.Nov.10	37.50
21	TB9ACC011	21.Aug.08	37.00
22	MHI013	25.Nov.10	36.20
23	TB9AES009	07.Oct.09	36.00
24	TB9RI027	11.Oct.10	34.80
25	AC150	08.May.09	33.23
26	Z139	20.Oct.08	32.75
27	AC124	19.May.09	30.93
28	Z162	14.Nov.11	29.37
29	ACCEL6	23.Jan.07	29.00
30	CAV00001	22.Mar.12	28.66
31	AC127	11.Jun.09	27.85
32	TB9AES006	11.Sep.09	22.20
33	Z141	14.May.08	20.70
34	TB9AES005	09.Apr.09	20.50
35	Z131	25.Nov.08	17.96
36	Z130	15.Oct.08	16.60
37	MHI014	17.Feb.11	13.00
38	AC126	21.Oct.08	6.14

(b) Second pass

Figure A.1: Data of cavities included in the first and second pass yield plot

APPENDIX B

Spots in Z161

B Spots in Z161

Table B.1: List of spots in cavity Z161, cells 1-7, in initial state, after US rinsing and after bulk and final EP. Each position with a black spot in the first optical inspection is listed. Spots that were removed by US rinsing or EP are marked with an x. An o indicates spots that were not removed by the surface treatment. (o) indicates spots that are almost removed and only barely visible.

Cell	Angle	after US rinse	after bulk EP	after final EP
1	143	x		
	184	o	o	o
2	128	o	o	o
	153	x		
	169	x		
	193	x		
3	33	x		
	117	o	o	o
	145	x		
	149	x		
	181	o	o	(o)
	225	o	o	(o)
	237	o	o	(o)
	254	o	o	o
	274	x		
	285	x		
	293	o	o	(o)
300	x			
4	36	x		
	52	x		
	108	o	o	o
	160	x		
	180	?	o	o
	189	o	o	o
	201	x		
5	64	x		
	68	x		
	129	x		
	188	o	o	o
	248	o	o	o
272	o	o	o	
6	96	o	x	x
	168	o	(o)	x
	284	x		
	324	x		
7	32	o	x	
	51	x		
	64	o	o	(o)
	308	o	o	(o)

Table B.2: List of spots in cavity Z161, cells 8 and 9, in initial state, after US rinsing and after bulk and final EP. Each position with a black spot in the first optical inspection is listed. Spots that were removed by US rinsing or EP are marked with an x. An o indicates spots that were not removed by the surface treatment. (o) indicates spots that are almost removed and only barely visible.

Cell	Angle	after US rinse	after bulk EP	after final EP	
8	17	x			
	57	o	o	(o)	
	61	x			
	101	o	(o)	x	
	136	x			
	141	x			
	193	x			
	216	o	x		
	232	x			
	284	x			
	296	o	(o)	x	
	320	x			
	9	8	x		
		16	x		
20		x			
24		x			
28		x			
40		x			
48		x			
52		x			
56		x			
64		x			
108		x			
132		x			
148		x			
160		x			
168		x			
192		o	(o)	(o)	
196		x			
236		o	o	o	
262	o	o	o		
268	x				
350	o	x			
356	x				

List of Figures

2.1	Particles in the standard model	6
2.2	Birds-eye view of the future European XFEL	9
2.3	ILC design layout	11
3.1	9-cell cavity with field-lines	13
3.2	Cross-section of a TESLA -shape 9-cell cavity	14
3.3	Field distribution in different modes	15
3.3	Field distribution in different modes	16
3.4	Shielding of external magnetic field and flux trapping in perfect conductor	18
3.5	Meissner-Ochsenfeld effect	20
3.6	B-T-phase-diagrams	21
3.7	Metal-insulator-vacuum and metal-insulator-metal model	22
3.8	Typical Q(E)-curve for a cavity limited by FE	23
3.9	Schematic of thermal breakdown	24
3.10	Secondary electron emission coefficient for niobium	26
3.11	Example-curve for Q-switch	27
4.1	Two possible contours of the two half-cells before welding of the equator seam	31
4.2	Preparation scheme for the preparation of European XFEL cavities at DESY	32
4.3	Viscous layer forming during EP and its different thickness due to pro- truding features and pits [35]	34
4.4	Impact of 120 °C bake on the Q(E)-curve of cavity 1AC8, before baking (blue circles) and after baking (red squares)	35
5.1	Schematic drawing of the vertical test cryostat	38
5.2	Accelerating gradient in MV/m for all cells measured in all nine modes .	39
5.3	Rotating temperature mapping system at DESY	40
5.4	Typical result of a temperature mapping	41
5.5	Principle of second sound formation and propagation	42
5.6	Schematic drawing of second sound detection with an OST	43
6.1	Comparison between borescope and camera	46
6.2	Comparison between borescope and camera	46

List of Figures

6.3	Relevant areas of an equator welding seam as obtained in optical inspection, indicated are the welding seam itself, the heat affected zone (HAZ) next to it and the bulk material	47
6.4	Schematic view of the camera system in use at DESY: The camera cylinder is inserted into a cavity	48
6.5	Detailed camera schematic	48
6.6	Comparison of images by different camera systems	50
6.7	Illustration Depth of field	51
6.8	Standard illumination patterns	53
6.9	Geometric view of set-up for the measurement of the surface profile	54
6.10	Cavity coordinate system	55
6.11	Photograph of the OBACHT setup	56
7.1	Standard equator welding seam	60
7.2	Standard iris welding seam	61
7.3	Curvy welding seam	62
7.4	Welding overlap	63
7.5	Grainboundary in large-grain cavity	65
7.6	Traces of grinding on iris	66
7.7	Black spot next to welding seam	67
7.8	Coloured spots at iris	68
7.9	Dust and dirt on cavity surface	69
7.10	Scratch at Iris	70
7.11	Circular pit on iris	71
7.12	Circular pit at equator	72
7.13	Small pits on equator welding seam	72
7.14	Steps at grain-boundaries and rough grains	73
7.15	7.15a: Hotspot located by Tmap in cell 2 at 85 degrees near equator of AC126, 7.15b:Optical inspection image of the respective location	76
7.16	7.16a: SEM image of the defect at the quench location in AC126, 7.16b, 7.16c and 7.16d: Detailed view with increased magnification of the crystal structures grown on the surface	77
7.17	Element abundance line-scan in AC126	78
7.18	Removal of spots in Z161 by US rinsing and EP	80
7.19	Evolution of defect in Z161	81
7.20	7.20a: Hotspot located by Tmap in cell 2 at 128 degrees near equator of Z161, 7.20b:Optical inspection image of the respective location	82
7.21	SEM image of the defect at the quench location in Z161 7.21a: Overview of the defect 7.21b: Close-up of the structures on the defect plateau	83
7.23	7.23a: Hotspot located by Tmap in cell 5 around 25 degrees near equator of Z130, 7.23b:Optical inspection image of the respective location. A circular defect is visible on the left edge of the welding seam.	85

7.24	Profile of the defect in Z130. The maximum difference in height is 265 μm . [89]	86
7.25	SEM image of the left edge of the round defect extracted from Z130. Small substructures on the order of few micrometers and sharp edges are visible.	86
7.26	Q(E)-curve of AC151 in test no. 4 with Q-switches starting at a gradient of 16.7 MV/m (blue circles) and Q(E)-curve in test no. 5 after the successful repair (red squares)	87
7.27	7.27a: Optical inspection image of the damaged antenna tip at HOM 2 in AC151. An undamaged tip is smooth and shiny. 7.27b: Damaged HOM antenna seen from outside the cavity	87
7.28	SEM picture of sample from HOM antenna in AC151	88
7.29	EDX-spectra of sample from HOM antenna in AC151	89
7.30	Limiting defect in cavity Z142: Hotspot located by Tmap in cell 6 during quench at 20 MV/m and picture of the respective area in the cavity with defect	90
7.31	Comparison of the same defect in Z142 at three different surface preparation stages: Before surface treatment (upper part), after bulk EP (middle part) and after final EP (lower part)	91
7.32	Influence of grinding on AC71	91
7.33	Dependency of defect size and gradient at DESY	94
7.34	Dependency of defect size and gradient at KEK	94
7.35	Q(E) of LG cavities after BCP	95
7.36	Q(E) of LG cavities after EP	96
7.37	Grain boundary before and after EP	97
8.1	First pass yield plot of ILC cavity data, the yield plot includes 52 cavities. The yield at 35 MV/m is around 30 %	101
8.2	Second pass yield plot of ILC cavity data, the yield plot includes 38 cavities. The yield at 35 MV/m is around 60 %	102
8.3	Time evolution of yield, integrated	103
8.4	Differential yield plots	104
A.1	Cavity data for yield plots	110

List of Tables

2.1	Nominal ILC parameter set	12
4.1	XFEL niobium specification	30
6.1	Parameters of camera systems	49
7.1	Risk assessment for optical features	74
7.2	Defects for correlation of defect size and gradient	93
B.1	Spots in Z161, cells 1-7	112
B.2	Spots in Z161, cells 8 and 9	113

References

- [1] F. Zimmermann, M. Benedikt, D. Schulte, and J. Wenniger. Challenges for highest energy circular colliders. In *Proceedings of IPAC14*, 2014. 1
- [2] Ties Behnke, James E. Brau, Brian Foster, et al. The International Linear Collider Technical Design Report - Volume 1: Executive Summary. 2013. 1, 12
- [3] B. Aune, R. Bandelmann, D. Bloess, et al. Superconducting TESLA cavities. *Physical Review Special Topics - Accelerators And Beams*, 3(9):092001, Sep 2000. 2, 10
- [4] D. Reschke, S. Aderhold, A. Goessel, et al. Results on Large Grain Nine-Cell Cavities at DESY: Gradients up to 45 MV/m after Electropolishing. In *Proceedings of the 15th International Conference on RF Superconductivity*, 2011. 2, 33, 95, 96
- [5] K. Nakamura and others (Particle Data Group). Review of Particle Physics. *Journal of Physics G: Nuclear and Particle Physics*, 37:075021, 2010. 6
- [6] F. Abe, H. Akimoto, A. Akopian, et al. Observation of Top Quark Production in $\bar{p}p$ Collisions with the Collider Detector at Fermilab. *Phys. Rev. Lett.*, 74:2626–2631, Apr 1995. 5
- [7] S. Abachi, B. Abbott, M. Abolins, et al. Observation of the Top Quark. *Phys. Rev. Lett.*, 74:2632–2637, Apr 1995. 5
- [8] Peter W. Higgs. Broken Symmetries and the Masses of Gauge Bosons. *Phys. Rev. Lett.*, 13:508–509, Oct 1964. 5
- [9] Peter W. Higgs. Broken symmetries, massless particles and gauge fields. *Phys. Lett.*, 12:132–133, 1964. 5
- [10] L. Evans and P. Bryant. LHC Machine. *JINST*, 3:S08001, 2008. 5
- [11] The ATLAS Collaboration. The ATLAS Experiment at the CERN Large Hadron Collider. *Journal of Instrumentation*, 3(08):S08003, 2008. 5
- [12] The CMS Collaboration. The CMS experiment at the CERN LHC. *JINST*, 3:S08004, 2008. 5

References

- [13] The ATLAS Collaboration. Observation of a new particle in the search for the Standard Model Higgs boson with the ATLAS detector at the LHC. *Phys.Lett.B*, 716(1):1–29, 2012. 5
- [14] The CMS Collaboration. Observation of a new boson at a mass of 125 GeV with the CMS experiment at the LHC. *Physics Letters B*, 716(1):30 – 61, 2012. 5
- [15] E. Komatsu, J. Dunkley, M. R. Nolta, et al. Five-Year Wilkinson Microwave Anisotropy Probe Observations: Cosmological Interpretation. *The Astrophysical Journal Supplement Series*, 180(2):330, 2009. 7
- [16] P. Fayet and S. Ferrara. Supersymmetry. *Phys. Rept.*, 32:249–334, 1977. 7
- [17] S. Dimopoulos, S. Raby, and F. Wilczek. Supersymmetry and the Scale of Unification. *Physical Review D: Particles and Fields*, 24:1681–1683, 1981. 7
- [18] ILC-TRC. International Linear Collider Technical Review Committee, Second report. Technical Report SLAC-R-606, 2003. 8
- [19] S. Takeda. Japan Linear Collider (JLC). *Particle Accelerators*, 30:134–152, 1990. 8
- [20] C. Adolphsen, R. Aiello, R. Alley, et al. Zeroth Order Design Report For The Next Linear Collider. Technical Report SLAC-R-474, The NLC Design Group, 1996. 8
- [21] F. Richard, (ed.), J. R. Schneider, (ed.), D. Trines, (ed.), and A. Wagner, (ed.). TESLA: The superconducting electron positron linear collider with an integrated X-ray laser laboratory. Technical design report. Pt. 1: Executive Summary. Technical report, TESLA, 2001. 8
- [22] D. A. Edwards, (ed.). TESLA TEST FACILITY LINAC - Conceptual Design Report. Technical report, TESLA, 1995. 8
- [23] Carlo Pagani. Developments and Achievements at the TESLA Test Facility (TTF). *IEEE Transactions on Applied Superconductivity*, 9(2):276–281, June 1999. 8
- [24] J. Rossbach. The VUV Free Electron Laser Based on the TESLA Test Facility at DESY. In *Proceedings of EPAC98*, 1998. 9
- [25] J. Andruszkov, B. Aune, V. Ayvazyan, et al. First Observation of Self-Amplified Spontaneous Emission in a Free-Electron Laser at 109nm Wavelength. *Physical Review Letters*, 85(18):3825–3829, 2000. 9
- [26] S. Schreiber. First Lasing in the Water Window with 4.1nm at FLASH. In *Proceedings of FEL2011*, 2011. 9

-
- [27] M. Altarelli et al. The European X-Ray Free Electron Laser Technical Design Report. Technical Report DESY 06-97, Deutsches Elektronen-Synchrotron DESY, 2007. 9, 14, 30
- [28] ITRP Recommendation, 2004.
http://www.fnal.gov/directorate/icfa/ITRP_Report_Final.pdf. 10
- [29] J. Brau, (ed.), Y. Okada, (ed.), and N. Walker, (ed.). International Linear Collider Reference Design Report, Volume 1: Executive Summary. Technical report, ILC Global Design Effort, 2007. 10
- [30] J. Bagger, T. Behnke, P. Burrows, et al. The International Linear Collider: Gateway to the Quantum Universe, 2008. 11
- [31] H. Aihara, (ed.), P. Burrows, (ed.), and M. Oreglia, (ed.). SiD Letter of Intent, 2009. 11
- [32] ILD Concept Group. The International Large Detector: Letter of Intent, 2010. DESY-2009-87. 11
- [33] M. Pekeler. *Untersuchungen der feldbegrenzenden Mechanismen in supraleitenden Niob-Resonatoren*. PhD thesis, Universität Hamburg, 1996. 13, 38
- [34] W. Meissner and R. Ochsenfeld. Ein neuer Effekt bei Eintritt der Supraleitfähigkeit. *Naturwissenschaften*, 21(44):787–788, 1933. 17
- [35] L. Lilje. *Experimental Investigations on Superconducting Niobium Cavities at Highest Radiofrequency Fields*. PhD thesis, Universität Hamburg, 2001. 21, 30, 33, 34, I
- [36] F. London and H. London. The Electromagnetic Equations of the Supraconductor. *Proceedings of the Royal Society of London. Series A, Mathematical and Physical Sciences*, 149(866):71–88, Mar 1935. 19
- [37] R. H. Fowler and L. Nordheim. Electron Emission in Intense Electric Fields. *Proceedings of the Royal Society of London. Series A*, 119(781):173–181, 1928. 21
- [38] H. Padamsee, J. Knobloch, and T. Hays. *RF Superconductivity for Accelerators*. Wiley-VCH Verlag, Weinheim, 2008. 22, 24, 29, 82
- [39] M. Jimenez, R. J. Noer, G. Jouve, J. Jodet, and B. Bonin. Electron field emission from large-area cathodes: evidence for the projection model. *J. Phys. D: Appl. Phys.*, 27:1038, 1994. 22
- [40] R. Latham, editor. *High Voltage Vacuum Insulation*. Academic Press, 1995. 22

References

- [41] Y. Yamamoto, H. Hayano, E. Kako, et al. Summary of results and development of online monitor for T-mapping/X-ray-mapping in KEK-STF. In *Proceedings of IPAC10*, 2010. 23
- [42] H. Padamsee, D. Proch, P. Kneisel, and J. Mioduszewski. Field strength limitations in superconducting cavities - multipacting and thermal breakdown. *IEEE Transactions on Magnetics*, 17:947–950, Jan 1981. 24
- [43] G. Eremeev, R. L. Geng, and A. D. Palzcewski. Probing the fundamental limit of niobium in high radiofrequency fields by dual mode excitation in superconducting radiofrequency cavities. In *Proceedings of the 15th International Conference on RF Superconductivity*, 2011. 24
- [44] H. Padamsee. Calculations for breakdown induced by "Large defects" in superconducting niobium cavities. *Magnetics, IEEE Transactions on*, 19(3):1322–1325, 1983. 25
- [45] D. Proch and U. Klein. Multipacting in superconducting RF structures. In *Proceedings Conference for Future Possibilities for Electron Accelerators*, 1979. 25
- [46] P. Ylae-Oijala. Electron multipacting in TESLA cavities and input couplers. *Particle Accelerators*, 63:105–137, 1999. 25
- [47] H. Piel. Superconducting Cavities. In S. Turner, editor, *Superconductivity in Particle Accelerators*, 1989. CERN 89-04. 26
- [48] B. Bonin and R. W. Röth. Q degradation of Niobium cavities due to Hydrogen contamination. In *Proceedings of the 5th Workshop on RF Superconductivity*, 1991. 26
- [49] W. Singer, D. Proch, and A. Brinkmann. Diagnostic of Defects in High Purity Niobium. In *Proceedings of the 1997 Workshop on RF Superconductivity*, 1997. 29
- [50] W. Singer, S. Aderhold, J. Iversen, et al. Development of large grain superconducting resonators for the European XFEL. In *Proceedings of the 23rd PAC09*, 2009. 29
- [51] H. Umezawa. Niobium Production at Tokyo Denkai. In *AIP Conference Proceedings*, number 1352, pages 79–83, 2010. 29
- [52] W. Singer, S. Aderhold, A. Ermakov, et al. Development of large grain cavities. *Phys. Rev. ST Accel. Beams*, 16:012003, Jan 2013. 29
- [53] W. Singer, A. Brinkmann, D. Proch, and X. Singer. Quality requirements and control of high purity niobium for superconducting RF cavities. *Physica C: Superconductivity*, 386(0):379 – 384, 2003. Proceedings of the topical conference

-
- of the International Cryogenic Materials Conference (ICMC 2002).
Superconductors for Practical Applications. 30
- [54] W. Singer and A. Brinkmann. Final Report on SQUID Scanning. Technical Report CARE-Report-2008-024-SRF, CARE, 2008. 30
- [55] J. Iversen, T. Buettner, A. Goessel, et al. Development and Design of a RF-measurement machine for the European XFEL cavity fabrication. In *Proceedings of the 14th International Conference on RF Superconductivity*, 2009. 30
- [56] J. L. Kirchgessner. Forming and Welding of Niobium for Superconducting Cavities. In *Proceedings of the third Workshop on RF Superconductivity*, 1987. 30
- [57] J. H. Thie, A. Goessel, J. Iversen, et al. Mechanical Design of Automatic Cavity Tuning Machines. In *Proceedings of SRF2009*, 2009. 31
- [58] J. H. Thie, A. Goessel, J. Iversen, et al. Commissioning and Upgrade of Automatic Cavity Tuning Machines for the European XFEL. In *Proceedings of the 15th International Conference on RF Superconductivity*, 2011. 31
- [59] W. Singer, H. Kaiser, X. Singer, et al. Hydroforming of Superconducting TESLA Cavities. In *The 10th Workshop on RF Superconductivity*, 2001. 31
- [60] X. Singer, W. Singer, I. Jelezov, A. Matheisen, and P. Kneisel. Hydroforming of Multi-Cell Niobium and NbCu-clad Cavities. In *Proceedings of the 23rd PAC09*, 2009. 31
- [61] M. Schalwat, K. Escherich, N. Krupka, et al. Update of the DESY Infrastructure for Cavity Preparation. In *Proceedings of the 15th International Conference on RF Superconductivity*, 2011. 31
- [62] D. Reschke, L. Lilje, and H. Weise. Analysis of RF results of recent nine-cell cavities at DESY. In *Proceedings of the 14th international conference on RF superconductivity*, 2009. 32
- [63] P. Kneisel, R. W. Roeth, and H.-G. Kuerschner. Results from a nearly "Defect-free" Niobium Cavity. In *Proceedings of the 1995 Workshop on RF Superconductivity*, 1995. 33
- [64] H. Diepers, O. Schmidt, H. Martens, and F.S. Sun. A new method of electropolishing niobium. *Physics Letters A*, 37(2):139 – 140, 1971. 33
- [65] W. C. Elmore. Electrolytic Polishing. *J. Appl. Phys.*, 10:724–727, 1939. 33

References

- [66] A. Matheisen, B. van der Horst, B. Petersen, S. Saegbarth, and P. Schilling. Preparation Sequences for Electro-polished High Gradient Multi-Cell Cavities at DESY. In *Proceedings of the 12th International Workshop on RF Superconductivity*, 2005. 34
- [67] A. Aspart, F. Eozenou, and C. Antoine. Aluminum and Sulphur particles in Electropolishing Baths. In *Proceedings of the 12th International Workshop on RF Superconductivity*, 2005. 34
- [68] N. Steinhau-Kuehl, A. Matheisen, L. Lilje, et al. Update on the Experiences of Electropolishing of Multi-Cell Resonators at DESY. In *Proceedings of the 12th International Workshop on RF Superconductivity*, 2005. 34
- [69] H. Padamsee. *RF Superconductivity*. Wiley-VCH Verlag, Weinheim, 2009. 34
- [70] B. van der Horst, A. Matheisen, B. Petersen, S. Saegbarth, and P. Schilling. Update on cavity preparation for high gradient superconducting multicell cavities at DESY. In *Proceedings of the 13th International Workshop on RF Superconductivity*, 2007. 34
- [71] M. Schmoekel, A. Matheisen, B. Petersen, N. Steinhau-Kuehl, and H. Weitkaemper. Update on EP experiences at DESY with the electro-polishing process at DESY 1.3 GHz. In *Proceedings of the 13th International Workshop on RF Superconductivity*, 2007. 34
- [72] D. Reschke and L. Lilje. Recent experience with nine-cell cavity performance at DESY. In *Proceedings of the 13th International Workshop on RF Superconductivity*, 2007. 34
- [73] P. Clay, J. P. Desvard, R. Duthil, et al. Cryogenic and Electrical Test Cryostat for Instrumented Superconductive RF Cavities (CHECHIA). In *Proceedings of CEC/ICMC 1995*, 1995. 37
- [74] Q. S. Shu, G. Deppe, W.-D. Möller, et al. An advanced rotating T-R mapping & its diagnoses of TESLA 9-cell superconducting cavity. *Proceedings of the 1995 Particle Accelerator Conference*, 3:1639–1641, 1995. 40
- [75] F. Schländer and H. Vennekate. Second Sound as diagnostic tool for SCRF cavities. In *3rd Annual Workshop of the Helmholtz Alliance "Physics at the Terascale"*, 2009. 42
- [76] Z. A. Conway, D. L. Hartill, H. Padamsee, and E. N. Smith. Oscillating Superleak Transducers for Quench Detection in Superconducting ILC Cavities cooled with Helium-II. In *Proceedings of the XXIV Linear Accelerator Conference*, 2008. 43

-
- [77] F. Schlander, E. Elsen, and D. Reschke. Second Sound as an Automated Quench Localisation Tool at DESY. In *Proceedings of the 15th International Conference on RF Superconductivity*, 2011. 43
- [78] F. Schlander. *Study of Quality and Field Limitation of Superconducting 1.3 GHz 9-Cell RF-Cavities at DESY*. PhD thesis, Universität Hamburg, 2012. 43
- [79] F. Schlander, S. Aderhold, D. Reschke, and K. Twarowski. Recent Results from Second Sound, T-Mapping and Optical Inspection of 1.3 GHz Cavities at DESY. In *Proceedings of the 15th International Conference on RF Superconductivity*, 2011. 44
- [80] M. Wenskat, S. Aderhold, E. Elsen, et al. Image processing for characterisation of surfaces of superconducting RF cavities. In *Proceedings of IPAC12*, 2012. 46
- [81] Y. Iwashita, Y. Tajima, and H. Hayano. Development of high resolution camera for observations of superconducting cavities. *Physical Review Special Topics - Accelerators And Beams*, 11:093501, 2008. 49
- [82] K. Saito, H. Inoue, E. Kako, et al. Superiority of Electropolishing over Chemical Polishing on High Gradients. In *Proceedings of the 1997 Workshop on RF Superconductivity*, 1997. 52
- [83] K. Watanabe. Recent results by Kyoto-camera. Talk at TTC Meeting, October 2008. 53
- [84] Y. Tajima. in Japanese. Master's thesis, Department of Physics, Kyoto University, 2007. 54
- [85] S. Aderhold, E. Elsen, F. Schlander, and L. Steder. A Common Cavity Coordinate System. Technical report, ILC HiGrade, 2010. 54, 55
- [86] M. Lemke, E. Elsen, S. Aderhold, et al. OBACHT - Optical Bench for Automated Cavity Inspection with High Resolution on Short Timescales. Technical report, ILC Higrade, 2013. 57
- [87] X. Singer, S. Aderhold, A. Ermakov, et al. Investigation of Samples Separated From Prototype Cavities of the European XFEL. In *Proceedings of the 15th International Conference on RF Superconductivity*, 2011. 76
- [88] P. D. Desai, H. M. James, and C. J. Ho. Electrical Resistivity of Aluminum and Manganese. *J. Phys. Chem. Ref. Data*, 13(4):1131–1172, 1984. 82
- [89] W. Singer and X. Singer. Kein Fremdmaterial in Defekt in Z130. 84, 86, III

References

- [90] Y. Yamamoto, H. Hayano, E. Kako, et al. Achieving high gradient performance of 9-cell cavities at KEK for the international linear collider. *Nuclear Instruments and Methods in Physics Research Section A: Accelerators, Spectrometers, Detectors and Associated Equipment*, 729(0):589 – 595, 2013. 93, 94
- [91] J. Knobloch, R. L. Geng, M. Liepe, and H. Padamsee. High-Field Q Slope in Superconducting Cavities Due to Magnetic Field Enhancement at Grain Boundaries. In *Proceedings of the 1999 Workshop on RF Superconductivity*, 1999. 97
- [92] C. Adolphsen, M. Barone, B. Barish, et al. The International Linear Collider Technical Design Report - Volume 3.I: Accelerator R & D in the Technical Design Phase. 2013. 99, 104
- [93] P.-D. Gall, A. Goessel, V. Gubarev, and J. Iversen. A Database For Superconducting Cavities. In *Proceedings of SRF2007*, 2007. 99

Danksagung

Das Schreiben dieser Zeilen bedeutet für mich den Abschluss eines langen Kapitels in meinem Leben. An dieser Stelle möchte ich mich bei allen bedanken, die zum Gelingen beigetragen haben.

Ein ganz besonderer Dank gilt meinen Eltern für ihre fortwährende Unterstützung während Studium und Promotionszeit.

Bei Eckhard Elsen bedanke ich mich für die Betreuung und dass er mir von Anfang die Möglichkeit gegeben hat zu erfahren, warum es *International* Linear Collider heißt. Der Besuch von internationalen Konferenzen und Workshops und die Zusammenarbeit mit den Kollegen aus Laboren auf der ganzen Welt waren der Ausgangspunkt für viele tolle Erfahrungen und Möglichkeiten.

Following that I would like to thank Hayano-san and Iwashita-san for giving me the possibility to work with one of the very early versions of the Kyoto/KEK inspection system that was essential for the research for my thesis.

Not only in the context of the ILC cavity database I was very happy to work with Zachary Conway, Rongli Geng and Kirk Yamamoto. I especially enjoyed working and discussing with Camille Ginsburg while developing yield plots and selection criteria for cavities.

Bei DESY gibt es eine ganze Reihe von Kollegen die durch ihre Unterstützung ganz maßgeblich am Gelingen dieses Projektes beteiligt waren. Für die Zusammenarbeit in allen Belangen rund um die Datenbank bin ich Dieter Gall, Vladimir Gubarev und Sibel Yasar sehr dankbar.

OBACHT entstand im Team mit Uwe Cornett, Gert Falley, Sven Karstensen, Torsten Külper, Martin Lemke, Jörn Schaffran, Lea Steder und Ronny Sternberger. Für jedes erdenkliche Problem, ob mechanischer Aufbau, Konstruktion, elektrische Verkabelung oder Programmierung der Steuerungselektronik fand sich eine Lösung.

Als Grundlage für meine Auswertungen dienten mehrere Zehntausend Bilder, die in der "Vor-OBACHT-Zeit" alle von Hand genommen wurden. Agnesa Guddat habe ich zu verdanken, dass ich nicht alle selber nehmen musste und meine Augen ein bisschen weniger quadratisch geworden sind.

Für Unterstützung bei Materialanalysen und die Möglichkeit Cavities für die Probenentnahme "zu zersägen" danke ich Waldemar und Xenia Singer sowie Alexey Ermakov.

Ich danke Jürgen Eschke, Birte van der Horst, Axel Matheisen, Marco Schalwat, Manuela Schmökel, Nicolai Steinhau-Kühl und allen anderen Beteiligten an Präparation und Kryogenik in Halle 3. Nur so konnte ich meine Analysen der inneren Oberfläche auch mit der "realen Welt" des Vertikaltests vergleichen.

Hans Weise hatte für mich immer eine offene Tür und ein offenes Ohr und stand mit Rat und Tat auch über den Rand von rein physikalischen Problemen hinaus zur Verfügung. Ein besonderer Dank gilt Lutz Lilje und Detlef Reschke. Beide haben mich an ihrem ungeheuren Erfahrungsschatz teilhaben lassen und in die Welt der supraleitenden Cavities eingeführt; gemeinsame Diskussionen waren immer wieder hilfreich und sie haben

frühe und späte Versionen meiner Arbeit korrigiert.

Über die letzten Jahre war DESY für mich aber nicht nur Arbeitsplatz, sondern auch ein Ort an dem ich sehr viele nette Menschen kennengelernt habe. Da es den Rahmen sprengen würde hier alle aufzuzählen, beschränke ich mich stellvertretend auf meine Bürokollegen Felix, Marc und Timon, mit denen ich außer fachlichen und weniger fachlichen Diskussionen auch genug angenehme Zeit bei den verschiedensten Aktivitäten ausserhalb des Büros verbracht habe.